Original paper

From magmatic arc to a post-accretionary setting: Late Palaeozoic granitoid plutons in the northwestern Trans-Altai Zone, Mongolia

Pavel HANŽL[1]*, Vojtěch JANOUŠEK[1], Kristýna HRDLIČKOVÁ[1], David BURIÁNEK[1], Ochir GEREL[2], Battushig ALTANBAATAR[3], John M. HORA[1], Petr ČOUPEK[1]

[1] Czech Geological Survey, Klárov 3, 118 21 Prague 1, Czech Republic; pavel.hanzl@geology.cz
[2] Geoscience Center, School of Geology and Mining Engineering, Mongolian University of Science and Technology, Ulaanbaatar 14191, Mongolia
[3] National Geological Survey of Mongolia, Ulaanbaatar 18072, Mongolia
*Corresponding author

The Trans-Altai Zone in the southern tract of the Central Asian Oceanic Belt is composed of Early Palaeozoic oceanic crust preserved in Ordovician to Devonian ophiolite fragments and Devonian–Carboniferous igneous arcs. The Edren and Baaran subzones at the NW tip of the Trans-Altai Zone were intruded by Late Palaeozoic plutons that have been examined by the combined geochronological and geochemical study.

Mississippian subduction-related plutons intruded Devonian and Carboniferous volcano-sedimentary sequences in two magmatic pulses. The older, Tournaisian plutons (dated at 352 ± 1 and 347 ± 4 Ma) occur in both subzones; the younger Visean/Serpukhovian ones (331 ± 1 Ma) are found only at the northern boundary of the Edren Subzone. All Mississippian rocks are high-K calc-alkaline and characterised by a strong enrichment of hydrous fluid mobile lithophile elements over conservative Nb, Ta and Ti relative to normal mid-ocean ridge basalts. Low $^{87}Sr/^{86}Sr_i$ ($\sim 0.7035–0.7038$) and highly positive ε_{Nd}^i values ($+6.6$ to $+5.2$) suggest a relatively juvenile parental magma source with a short mean crustal residence. This corresponds well with the age of scarce inherited zircons, none of which is older than 530 Ma.

The Early Permian post-tectonic plutons intruded the shallow crust of the Baaran Subzone (Devonian–Carboniferous flysch and Early Carboniferous volcanic arc). The prominent concentric body of the Aaj Bogd Pluton is composed of monzodiorites to monzogabbros (284 ± 1 and 294 ± 3 Ma) in its centre, surrounded by granite with syenite (282 ± 1 Ma) in the main mass of the pluton. Whole-rock Sr–Nd isotopic ratios match those of Carboniferous magmatic rocks, while trace-element patterns point to an intra-plate origin influenced by a fertile asthenospheric mantle component. On the other hand, the slightly older (290 ± 1 Ma) quartz syenites to alkali feldspar granites in the Baaran Subzone have spurious arc-like geochemistry inherited from their arc-related crustal source(s). Regional distribution of the numerous oval-shaped Early Permian alkaline post-orogenic plutons, some with A_2-type granite affinity, follows the major Permian strike-slip zones spanning from the Dulate Arc in the west to the Khan Bogd Pluton in the east. These late, transcurrent zones apparently played an important role in late-orogenic magma generation, ascent and emplacement.

1. Introduction

The Central Asian Orogenic Belt (CAOB; Mossakovsky et al. 1993), also known as Altaids (Suess 1901), rims the Siberian cratonic block from the Ural Mountains to the Pacific Ocean. It represents a huge Late Mesoproterozoic to Late Palaeozoic accretionary orogen (Şengör et al. 1993; Jahn 2004; Windley et al. 2007; Safonova et al. 2011). Palaeozoic accretionary continental growth was terminated by Late Carboniferous to Triassic collision (e.g., Xiao et al. 2009; Lehmann et al. 2010), culminating in the closure of the Mongol–Okhotsk Ocean at the end of the early/middle Jurassic (Zorin 1999) or even the latest Jurassic–earliest Cretaceous (Van der Voo et al. 2015).

The Mongolian tract of the CAOB (Fig. 1) began to develop in the Cambrian by thrusting the Neoproterozoic to Early Cambrian ophiolites over the Proterozoic basement – the Tuva-Mongolia, Zavkhan and Baidrag microcontinents (Lehmann et al. 2010; Jian et al. 2014; Buriánek et al. 2017; Khukhuudei et al. 2020). Thrusting was followed by intrusion of the 2000 km long Cambrian–Ordovician Ikh-Mongol Arc System into the Proterozoic basement and a stacked pile of ophiolites (Janoušek et al. 2018). Development of the southerly Chinese, Mongolian and Gobi Altai domains continued by successive accretion of Ordovician to Devonian volcano-sedimentary complexes (Badarch et al. 2002; Xiao et al. 2009; Jiang et al. 2017). Further to the south, Silurian to
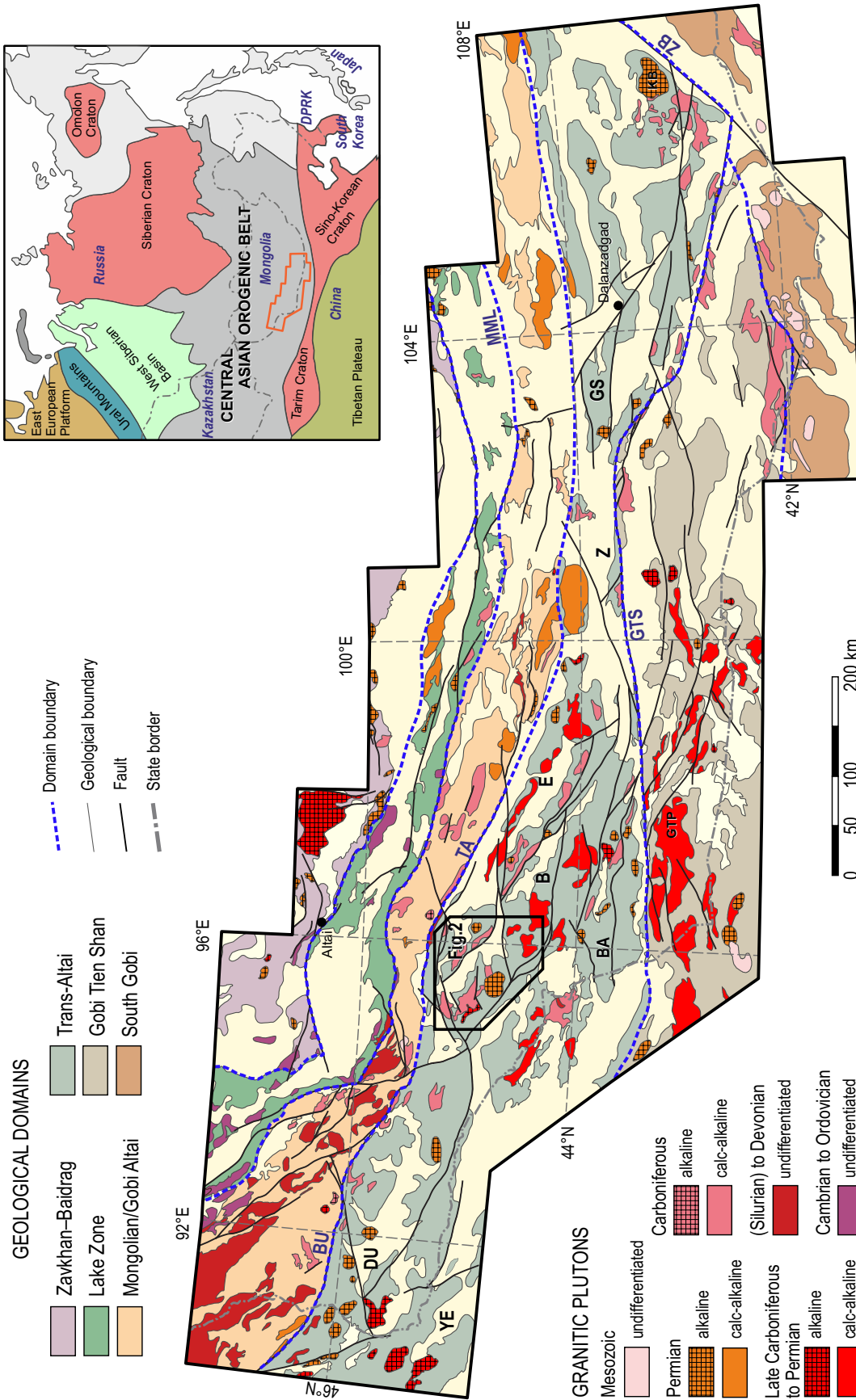
Fig. 1 Geological zonation of SW Mongolia with distribution of granitic plutons and position of studied area (modified from Badarch et al. 2002 and Guy et al. 2021). Inset: location of Mongolia in frame of the Central Asian Orogenic Belt. Master faults and major tectonic boundaries: MML – Main Mongolian Lineament, BU – Bulgan Fault, TA – Trans-Altai Fault Zone, GTS – Gobi Tien Shan Fault, ZB – Zuunbayan Fault. Subzones: DU – Dulate Arc, YE – Yemaquan Arc, E – Edren, B – Baaran, BA – Baytag, GS – Gurvansaikhan, Z – Zuulen. Plutons: GTP – Gobi Tien Shan, KB – Khan Bogd.

Early Carboniferous oceanic crust that is accompanied by arc-related Carboniferous (Nguyen et al. 2018) to alkaline Permian (Kozlovsky et al. 2007) magmatic rocks is known as the Trans-Altai Zone (Ruzhentsev and Pospelov 1992; Helo et al. 2006; Kröner et al. 2010).

All stages of the CAOB evolution were accompanied by massive production of geochemically mainly primitive plutonic rocks (Jahn et al. 2000). Numerous plutonic bodies of Cambrian to Permian (or even Triassic) age are arranged in distinct zones reflecting geotectonic settings variable in time and space (Cai et al. 2015; Wang et al. 2017 for review). Post-orogenic Carboniferous to Permian plutons also dominate the Trans-Altai Zone (Kozlovsky et al. 2005, 2012; Kozakov et al. 2007; Hanžl et al. 2008; Yang et al. 2022) and Eastern Junggar (e.g., Liu et al. 2013). Early Palaeozoic plutonic rocks in the Trans-Altai Zone are exposed only in the Zuulen (Zoolen) Terrane (Jian et al. 2014), representing the tectonic suture between the Baaran and Baytag subzones (Helo et al. 2006) and continuation of this zone to the Eastern Junggar (Zhang et al. 2017; Zhang et al. 2018b). However, Late Carboniferous to Permian post-tectonic granitic and, rarely, gabbroic massifs are widespread throughout all three zones, reflecting the evolution of the geodynamic regimes from late subduction to post-tectonic (Cai et al. 2015).

Late Palaeozoic calc-alkaline to alkaline and even peralkaline intrusive and extrusive igneous rocks in Mongolia and northern China evolved at the final stage of amalgamation in this part of the CAOB (Jahn 2004; Liu et al. 2013; Mao et al. 2014; Antipin et al. 2016; Zhou et al. 2021). The intra-plate magmatic activity at the margin of the Siberian Craton was related to Late Palaeozoic–Early Mesozoic Central Asian extension that was manifested in the formation of several rifts of different ages (e.g., Chen and Jahn 2004; Jahn 2004; Kovalenko and Chernov 2008; Buriánek et al. 2012, 2016; Yarmolyuk et al. 2013; Kozlovsky et al. 2015). In western Mongolia, this Asian rift system consists of five lineaments: Gobi Tien Shan, Main Mongolian, Gobi Altai, North Gobi, and North Mongolian–Trans-Baikalian, respectively (Yarmolyuk et al. 2014 for review). The Late Palaeozoic rifting propagated progressively from the continental margin toward the interior during the final stage of the Palaeo-Asian Ocean closure (e.g., Yarmolyuk et al. 2014; Liu et al. 2017). In the southern CAOB, the rifting was accompanied by common extension-related magmatism and intrusion of A-type granitic plutons; the latter have been interpreted as being associated with the Permian activity of the Tarim mantle plume (Zhang et al. 2010; Yarmolyuk et al. 2014).

There is a lack of isotopic data from Late Palaeozoic plutonic rocks in the Trans-Altai Gobi if compared with westerly Eastern Junggar, easterly Gurvansaikhan area

in the Middle Gobi, and the northerly Mongol and Gobi Altai zones. Therefore, this study focuses on the nature, likely source and emplacement conditions of the Carboniferous subduction-related and Early Permian post-tectonic plutons in the NW tip of the Trans-Altai Zone. Finally, we compare our data with other Late Palaeozoic granites in the adjacent parts of the CAOB, drawing some general conclusions regarding the genesis and geodynamic setting of post-tectonic granitoids.

2. Geological settings

2.1. General regional subdivision

Mongolia is traditionally subdivided into two geological super-units (Amantov et al. 1970; Marinov et al. 1973) separated by a system of Cenozoic faults known as the Main Mongolian Lineament (Fig. 1):

1) The northern super-unit includes Precambrian basement in Tuva-Mongolia, Zavkhan and Baidrag blocks, as well as Neoproterozoic to Lower Palaeozoic accretionary wedge and ophiolites of the Lake Zone;

2) The southern generally Palaeozoic super-unit was subdivided by Kröner et al. (2010) from north to south to (a) the Mongol Altai and Gobi Altai zones, (b) the Trans-Altai Zone, and (c) the Gobi Tien Shan Zone. The Mongol Altai and Gobi Altai zones consist of accreted Lower Palaeozoic back-arc/fore-arc basins, island arcs, granite–migmatite complexes and turbidite sequences (Burenjargal et al. 2014; Hanžl et al. 2017; Jiang et al. 2017; Lehmann et al. 2017; Buriánek et al. 2022). The Devonian–Carboniferous volcanic rocks and turbidites in the Trans-Altai Zone are imbricated with Early Palaeozoic ophiolites and oceanic sediments (Ruzhentsev and Pospelov 1992; Helo et al. 2006; Edel et al. 2018). The southernmost Gobi Tien Shan Zone, consisting of Silurian to Lower Carboniferous oceanic sediments and Carboniferous terrestrial volcanic rocks (Ruzhentsev 1985; Ruzhentsev and Pospelov 1992; Hanžl and Krejčí eds 2008), was intruded by numerous Late Carboniferous–Early Permian arc plutons (Hanžl et al. 2008; Yarmolyuk et al. 2008; Economos et al. 2012).

2.2. Geology of the Trans-Altai Zone

The Trans-Altai Zone (TAZ) in southern Mongolia is separated from the northerly Gobi Altai Zone by the system of Trans-Altai faults (also known as Bulgan Fault in the west – Cunningham 2005) and from the southerly Gobi Tien Shan Zone by the Cenozoic Gobi Tien Shan Fault. Laterally, the TAZ continues to Eastern Junggar towards the west and towards the easterly Zuunbayan

Fault in southern Mongolia, as shown by geophysical data (Guy et al. 2021). In SW Mongolia, the TAZ can be subdivided from north to south into the Edren, Baaran, Zoolen and Baytag subzones (Fig. 1) *sensu* Badarch et al. (2002).

The **Edren Subzone** forms the northern part of the Trans-Altai Zone separated from the Gobi Altai Zone by the system of E–W trending faults and could be correlated with the more easterly Gurvansaikhan Zone. The Edren Subzone comprises deformed Devonian sandstones and conglomerates with layers of siliceous shales, jasper and pillow lavas in the north. Slightly metamorphosed Devonian volcanic rocks (massive dacites–andesites, basaltic pillow lavas and agglomerates) containing limestone lenses with Early Devonian brachiopods (Šourek ed. 2003) dominate in the southern part of this unit. The basalts are characterised by an island-arc geochemical signature (Lamb and Badarch 2001). The overlying sequence of Middle to Upper Devonian flysch, associated with mafic to intermediate volcanic rocks, is probably rift-related (Ruzhentsev and Pospelov 1992; Lamb and Badarch 1997; Kröner et al. 2010; Lehmann et al. 2010; Rippington et al. 2013). The Devonian rocks are covered by products of acid–intermediate volcanism of the Early Carboniferous age (Filippova et al. 1990).

The Edren Subzone was intruded by Carboniferous and Permian gabbro, diorite, granodiorite and granite, rarely also monzonite plutons (Hanžl et al. 2008; Yarmolyuk et al. 2008; Hanžl et al. 2020).

The boundary of the **Baaran Subzone** with the Edren Subzone is masked by a narrow NW–SE trending trough filled by Mesozoic and Cenozoic sediments (Hanžl and Krejčí eds 2008; Hanžl et al. 2020); however, it is not manifested by any pronounced geophysical signal (Guy et al. 2015). Towards the WNW, this zone continues towards the Dulate Arc (Xiao et al. 2004) in NW China. Varicoloured hemipelagic sediments represent the Lower Devonian sequence of the Baaran Subzone with rare pillow lavas and limestone lenses. Younger, Upper Devonian to Mississippian turbidites are imbricated in the NE with shallow-sea to brackish water sediments and volcaniclastic rocks with limestones of Tournaisian age (Šourek et al. 2003). Mississippian andesite lavas and domes accompanied by rare rhyolites and basalts of volcanic-arc origin (Nguyen et al. 2018) are characteristic of this region. The Baaran Subzone was intruded by Late Carboniferous to Permian granitic and, rarely, gabbroic plutons (Hanžl et al. 2008; Yarmolyuk et al. 2008; Cai et al. 2014, 2015).

The narrow **Zuulen Subzone,** sandwiched between the Baaran and Baytag subzones, was defined as an accretionary prism (Badarch et al. 2002). Its structure is characterised by locally highly deformed rocks of ophiolite character that have undergone greenschist-facies metamorphism (Ruzhentsev and Mossakovsky 1995; Helo et al. 2006). The zone wedges out westward, where it is defined by a narrow anastomosing Trans-Altai Shear Zone (Hanžl et al. 2008; Guy et al. 2015). The southern branch of the Zoolen Subzone can be correlated with the Armantai ophiolitic belt in the Eastern Junggar (Xiao et al. 2009; Song et al. 2019), while its northern branch corresponds to the Irtysh (Erqis) Zone separating the Chinese Altai from the Eastern Junggar in NW China (Xiao et al. 2004; Long et al. 2012). Oceanic sediments with jasper layers contain radiolaria and sponges that were determined to be Late Silurian–Early Devonian in age (Zonenshain et al. 1975; Ruzhentsev et al. 1985; Lamb and Badarch 2001). Helo et al. (2006) reported U–Pb SHRIMP zircon ages of 421 ± 3 and 417 ± 2 Ma for volcanic rocks from the eastern part of this unit. The rocks show a calc-alkaline affinity and primitive Nd isotopic ratios corresponding to a juvenile intra-oceanic arc setting.

The **Baytag Subzone** forms the southernmost part of the Trans-Altai Zone along the boundary with the South Gobi Zone. It extends westwards into the Yemaquan Arc of the Eastern Junggar (Zhang et al. 2007; Song et al. 2019). The boundary between the Baaran and Baytag subzones is clear in the SE, where it is accentuated by serpentinite-bearing tectonic slices of the Zuulen Subzone. However, its continuation to the NW is not apparent and probably follows one of the WNW–ESE mylonitic zones. The Baytag Subzone consists of Devonian deep-water sediments with cherts, pillow lavas and rare carbonates. Folded Upper Devonian to Lower Carboniferous siliciclastic flysch sediments with pronounced cleavage are exposed in tectonic slices inside the unit (Hanžl and Krejčí eds 2008). The whole subzone is covered by Carboniferous intermediate to acid continental volcanic rocks interpreted as a product of subduction-related magmatism (Nguyen et al. 2018). Late Carboniferous to Permian post-tectonic gabbro and granite stocks with alkaline affinity dominate this unit. Some older deformed granitoids with primitive arc chemistry were also described close to the boundary between Baytag and Baaran subzones (Hanžl et al. 2008). Early Devonian tonalites and porphyries were reported from the Eastern Junggar south of the Aaj Bogd Range, close to the Mongolian border (Zhang et al. 2018b and references therein).

3. Methodology

Plutonic bodies and their host rocks of the northern tip of the Trans-Altai Zone W and NW of Eej Khayrkhan Mountain were sampled in the Gobi Altai province's southern part for petrography, whole-rock geochemistry and U–Pb zircon dating (Fig. 2, Tab. 1).
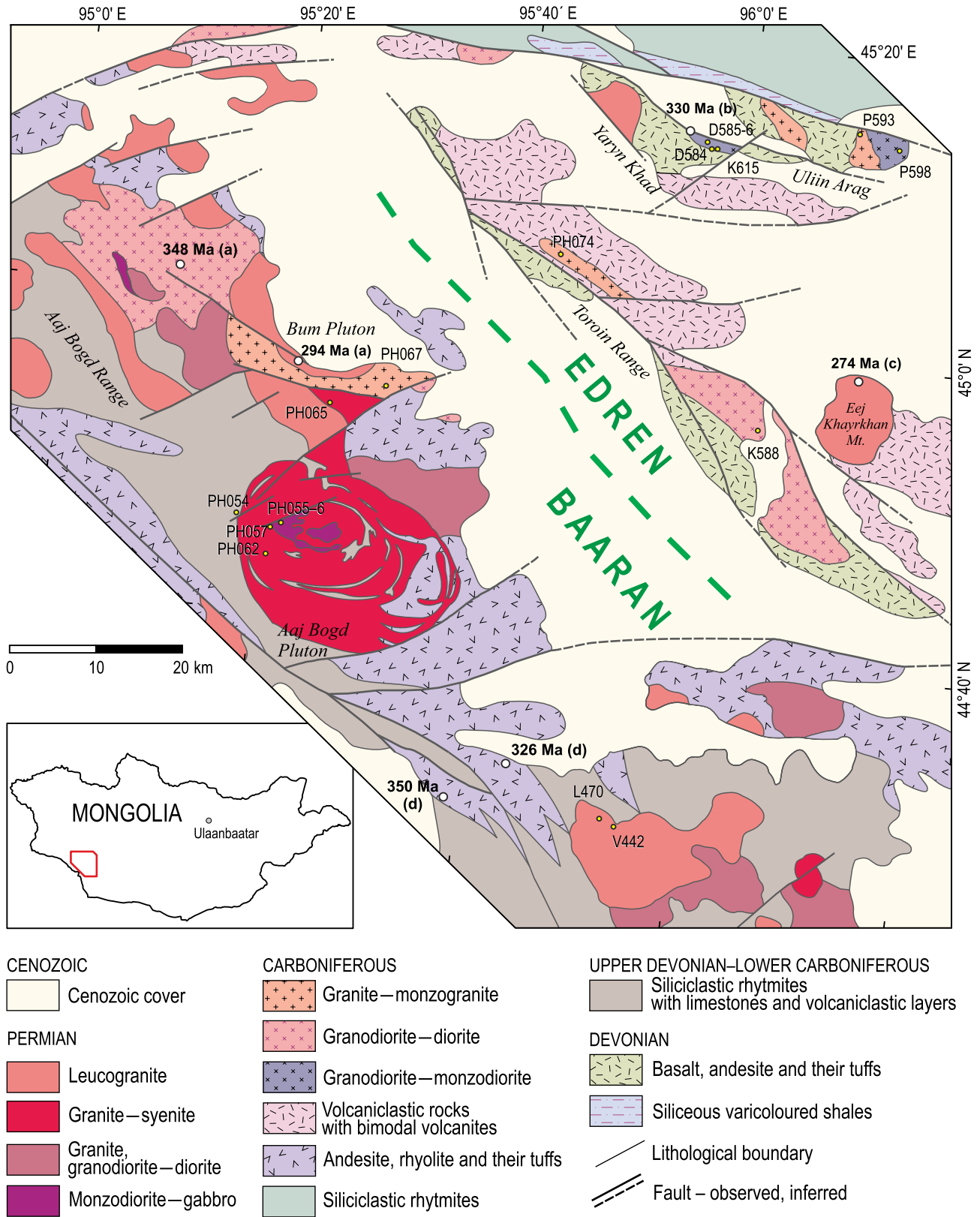
Fig. 2 Geological map of Aaj Bogd area with locations of studied samples and published radiometric ages (modified from Nguyen et al. 2018 and Hanžl et al. 2020). (a) – Yarmolyuk et al. (2008), (b) – Izokh et al. (2011), (c) – Kozakov et al. (2007), (d) – Nguyen et al. (2018).

Tab. 1 General description of studied samples from the NW Trans-Altai Zone

Sample	X	Y	Rock	Unit	Description	Minerals	Age (Ma)	Datasets[†]
D585A	95.92973	45.21921	Quartz monzodiorite	Edren Subzone; Yaryn Khad (C)	Fine-grained MME in granodiorite	Pl, Amp, Bt, Qz, Mag, Ttn, Aln, Ap, Zrn	–	WR, Pet, Sr–Nd
D585B	95.92973	45.21921	Granodiorite	Edren Subzone; Yaryn Khad (C)	Medium-grained, common MME	Pl, Kfs, Qz, Bt	–	WR
D586	95.91850	45.22677	Quartz diorite	Edren Subzone; Yaryn Khad (C)	Coarse-grained, fresh rock	Pl, Kfs, Amp, Bt, Cpx, Opx, Mag, Ilm, Ap	–	WR, Pet, Sr–Nd
K615	95.93736	45.21693	Granodiorite	Edren Subzone; Yaryn Khad (C)	Coarse-grained with mingling textures, in endocontact with volcanic wall-rocks	Pl, Kfs, Qz, Pl	330.2 ± 0.7	D
P593	96.16675	45.24408	Granite	Edren Subzone; Uulin Arag (C)	Coarse-grained, porphyritic	Kf, Qz, Pl, Bt	–	WR, Sr–Nd
P598	96.22591	45.24059	Quartz monzodiorite	Edren Subzone; Uulin Arag (C)	Coarse-grained, altered	Pl, Amp, Bt, Kfs, Mag, Ttn, Ap, Zrn (Ep, Chl)	–	WR, Pet
PH074	95.73705	45.07639	Granite	Edren Subzone; Toroin Range (C)	Porphyritic, medium-grained	Kfs, Pl, Bt, Ms, Qz	345.5 ± 4.0	WR, Pet, Sr–Nd, D
K588A	96.06358	44.92202	Granite	Edren Subzone; Toroin Range (C)	Medium-grained, xenoliths of fine-grained volcanic rocks	Kfs, Pl, Qz, ±Bt	–	WR, Nd
PH054	95.30127	44.76849	Hornfels	Baaran Subzone; Aaj Bogd host rocks	Medium-grained rock in endocontact of pluton	Qz, Kfs, Ms, Bt, Pl, Grt, Sill, Crd, Ap, Zrn	–	Pet
PH055	95.35103	44.76813	Quartz monzodiorite	Baaran Subzone; Aaj Bogd (P)	Medium-grained enclaves in granite, mingling textures	Pl, Amp, Bt, Mag, Ilm, Ap, Zrn	286.3 ± 1.2	WR, Pet, D
PH056A	95.34716	44.76662	Monzogabbro	Baaran Subzone; Aaj Bogd (P)	Medium-grained, lens in serpentinitized rock	Pl, Amp, Cpx, Opx, Mag, Ilm, Ap	284.5 ± 0.6	WR, Pet, Sr–Nd, D
PH056B	95.34777	44.76762	Monzogabbro	Baaran Subzone; Aaj Bogd (P)	Coarse-grained, lens in serpentinitized rock	Pl, Cpx, Opx, Ol, Amp, Mag, Ilm, Ap	–	Pet
PH057	95.34534	44.76638	Granite	Baaran Subzone; Aaj Bogd (P)	Porphyritic, medium-grained	Kfs, Pl, Qz, Bt, Ap, Mnz, Zrn	–	WR, Pet
PH062	95.34205	44.73245	Syenite	Baaran Subzone; Aaj Bogd (P)	Coarse-grained, perthitic, rare metagreywacke xenoliths	Kfs, Pl, Bt, Amp, Mag, Ilm, Ap, Zrn	281.2 ± 0.9	WR, Pet, Sr–Nd, D
PH065	95.39847	44.89315	Quartz syenite	Baaran Subzone; Aaj Bogd Satellite (P)	Red, coarse-grained, porphyritic with small gneiss xenoliths	Kfs, Qz, Bt, Pl	289.1 ± 0.9	WR, D
PH067	95.48968	44.92369	Monzogranite	Baaran Subzone; Bum (C)	Porphyritic, coarse-grained, MME, Fsp megacrysts	Pl, Kfs, Qz, Bt, Amp, Mag, Ilm, Ap, Zrn	350.1 ± 1.1	WR, Pet, Sr–Nd, D
L470	95.87827	44.49365	Alkali-Fsp granite	Baaran Subzone; Aaj Bogd Satellite (P)	Medium grained	Kfs, Pl, Qz, ±Bt, Ep	–	WR
V442	95.90881	44.48517	Alkali-Fsp granite	Baaran Subzone; Aaj Bogd Satellite (P)	Pink to red, medium-grained with granophyric textures	Kfs, Qz, Pl, Bt	–	WR

† Pet – petrological data, WR – whole-rock chemical analyses, Sr–Nd – strontium and neodymium isotopic data, D – LA-ICP-MS U–Pb zircon dating

3.1. Electron-microprobe and P–T–X conditions

Electron-microprobe analyses of minerals (Electronic Supplementary Material, ESM 1) were carried out using a Cameca SX-100 electron microprobe at the Joint Laboratory of the Masaryk University and the Czech Geological Survey in Brno. The minerals were measured under the following conditions: accelerating voltage 15 kV, beam current 10 nA and beam diameter 3–8 μm. Natural minerals and stable synthetic compounds were used as standards. Peak-counting times were 10 and 20 s for major elements and 30 and 40 s for minor to trace elements. Raw intensities were processed by X–φ matrix correction (Merlet 1994). Mineral abbreviations are after Whitney and Evans (2010). The following standards were used (K_α X-ray lines): augite (Si, Mg), orthoclase (K), jadeite (Na), chromite (Cr), almandine (Al), andradite (Fe, Ca), rhodonite (Mn), TiO_2 (Ti).

The electron-microprobe analyses of amphiboles were recalculated to atoms per formula unit (*apfu*) according to Hawthorne et al. (2012). Pyroxene analyses were recalculated based on 6 oxygen atoms (and Fe^{3+} estimated following Droop 1987), micas based on 22 anions and olivine on 4 oxygen atoms. X_{Fe} for biotite was computed as $Fe_{tot}/(Mg + Fe_{tot})$.

Amphibole compositions were used to estimate P–T–X conditions of emplacement. Thermobarometric formulations of Ridolfi et al. (2010) were used because they can be applied to hybrid and re-homogenized magmas (e.g., Ridolfi et al. 2010; Laeger et al. 2013). The accuracy of the obtained P–T conditions was tested by the edenite–richterite (model B) thermometer (Holland and Blundy 1994).

3.2. Laser-ablation ICP-MS U–Pb dating of zircon

Zircons were separated using conventional techniques (crushing, grinding, sieving, Wilfley gravity separation table, magnetic and heavy-liquid separation) at the Central Geological Laboratory in Ulaanbaatar. Subsequently, individual zircons were hand-picked from the zircon concentrate using a petrographic microscope, embedded in epoxy resin and polished. Their internal structure and zoning were imaged using cathodoluminescence (CL) on a scanning electron microscope (SEM) in laboratories of the Czech Geological Survey in Prague-Barrandov (CGS).

Zircons were dated by the U–Pb method using an Analyte Excite 193 nm excimer laser-ablation system (LA, Photon Machines) equipped with a two-volume HelEx ablation cell in tandem with an Agilent 7900x ICP-MS housed at the CGS. The ablation took place in a He at-

mosphere ($0.8 \, l \cdot min^{-1}$), the laser frequency was 5 Hz, the laser fluence $7.59 \, J \cdot cm^{-2}$ and the beam diameter 25 μm. Each measurement consisted of 20 s integration of the entrainment background signal and another 40 s integration of the sample ablation signal for masses 202, 204, 206, 207, 208, 232 and 238 using an SEM detector with one point per mass peak and mass integration times 10, 10, 15, 30, 20, 10 and 15 ms (total cycle time 0.134 s). To monitor the stability of the instrument and ensure the reliability of the measured results, international zircon standards (91500 as the primary reference material and Plešovice and GJ-1 as the secondary reference materials) were measured after every twenty sample points. Instrumental drift throughout the measurement was monitored by repeated analyses of the reference zircon 91500 (Wiedenbeck et al. 1995). Data processing was performed using Iolite software as described in Paton et al. (2011), including background correction, followed by laser-induced elemental fractionation (LIEF) correction based on comparison with the behavior of the reference zircon 91500 (1065 Ma – Wiedenbeck et al. 1995) whose concordant age of 1063 ± 6 Ma obtained in the course of the current study matched the reference value well. During this study, reference samples of Plešovice zircon (337 Ma – Sláma et al. 2008) and GJ-1 (609 Ma – Jackson et al. 2004) were periodically analyzed, giving concordant ages of 338 ± 3 and 608 ± 5 Ma (2σ). The data obtained (ESM 2) were statistically adjusted, and error correction was performed by propagating the relative error on the primary reference material (ESM 3), according to Horstwood et al. (2016). The propagated uncertainties were used to plot the mean and concordia ages using the IsoplotR software (Vermeesch 2018). The weighted mean and Tera-Wasserburg plots are presented for individual samples. No common Pb correction was employed.

3.3. Whole-rock geochemistry

Major and trace elements in fresh whole-rock samples (3–4 kg) were determined in the AcmeLabs Vancouver (now Bureau Veritas Minerals) by ICP-OES/MS. The dissolution of the samples was by $LiBO_2/Li_2B_4O_7$ fusion in order to determine precisely also rare earth and refractory elements stored in refractory accessory phases. Detection limits were 0.01% and better for major elements, 2 ppm and better for trace elements used for our geochemical interpretation and 0.05 ppm and better for REE.

Data management, recalculation, plotting and statistical evaluation of the whole-rock geochemical and isotopic data were facilitated by *GCDkit* (Janoušek et al. 2006). In this work, the mg number (mg#) is defined as $100 \times MgO/(FeO_t + MgO)$ [mol. %] and the A/CNK index, uncorrected for apatite (Shand 1943) as $Al_2O_3/(CaO + Na_2O + K_2O)$ [mol. %]. For a description

of chondrite-normalized REE patterns serves the Eu/Eu* ratio, reflecting the magnitude of the Eu anomaly ($Eu/Eu* = Eu_N / \sqrt{Sm_N Gd_N}$), where N refers to concentrations normalized to chondritic abundances (Boynton 1984).

3.4. Radiogenic isotopes

Strontium and neodymium isotopic analyses were done by thermal ionization mass spectrometry (TIMS) using the Thermo-Fisher Triton Plus instrument at the CGS. Before analysis, powdered samples were dissolved and dried in several steps and separated via column chromatography. Samples were (1) dissolved in 3.5 ml 29M Romil HF + 1.5 ml concentrated doubly-distilled HNO_3, followed by drying down, (2) dissolved and dried down three times in 1 ml concentrated doubly-distilled HNO_3, and (3) dissolved in 4 ml doubly-distilled 6M HCl, from which aliquots corresponding to 200 ng of Nd were further processed for column chromatography. Strontium and REE were isolated from the bulk dissolved matrix using SR and TRU-spec resins manufactured by Eichrom (Pin et al. 1994). Neodymium was further separated from the REE fraction using LN resin (Pin and Zalduegui 1997), following the techniques described in Míková and Denková (2007).

Strontium was loaded onto Ta single filaments and TIMS analyses were done in static mode, with simultaneous collection of ^{84}Sr, ^{85}Rb, ^{86}Sr, ^{87}Sr, and ^{88}Sr, at typical ion beam intensities of 6–12 V on ^{88}Sr for 150 ratios, each with 8 s integration time. Neodymium was loaded onto Re filaments and analyzed in double filament configuration, static mode, with simultaneous collection of ^{143}Nd, ^{144}Nd, ^{145}Nd, ^{146}Nd, ^{147}Sm, and ^{150}Nd, at typical ion beam intensities of 2–4 V on ^{144}Nd, for 120 ratios, each with 4 s integration time. Isotopic ratios were corrected for gain, baseline, isobaric interferences, and instrumental mass fractionation, assuming $^{146}Nd/^{144}Nd$ = 0.7219 (Wasserburg et al. 1981), and $^{86}Sr/^{88}Sr = 0.1194$ (Steiger and Jäger 1977). External reproducibility is estimated from repeated analyses over a 3-year period of the JNdi-1 standard (Tanaka et al. 2000) [$^{143}Nd/^{144}Nd$ = 0.512099 ±8 (2σ, n = 42)] and NBS-987 standard [$^{87}Sr/^{86}Sr = 0.710267 ± 22$ (2σ, n = 87)]. Decay constants applied to age-correct isotopic ratios are from Steiger and Jäger (1977) for Sr and Lugmair and Marti (1978) for Nd. The ε_{Nd} values were obtained using the Bulk Earth parameters of Jacobsen and Wasserburg (1980). In order to account for the more complex evolution of Nd isotopes in crustal melts and/or to compensate for the effects of crystal accumulation upon the $^{147}Sm/^{144}Nd$ ratios, we calculated not only single-stage but also two-stage Depleted Mantle Nd model ages ($T_{Nd.2stg}^{DM}$), using the parameters and the approach of Liew and Hofmann (1988).

4. Results

4.1. Field relationships, petrography and mineral chemistry

Plutonic rocks in the Edren and Baaran subzones were studied at the northwestern tip of the Trans-Altai Zone (Fig. 1).

4.1.1. Edren Subzone

Lower Devonian rocks of the NW tip of the Edren Zone are represented by chloritized and epidotized crystal tuffs of andesite composition, basaltic agglomerates and pillow lavas. Rare greenschist-facies foliation is steep and NW–SE striking. Devonian rocks and the Lower Carboniferous bimodal volcanic and volcaniclastic sequence are folded together by NW–SE trending upright folds. Two plutons were sampled south of the boundary with the Gobi Altai Zone in the Yaryn Khad and Uliin Arag mountain ranges and one in the southerly Toroin Range west of Eej Khayrkhan Mountain (Fig. 2).

In the NW, the **Yaryn Khad Pluton** (samples K615, D585, and D586) is a small oval body intruded into Devonian pillow lavas and is overlain from the north by Cenozoic sediments. Steep foliation bearing dip-slip lineation is locally developed along the exocontact of the pluton. The pluton dominantly consists of biotite granodiorite to orthopyroxene–amphibole monzodiorite, with bodies of olivine gabbro, gabbronorite, and lherzolite in the western part (Izokh et al. 2011). The felsic rocks (granite to granodiorite) show evidence of mingling with mafic magmas (Fig. 3a). Numerous aplitic and basaltic dykes crosscut the lithologically heterogeneous pluton.

Medium-grained granodiorite/quartz diorite to syenite/monzodiorite samples consist of plagioclase (63–54 vol. %), quartz (25–18 vol. %), K-feldspar (11–10 vol. %), amphibole (9–4 vol. %), biotite (1–4 vol. %) and orthopyroxene (0–1 vol. %). Subhedral to euhedral plagioclase (An_{26-66} Or_{0-3}) grains are oscillatory zoned and locally show effects of sericitization and kaolinization. Some grains contain needle-shaped apatite inclusions.

$\Rightarrow$

Fig. 3 Field photographs of representative rock types from the studied area of the Trans-Altai Zone. **a** – Magma mingling textures between granite and monzodiorite; Yaryn Khad Pluton (K615). **b** – Metamorphosed pillow lavas with skarns among pillows; endocontact of the Yaryn Khad Pluton (D584). **c** – Weathered quartz monzodiorite from the Uliin Arag Pluton (P598). **d** – Monogenic enclave swarm in granite of the Toroin Range (K588). **e** – Garnet-rich layer in hornfelsed tuffitic sandstone; exocontact of the Aaj Bogd Pluton (PH064). **f** – Mingling zone between monzodiorite and granite cut by aplite dykes; central part of the Aaj Bogd Pluton (PH056). **g** – Syenite with metagreywacke xenoliths (PH062). **h** – Carboniferous Bum monzogranite with rapakivi megacrysts (PH067).

Euhedral K-feldspars (Or_{80-95} Ab_{5-20}) are usually fresh. Subhedral to anhedral magnesio-ferri-hornblende to magnesio-hastingsite [^{C}(Al+Fe+2Ti) = 0.55–1.03 *apfu*, ^{A}(Na+K+2Ca) = 0.23–0.51 *apfu*; ESM 1] crystals are light-brown to dark-green. Orthopyroxene (enstatite, Si = 1.95–1.98, Al = 0.02–0.04 *apfu*, X_{Mg} = 0.56–0.63, ESM 1) is occasionally overgrown by amphibole or biotite. Biotite flakes (^{IV}Al = 2.33–2.41 *apfu*, X_{Mg} = 0.55–0.58) are rarely altered to chlorite.

Devonian pillow lavas with tuffs and carbonates in interstitial spaces among pillows (Fig. 3b) were metamorphosed to amphibolite (Amp+Cal+Pl±Kfs±Ep± Qz) and skarn, respectively, in the thermal aureole of the pluton. The contact skarn (D584) consists of the Ep+Qz +Cal+Grt+Cpx mineral assemblage.

In the east, **Uliin Arag Pluton** intruded the slightly deformed and altered basalts with rare rhyolite layers. Basaltic dykes are common throughout the pluton. Porphyritic biotite granite (P593) prevails in the western part of the pluton, while hornblende–biotite granodiorite to quartz monzodiorite with mafic microgranular enclaves dominates in the eastern part. Equigranular, medium-grained, slightly altered quartz monzodiorite (P598, Fig. 3c) consists of subhedral to euhedral plagioclase (51 vol. %; An_{24-28} Or_{0-2}), biotite altered to chlorite (25 vol. %), magnesio-ferri-hornblende [22 vol. %; ^{C}(Al+Fe +2Ti) = 0.54–0.69 *apfu*, ^{A}(Na+K+2Ca) = 0.27–0.38 *apfu*], and quartz (3 vol. %).

The biotite granite (K588, PH074) in the **Toroin Range** is an elongated body with rare microdiorite enclaves. It intruded the Carboniferous volcanic and volcaniclastic bimodal sequence in the north and the altered Devonian volcanoclastic rocks of andesite composition in the south. Slightly altered rocks are characterised by poikilitic K-feldspar enclosing euhedral zoned plagioclase and biotite leaves. Rare muscovite was found only in sample PH074. The pluton is crosscut by many subvolcanic dykes and contains numerous, partly dissolved xenoliths of the country-rock Carboniferous basalts (Fig. 3d) with steep NW–SE striking preferred orientation.

4.1.2. Baaran Subzone

Many plutonic bodies of variable shape and size are well exposed in the Aaj Bogd mountain range N of Altai village close to the Chinese border. The most conspicuous and varied body, the **Aaj Bogd Pluton**, is located in the central plateau of the range. Permian granites and Carboniferous granodiorites and mozogranites rimming the NE slopes of the range form the composite **Bum Pluton** originally described as Permian (Yarmolyuk et al. 2008). Plutonic rocks intruded the Devonian–Carboniferous siliciclastic rhythmites of turbidite origin and Mississippian

volcanic sequence of dominantly andesite composition (Nguyen et al. 2018).

4.1.3. Aaj Bogd Pluton

The Aaj Bogd Pluton has a characteristic circular shape with a diameter of *c.* 25 km and is zoned with small bodies of monzogabbros to quartz monzodiorites in the center and syenite–granite forming the bulk of the pluton. This 'onion skin' structure of the Aaj Bogd Pluton is accentuated by thin circularly-aligned septa of wall rocks, whose primary NE–SW trending bedding was reoriented parallel with the outline of the body. Foliation developed in the exocontact also respects the round shape of the pluton.

In a narrow zone in the roof of the intrusion, greywackes, siltstones and volcaniclastic rocks were thermally metamorphosed to massive hornfels (Fig. 3e) composed of quartz, K-feldspar, plagioclase, locally also decomposed cordierite, biotite and, exceptionally, garnet and sillimanite.

Quartz monzodiorites to monzogabbros in the center of the Aaj Bogd Pluton (PH055, PH056A, B) are medium- to coarse-grained with ophitic texture. Grain size decreases slightly towards contact with the surrounding granites, where mingling textures document coeval intrusion of both end members (Fig. 3f). The mafic rocks are formed by olivine, two pyroxenes, plagioclase, amphibole and biotite. Magnetite, ilmenite, long-prismatic apatite, pyrite, pyrrhotine and pentlandite are common accessory phases. Olivine is subhedral, relatively fresh forsterite (Fo_{69-70} Fa_{30} Tep_1). The prevalent orthopyroxene is enstatite (En_{74-75} Fs_{25-26}). Some of these orthopyroxene crystals are surrounded by diopside rims (Di_{80} Hd_{20}). Ti-rich magnetite commonly forms inclusions in orthopyroxene, in which slightly elevated Cr contents can be observed. Ferroactinolite and Ti-rich phlogopite are products of orthopyroxene decomposition. Plagioclase is subhedral to euhedral, optically unzoned, sometimes showing diffuse chemical zoning with a decrease of the An component from labradorite–bytownite cores (An_{75-69}) to andesine rims (An_{49-41}). Ilmenite with titanomagnetite lamellae is a common accessory mineral. Pyrrhotite, commonly with pentlandite inclusions in grain cores, and pyrite are abundant, as is acicular apatite.

Coarse-grained syenite (PH062) encloses rare angular country-rock xenoliths (Fig. 3g) and is composed mainly of feldspars (K-feldspar slightly predominates over plagioclase), amphibole and biotite. Apatite, titanite, ilmenite with titanomagnetite exsolutions and zircon are common accessories. K-feldspar (Or_{96-97} Ab_{3-4}) grains are subhedral to anhedral with common perthite. Subhedral to anhedral plagioclase shows continuous normal magmatic zoning ($An_{21-23} \rightarrow An_{4-11}$). Euhedral grains of amphibole

[magnesio-ferri-hornblende to actinolite; ^{C}(Al+Fe+2Ti) = 0.44–0.61 *apfu*, ^{A}(Na+K+2Ca) = 0.29–0.43 *apfu*] are nearly completely decomposed to a mixture of titanite, magnetite, zircon, chlorite and K-feldspar. Rare biotite (X_{Fe} = 0.44) is also partly chloritized.

Porphyritic leucogranite (PH057) is a medium-grained rock composed of quartz, feldspars (K-feldspar and plagioclase in equal proportions) and biotite. K-feldspar (Or$_{95–98}$ Ab$_{2–5}$) is subhedral and distinctively perthitic, with newly formed albite grains along cleavage planes. Euhedral plagioclase shows a continuous normal magmatic zoning with andesine cores (An$_{30–40}$) and oligoclase rims (An$_{26–28}$). Albitic rims at contact with K-feldspar and myrmekites are common. Biotite (X_{Fe} = 0.44–0.50), if present, is mostly chloritized. Accessory minerals are represented by apatite, ilmenite, magnetite and zircon.

4.1.4. Bum Pluton and minor bodies in the Aaj Bogd Range

Coarse-grained porphyritic amphibole–biotite monzogranite (PH067) was sampled from the E–W elongated body (Bum Pluton) cut by common trachytic and basaltic dykes on the northern slopes of the Aaj Bogd Ridge. This rock is composed of plagioclase, K-feldspar, amphibole, biotite and rare quartz and is porphyritic with white plagioclase and pink rapakivi-like K-feldspar megacrysts up to 5 cm across (Fig. 3h). Euhedral oligoclase–andesine grains are oscillatory zoned, whereby the An content decreases rimwards (An$_{40}$ → An$_{29–35}$). Andesine cores are altered to albite, sericite and clinozoisite; oligoclase rims are albitized. K-feldspars are usually perthitised (up to Ab$_3$) and with albite rim. Columnar amphibole is magnesio-ferri-hornblende to magnesio-hornblende [^{C}(Al+Fe+2Ti) = 0.59–0.65 apfu, ^{A}(Na+K+2Ca) = 0.28–0.37 *apfu*] and encloses titanite and apatite grains locally. Biotite, if preserved, is anhedral with X_{Fe} = 0.45–0.49 and is commonly altered to chlorite and small grains of secondary apatite. Accessory minerals are zircon, magnetite, (leucoxenised) ilmenite and titanite.

Two samples of alkali-feldspar granite to quartz syenite were obtained SE of Aaj Bogd Range (L470, V442), and one N of the Aaj Bogd Pluton (PH065). These rocks of simple modal composition (Kfs+Pl+Qtz±Bt) are reddish grey, medium-grained, slightly porphyritic and rarely contain small, nearly assimilated country-rock xenoliths.

4.2. U–Pb zircon dating

4.2.1. Edren Subzone

Two samples from Edren Subzone were taken for zircon dating: K615 from Yaryn Khad Pluton and PH074 from the Toroin Range. The best-developed zircon grains in equigranular biotite granodiorite **K615** from **Yaryn Khad Pluton** are euhedral, bipyramidal, *c.* 120–150 µm long if they are long-prismatic (aspect ratio 1 : 3) or *c.* 100 µm long if stubby (1 : 2) (Fig. 4a). Most common are originally subhedral fragments bearing a wide range of diverse textural and structural features reflecting the local magma dynamics in the pluton. These include entirely igneous oscillatory zoning, sector zoning, complex discontinuous zoning recording stages of growth/corrosion and convolute zoning. The zircon grains also commonly contain unzoned inherited cores. Their uranium content ranges between 79–1380 ppm; Th/U ratios are 0.26–0.79. A concordia age obtained from 56 spots is 331±1 Ma with MSWD = 1.3 (Fig. 5a, ESM 2).

Only 18 zircon grains were separated from the porphyritic biotite granite (**PH074)** of **Toroin Range**, 26 spots were analyzed in total, only 7 of which were useable for further processing. The subhedral grains 1 and 6 are apparently the oldest. Grain 1 is *c.* 160 µm long with 1 : 3 elongation; grain 6 is *c.* 110 µm long with an indeterminable ratio (fragment?). Both grains show irregular sector zoning (Fig. 4b) distinct from the others in the CL image. The U contents are 77 and 1846 ppm, and Th/U ratios are 0.31 and 0.69 in grain 1, while U = 179 ppm and Th/U = 0.74 in grain 6. Early Cambrian ages are mutually consistent in both spots on grain 1 (Fig. 4b: individual ages of 528±16 and 532±12 Ma, giving mean of *c.* 534 Ma). A significantly younger Early Ordovician age of *c.* 484 Ma was obtained from grain 6 (Fig. 5b, ESM 2).

The dipyramidal crystals 11, 17, and 19 are euhedral to subhedral and long prismatic (1 : 3 to 1 : 4). Grains 17 and 19 have oscillatory zoning and CL-bright cores that darken rimwards. Grain 11 contains a conspicuous core overgrown by two external zones, *c.* 10 µm thick (Fig. 4b). U contents are 189–513 ppm, Th/U ratios 0.52–0.79 (except grain 11 with Th/U = 1.03). The calculated concordia age corresponds to 347±4 Ma with MSWD = 1.5, but the limited reliability of the age calculated from only four spots should be taken into account (Fig. 5b, ESM 2).

The other grains, many being fragments, vary widely in size (50–300 µm). Some of them are characterised by oscillatory zoning with relatively thick zones (*c.* 10–20 µm), the others have only uniform, conspicuously dark luminescence. This widely variable zircon set yielded a highly heterogeneous range of geologically inconsistent ages from Early Triassic to Early Jurassic suggesting late-stage processes accompanied by alteration and lead loss.

4.2.2. Baaran Subzone

Aaj Bogd. Quartz monzodiorite to monzogabbro samples PH055 and PH056A represent the central mafic part and the syenite (PH062) the main body of the Aaj Bogd Pluton.
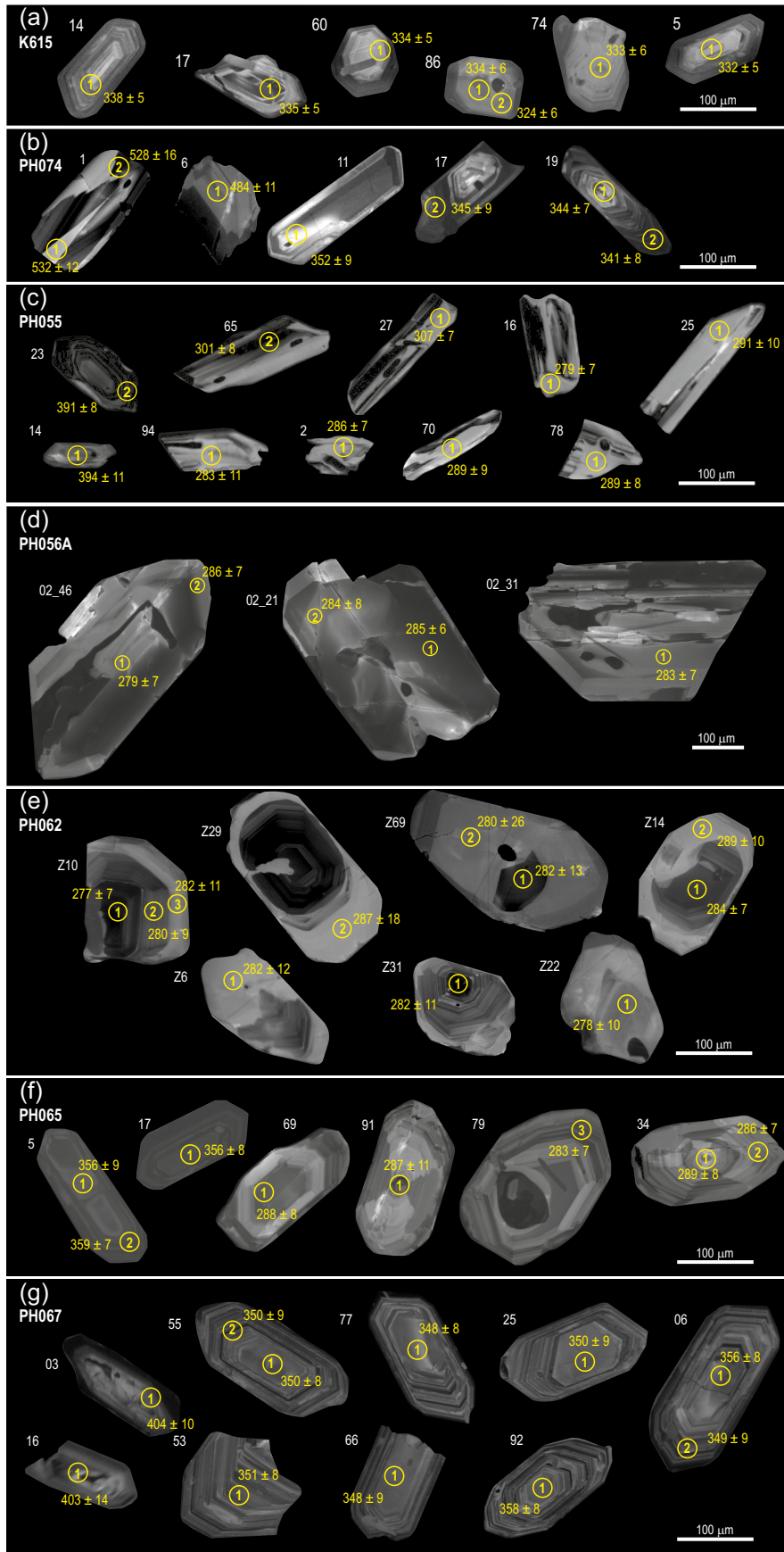
Zircon grains from the quartz monzodiorite **PH055** are mostly long-prismatic (1 : 4 to 1 : 5), euhedral to subhedral with a length exceeding 200 µm but subhedral to anhedral grains with an average size of 80–130 µm and elongation ratio 2 : 1 are also present. Uranium concentrations vary between 39 and 708 ppm; Th/U ratios are 0.39–1.69. Despite such a wide range in Th/U values, no significant differences in internal zircon zoning or ages were observed between the grains. The CL images feature irregular lamellae, in some cases with signs of resorption (Fig. 4c). The 35 processed zircon measurements yielded an Early Permian age of 294 ± 3 Ma with MSWD = 1.2 (Fig. 6a, ESM 2). Two euhedral, shortly prismatic (1 : 2.5), *c.* 100 µm long grains (23 and 14) have bipyramidal shape and blurred original oscillatory zoning with relatively dark luminescence. The U concentrations are 324 and 206 ppm, respectively; Th/U ratios are 0.66 and 0.54. These two xenocrysts gave the oldest ages of *c.* 394 Ma (Fig. 6a, ESM 2).

Zircon grains in the monzogabbro **PH056A** are euhedral to subhedral, stubby (1 : 2 to 1 : 2.5), of average length of *c.* 300 µm. They usually show cores of indistinctive lamellar zoning, in some cases mantled by thin oscillatory-zoned rims, whereas most of the grains have relatively thick (*c.* 20 mm) bright luminescent external zone. In CL images they

Fig. 4 Cathodoluminescence images of representative zircon grains from the studied samples along with individual [206]Pb/[238]U ages for the indicated spots. Edren Subzone: **a** – biotite granodiorite, Yaryn Khad Pluton (K615); **b** – biotite granite, Toroin Range Pluton (PH074). Baaran Subzone – Aaj Bogd Pluton: **c** – monzodiorite (PH055); **d** – monzogabbro (PH056A); **e** – syenite (PH062). Other bodies of the Baaran Subzone: **f** – syenite (PH065); **g** – monzogranite, Bum Pluton (PH067).
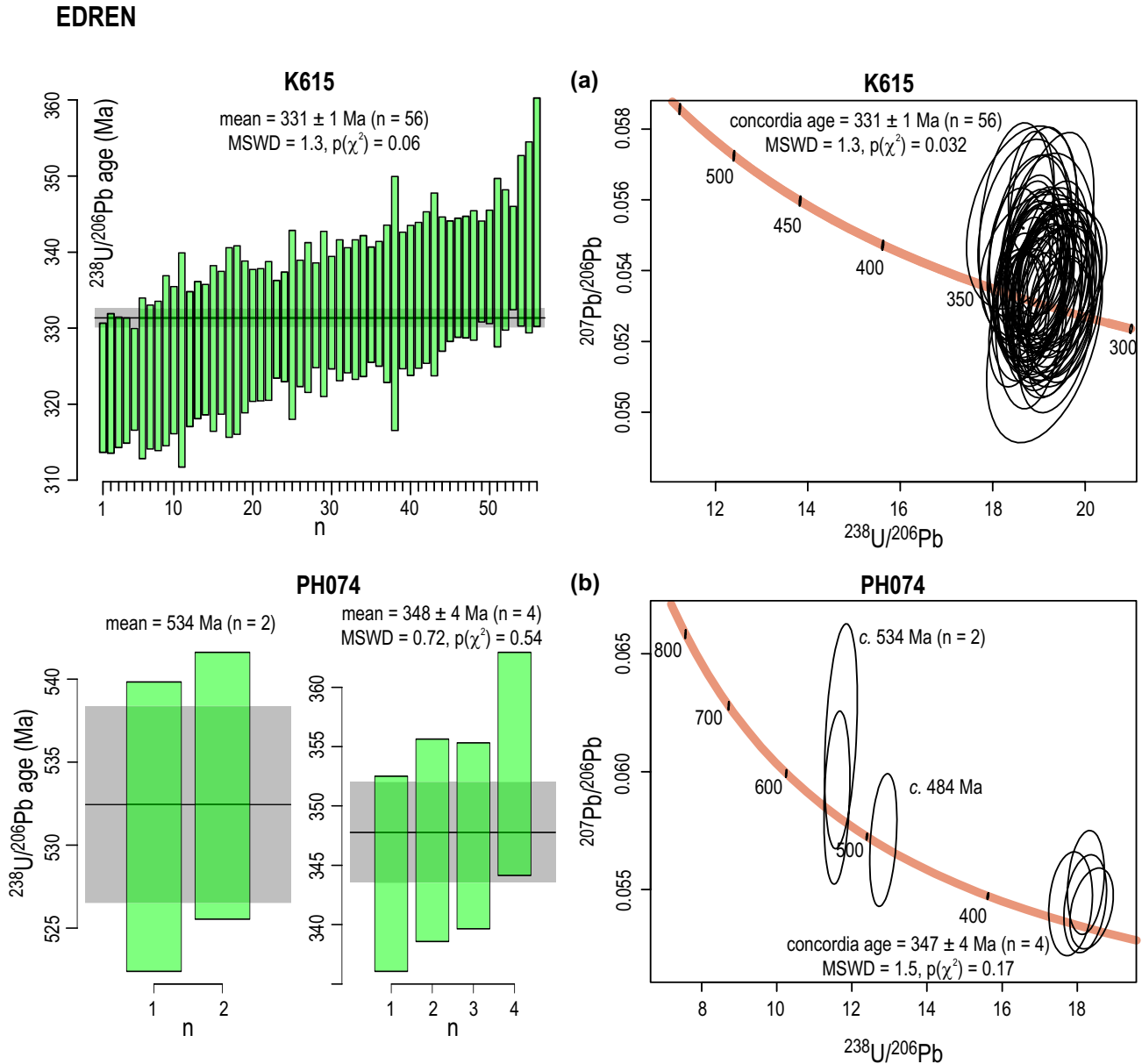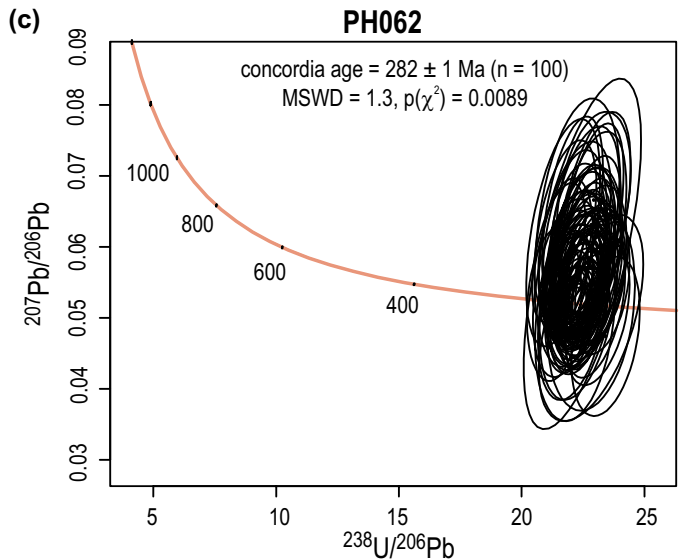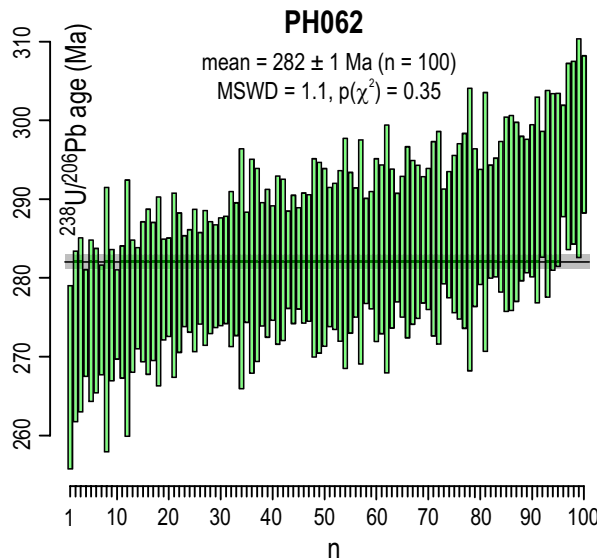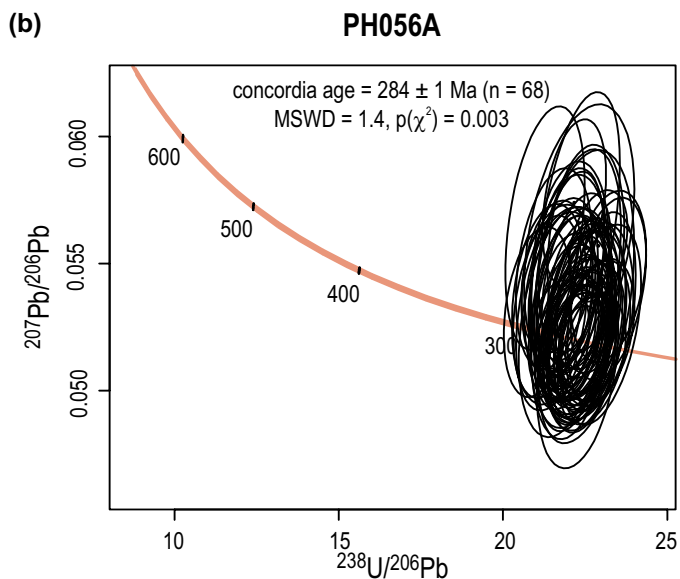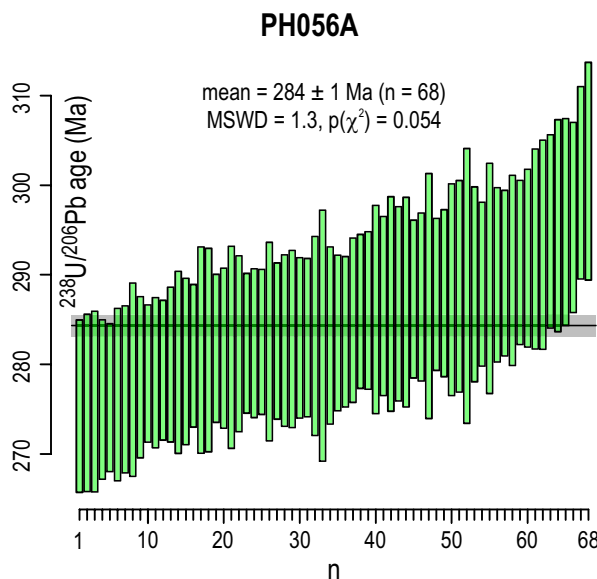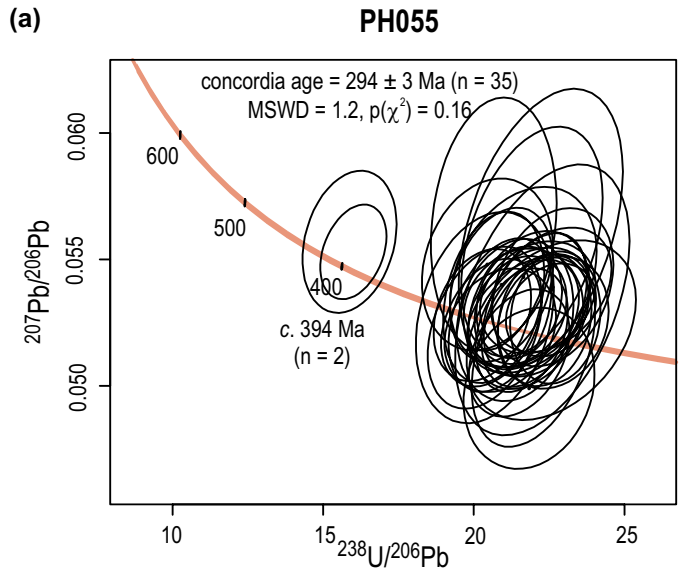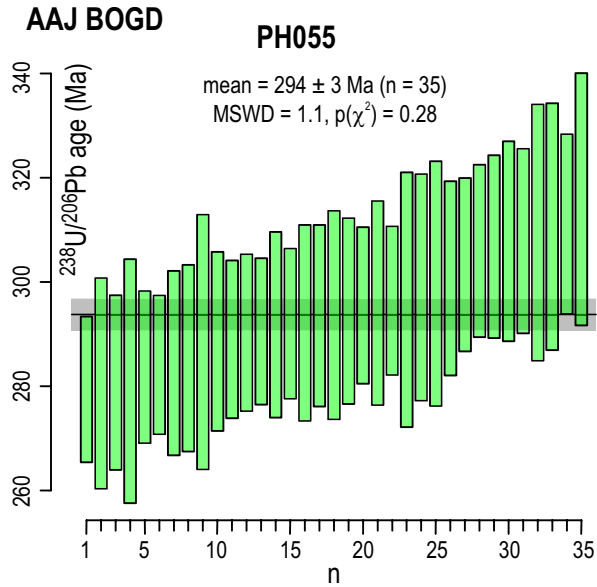
EDREN

Fig. 5 U–Pb weighted mean and Tera-Wasserburg concordia plots with calculated ages for magmatic zircons from plutons in the Edren Subzone: **a** – biotite granodiorite, Yaryn Khad Pluton (K615); **b** – biotite granite, Toroin Range Pluton (PH074). Weighted mean ages were calculated as concordia ages from $^{207}Pb/^{206}Pb$ to $^{238}U/^{206}Pb$ following Galbraith (2005). Concordia ages in Terra-Wasserburg plots were obtained using the three--dimensional maximum likelihood algorithm (Ludwig and Titterington 1994) modified by Ludwig (1998) to fit total U–Pb isochrons. The curves in Tera-Wasserburg plots are calculated using λ errors.

have ghost-like (to undulatory-like) appearance. Some parts of the grains, preferentially along cracks, are partially recrystallised (Fig. 4d). The U contents range 55–720 ppm and Th/U ratios are 0.35–1.27. Ages are independent of zircon appearance and composition, being *c.* 294–273 Ma. The 68 spots from the sample PH056A gave the Early Permian concordia age of 284 ± 1 Ma (MSWD = 1.4), which likely dates the intrusion (Fig. 6b, ESM 2).

Zircon grains in syenite **PH062** are euhedral to subhedral, stubby (1 : 2 to 1 : 2.5), mostly 150–300 μm long. Common dull unzoned xenocrystic cores with oscillatory

zoned rims are often overgrown by a thick CL-bright external zone. The effects of dissolution and ensuing new crystallization are seen in some grains (e.g., Z29; Fig. 4e). The U concentrations are 11–510 ppm, and Th/U ratios 0.45–1.86. The Early Permian concordia age of 282 ± 1 Ma (MSWD = 1.3) calculated from measurement on 100 spots reflects a magmatic event (Fig. 6c, ESM 2).

Other bodies of the Aaj Bogd Range. Porphyritic quartz syenite (**PH065**) comes from the northerly adjacent granitic body to the Aaj Bogd Pluton. Zircon forms euhedral to subhedral, short-prismatic (1 : 3) bipyramidal
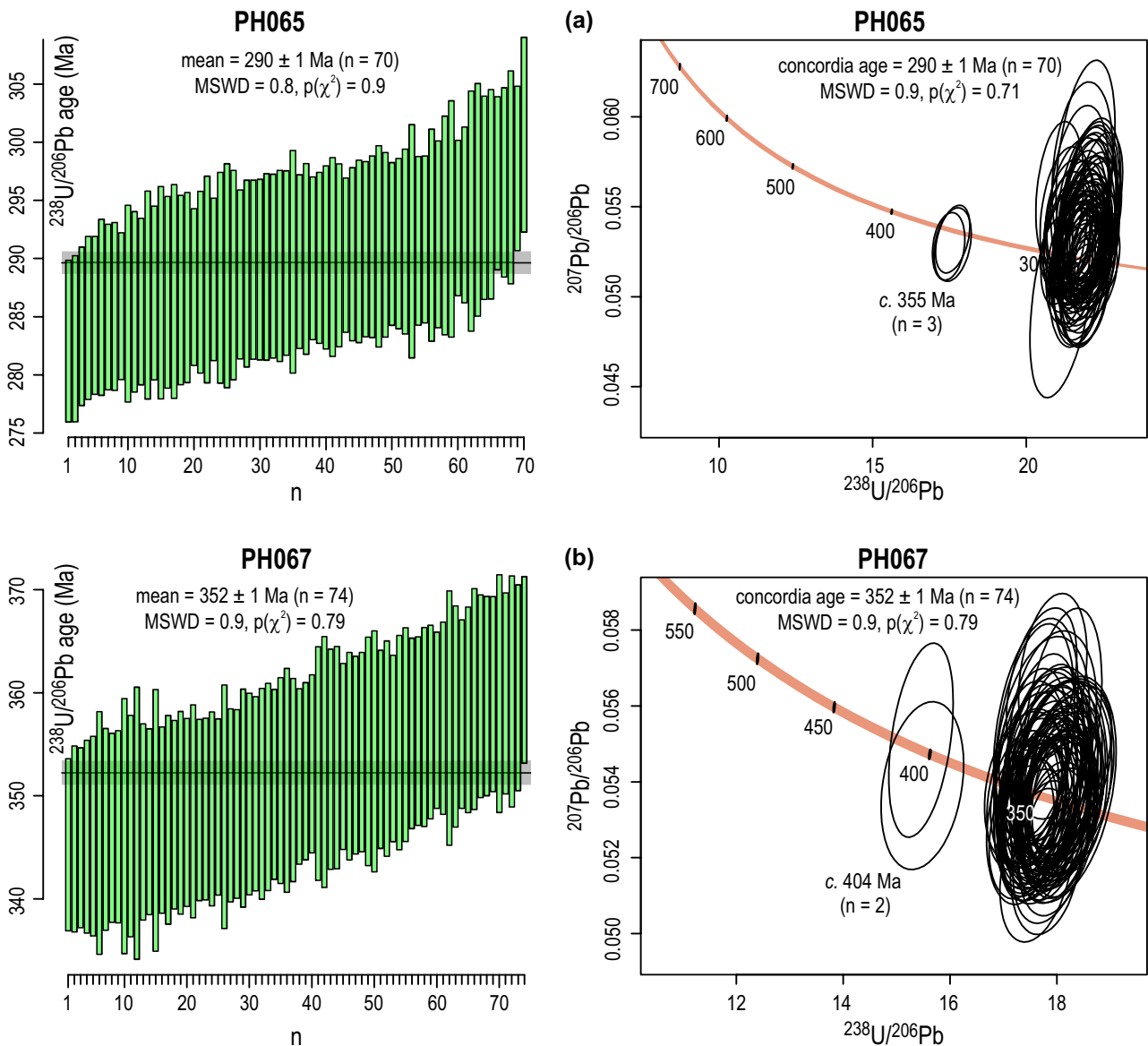
BAARAN

Fig. 7 U–Pb weighted mean and Tera-Wasserburg concordia plots with calculated ages for magmatic zircons from minor plutonic bodies of the Baaran Subzone: **a** – quartz syenite (PH065); **b** – monzogranite, Bum Pluton (PH067). For further details, see caption to Fig 5.
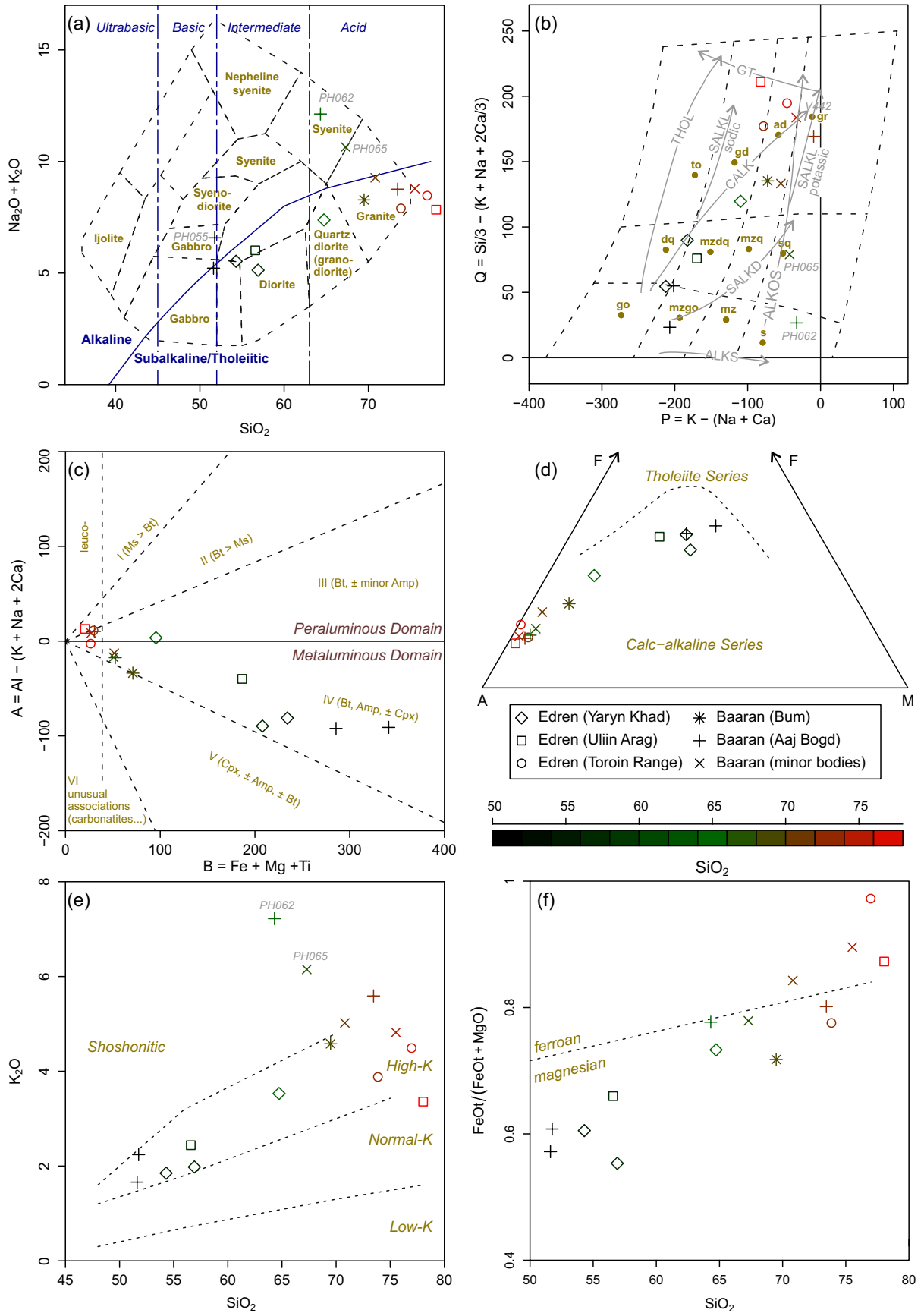
crystals, 120–160 μm long. The relatively large cores are overgrown by rims with fine oscillatory zoning; in cases, a *c.* 15 μm thick CL-bright zone emphasizes the interface between the core and the oscillatory-zoned rim. The hourglass-like sector zoning is apparent in some grains (Fig. 4f). U contents range from 25 to 768 ppm; Th/U ratios are 0.06–1.13. Early Permian magmatic age of 290 ± 1 Ma (MSWD = 0.9) was obtained from 70 spots

(Fig. 7a, ESM 2). In contrast, two grains (5 and 17) reveal significantly older (Early Carboniferous) ages. These grains are euhedral, bipyramidal, with large cores and limited number (*c.* five) of relatively massive external zones. They are of darker luminescence and better crystallised compared to other zircon grains in the sample (Fig. 4f). Uranium contents are 295–455 ppm and Th/U ratios range 0.46–0.49. Three spots in these two xenocrystic grains yielded ages of *c.* 355 Ma (Fig. 7a, ESM 2).

Porphyritic monzogranite (**PH067** from the Bum Pluton) contains numerous euhedral, stubby (1 : 2) bipyramidal zircon crystals, 150–250 μm long. They feature relatively large unzoned cores overgrown by oscillatory-

⇦

Fig 6 U–Pb weighted mean and Tera-Wasserburg concordia plots with calculated ages for magmatic zircons from Aaj Bogd Pluton in the Baaran Subzone: **a** – quartz monzodiorite (PH055); **b** – monzogabbro (PH056A); **c** – syenite (PH062). For further details, see caption to Fig 5.

zoned mantles (Fig. 4g). Uranium contents of 201–1573 ppm and Th/U ratios of 0.36–0.99 were measured. The 74 spot analyses gave consistent Early Carboniferous age of 352 ± 1 Ma, MSWD = 0.9 (Fig. 7b, ESM 2). Grains 3 (U = 503 ppm, Th/U = 0.44) and 16 (U = 349 ppm, Th/U = 0.75) are *c.* 120 μm long with 1:3 aspect ratio, and seem partly rounded with blurred original oscillatory zoning (Fig. 4g). These significantly older grains give ages of *c.* 404 Ma most likely corresponding to Early Devonian inheritance (Fig. 7b, ESM 2).

4.3. Whole-rock geochemistry

The dataset consists of 15 newly obtained whole-rock geochemical analyses of plutonic rocks (see ESM 4 for major- and trace-element data). It has been split into five groups: Edren Subzone (Yaryn Khad: n = 3, Uliin Arag: n = 2, Toroin Range: n = 2), Baaran Subzone (Aaj Bogd Pluton: n = 4, other bodies in the Aaj Bogd Range: n = 4). The samples were fresh and relatively large, in order to account for the coarse-grained or even porphyritic texture. Moreover, the whole dataset (perfectly fresh or not so) behaves coherently in all classification diagrams. Therefore, we assume that LILE (including alkalis) mobility was likely negligible, and that using the complete set of major- and trace elements is justifiable.

⇦

Fig. 8a Total alkali–silica (TAS) diagram after Cox et al. (1979) with the alkaline/subalkaline boundary of Irvine and Baragar (1971). **b** – Multicationic P–Q ('nomenclature') diagram of Debon and Le Fort (1983, 1988), where *P* represents the proportion of K-feldspar to plagioclase and *Q* the quartz content. The reference compositions of the twelve petrographic types are also shown as follows: to – tonalite, trondhjemite; gd – granodiorite; ad – adamellite (= monzogranite); gr – granite (= syenogranite); dq – quartz diorite, quartz gabbro, quartz anorthosite; mzdq – quartz monzodiorite, quartz monzogabbro; mzq – quartz monzonite; sq – quartz syenite; go – gabbro, diorite, anorthosite; mzgo – monzogabbro, monzodiorite; mz – monzonite; s – syenite. The marked trends refer to common subtypes of cafemic and alumino–cafemic associations: THOL, tholeiitic; CALK, calc-alkaline; SALKD, SALKL, dark- and light-coloured subalkaline (i.e., monzonitic); ALKS, dark-coloured alkaline saturated; ALKOS, light-coloured alkaline oversaturated; GT, granitic–trondhjemitic. **c** – Multicationic B–A ('characteristic minerals') plot of the same authors; *B* represents the content of mafic minerals and *A* is the balance of aluminium vs. calcium and alkalis (aluminosity). Typical of each of the sectors is a characteristic mineral assemblage; the I, II and III fields are for decreasingly peraluminous rocks [I – muscovite > biotite, II – biotite > muscovite, III – biotite (± minor amphibole)], the IV, V and VI fields for increasingly Al-deficient (metaluminous) rocks (IV – biotite, amphibole, ± clinopyroxene, V – clinopyroxene ± amphibole ± biotite, VI – unusual mineral associations, such as carbonatites]. **d** – Ternary AFM (A = Na$_2$O + K$_2$O, F = FeOt, M = MgO in wt. %) plot after Irvine and Baragar (1971) to distinguish between tholeiitic and calc-alkaline series. **e** – SiO$_2$ vs. K$_2$O diagram (wt. %) (Peccerillo and Taylor 1976) discriminating between the low-K, normal-K, high-K calc-alkaline and shoshonitic series. **f** – SiO$_2$ vs. FeOt/(FeOt + MgO) (wt. %) classification diagram of Frost et al. (2001). Note that the plotting colours in all panels reflect silica contents in each of the samples.

4.3.1. Major- and minor-element compositions

The dataset is compositionally rather heterogeneous, spanning from basic to acid (SiO$_2$ = 51.6–78.0 wt. %). This is shown, for instance, by the total alkali–silica (TAS) classification diagram of Cox et al. (1979) (Fig. 8a), where the samples range from gabbro to syenite or granite. Most classify as subalkaline, apart from alkaline samples PH055, PH062 and PH065.

Classification systems based on millications are considered superior to other schemes in that they reflect the stoichiometry of the main rock forming minerals (Bonin et al. 2020). The heterogeneity of the dataset is well illustrated by the multicationic P–Q diagram of Debon and Le Fort (1983, 1988) (Fig. 8b). In this 'nomenclature' diagram, the analyses from the Edren Subzone evolve from the quadruple point gabbro/quartz diorite/monzogabbro/quartz monzodiorite, through granodiorite to 'adamellite' (= monzogranite) fields, thus following a trend resembling a calc-alkaline subtype of the cafemic association (CALK) *sensu* Debon and Le Fort (1988). In the Baaran Subzone, the data points for the Aaj Bogd Pluton and other bodies in the Baaran Subzone define mainly a trend from syenite, through quartz syenite to 'adamellite' or 'granite' (= syenogranite). The two most mafic samples (PH055 and PH056A) correspond to monzogabbros – in the latter case transitional to a quartz monzodiorite. Together, the evolution can be described as dark- followed by light-coloured subalkaline (i.e., monzonitic; SALKD and SALKL) differentiation series of Debon and Le Fort (1988) (Fig. 8b).

The B–A multicationic diagram of Debon and Le Fort (1983, 1988) portrays the evolution of the aluminosity as a function of decreasing maficity and, consequently, the characteristic mineral assemblage (Fig. 8c). The studied rocks are mostly metaluminous (A/CNK down to 0.77; ESM 4), falling into sector IV of the diagram, with the characteristic mineral assemblage of Bt + Amp ± Cpx. Only the most felsic (leucogranitic) samples become subaluminous (A/CNK up to 1.05; i.e. *A* multicationic values turn slightly positive).

In the AFM diagram of Irvine and Baragar (1971) (Fig. 8d), all the analyses form a more or less continuous, relatively shallow (calc-alkaline) trend. The SiO$_2$ vs. K$_2$O diagram (Peccerillo and Taylor 1976) further classifies the Edren samples, together with the two most mafic (monzonitic) rocks of the Aaj Bogd Pluton, as high-K calc-alkaline (K$_2$O/Na$_2$O = 0.50–1.13 and 0.47–0.52 by weight). Most of the analyses from Aaj Bogd Pluton and smaller bodies in the Baaran Subzone define a negative trend from highly potassic ('shoshonitic') to high-K calc-alkaline (Fig. 8e), whereby potassium dominates over sodium (K$_2$O/Na$_2$O = 1.18–1.76 by weight).
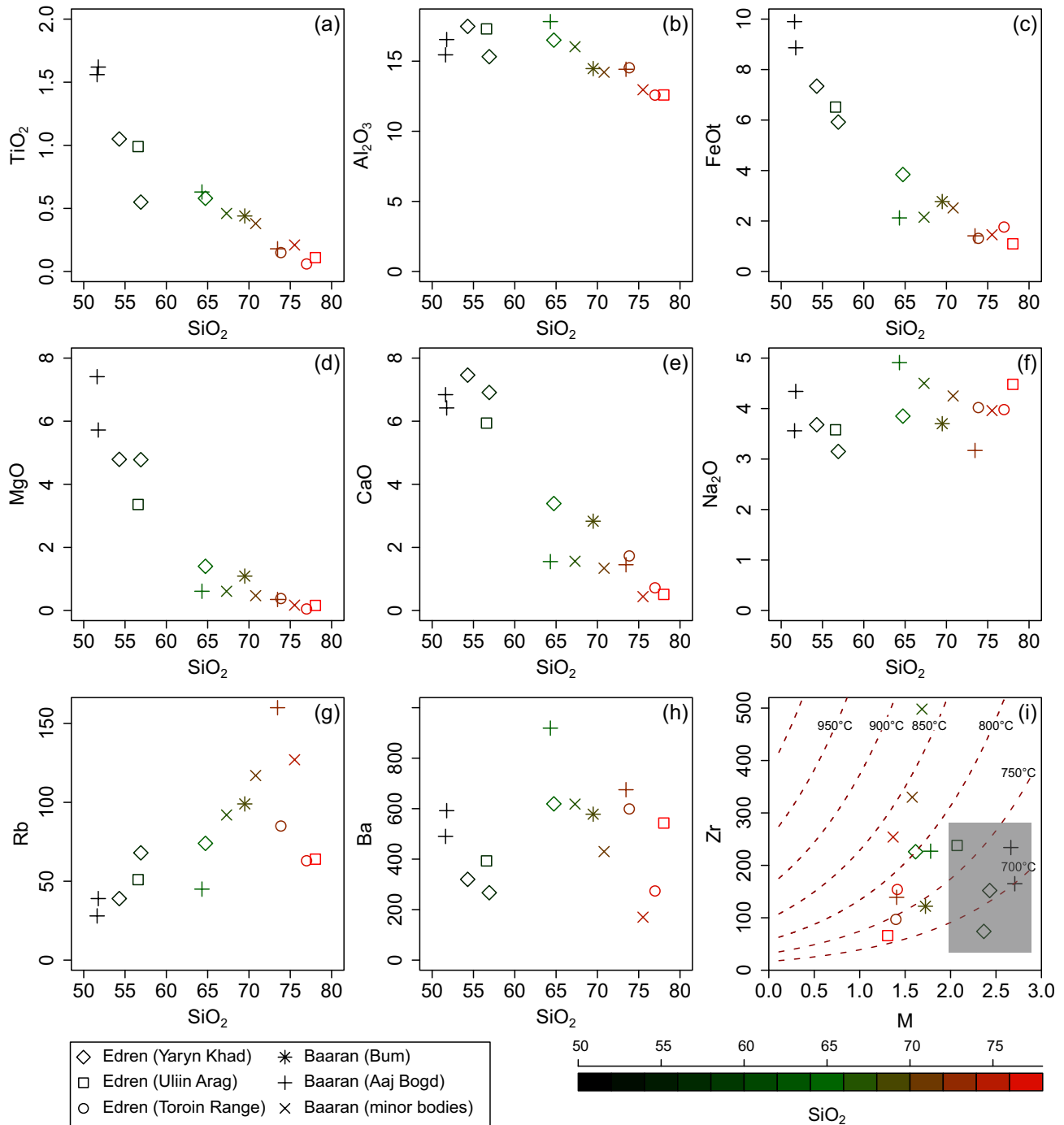
Fig. 9a–h Binary plots of SiO$_2$ vs. selected major-element oxides (wt. %) and trace elements (ppm). **i** – Binary plot of M [cationic ratio (Na+K+2Ca)/(Al×Si)] vs. Zr (ppm). The isotherms of Zr saturation levels were calculated using the model of Watson and Harrison (1983); only samples with M<2 were assumed to be saturated in zircon, and hence giving reasonable saturation temperatures that can be used to approximate the liquidus temperatures. While most of the samples were saturated at *c.* 700–800 °C, the minor bodies in the Baaran Subzone show highly heterogeneous, and generally high, zircon saturation temperatures.

In contrast to Debon and Le Fort's scheme based on millications, the SiO$_2$ vs. FeOt/(FeOt+MgO) diagram of Frost et al. (2001) employs weight percentages (Fig. 8f). In this projection, all samples seem to follow the same evolution, whereby the basic–intermediate types are

magnesian and the acid ones straddle the boundary of the ferroan domain. Accordingly, the mg# decrease with rising silica monotonously from 59 to a mere 4.8 (ESM 4).

Harker plots (Fig. 9a–f) for most of the dataset are characterised by more or less monotonous negative cor-

relations of TiO_2, FeOt and CaO with silica. Some trends, especially those for Al_2O_3 and MgO, have an inflection point at $SiO_2 \sim 65$ wt. %, being convex upward and downward, respectively (Fig. 9b, d).

4.3.2. Trace elements

Binary diagrams of SiO_2 vs. Rb and Ba (Fig. 9g–h) illustrate the incompatible character of Rb, and initially incompatible behaviour of Ba with an inflection point at $SiO_2 \sim 65$ wt. %, most likely connected to K-feldspar saturation.

Normal Mid-Ocean Ridge Basalt (NMORB) normalised (Sun and McDonough 1989) spider plots are shown separately for each of the five groups (Fig. 10a–e). All patterns display some common features; in particular, characteristic strong enrichments in Large Ion Lithophile Elements (LILE) (Cs, Rb, Ba and K) and Pb. All samples, apart from three of Aaj Bogd Pluton, additionally have high Th and U contents. Characteristic of all samples are negative anomalies in Nb and Ta, and for acid rocks also variable depletion in P and Ti. In some samples, notably those from the Yaryn Khad Pluton and small bodies of the Baaran Subzone, positive Zr–Hf anomalies can be observed.

Chondrite-normalized (Boynton 1984) HREE contents of the studied granitoids never drop below unity. Still, they exhibit a great deal of variation, both among, and within, individual groups (Fig. 11).

All analyses of the **Yaryn Khad Pluton** are characterised by moderate total REE contents (62.5–107.1 ppm) with a relatively low degree of LREE/HREE fractionation ($La_N/Yb_N = 2.7$–4.8) and either no or moderately negative Eu anomalies (Eu/Eu* = 0.99–0.61, Fig. 11a).

The **Uliin Arag** quartz diorite P598 and granodiorite P593 have contrasting chondrite-normalised REE patterns (Fig. 11b). The former sample is REE-rich (ΣREE = 113.6 ppm), and its pattern is basically straight, gently inclined ($La_N/Yb_N = 4.9$) with a negative Eu anomaly (Eu/Eu* = 0.66). The latter is rather REE-poor (ΣREE = 70.9 ppm), exhibiting a sea-gull shaped pattern strongly depleted in MREE, including Eu (Eu/Eu* = 0.66).

Two granitic samples from the **Toroin Range** display similar fractionated trends (ΣREE = 89.2 and 111.0 ppm, $La_N/Yb_N = 7.6$ and 16.5) but with contrasting magnitudes of negative Eu anomalies (Eu/Eu* = 0.81 and 0.24, Fig. 11c).

The two monzonitic samples from the **Aaj Bogd Pluton** (PH055, PH056A; Fig. 11d) have high total REE contents (~163 ppm) and moderately fractionated patterns (La_N/Yb_N of 7.0 and 8.4, respectively) with small, if any, negative Eu anomaly (Eu/Eu* = 0.84 and 0.97). Aaj Bogd syenite PH062 on the other hand yields a convex down, Eu-enriched (Eu/Eu* = 1.97) pattern with moder-

ate total REE content (120 ppm). Granite PH057 is poor in all REE (ΣREE = 87.1 ppm), especially the MREE and HREE ($Yb_N = 4.8$), with no Eu anomaly.

The **Baaran** quartz syenite PH065 (Fig. 11e) is relatively rich in all REE (ΣREE = 250 ppm), and has a strongly curved, convex down pattern ($La_N/Yb_N = 11.2$) with high HREE contents ($Yb_N = 15.2$) and a sizeable negative Eu anomaly (Eu/Eu* = 0.55). The samples L470 and V442 probably represent parts of a single differentiation sequence, with LREE more depleted than the syenite PH065, and Eu anomaly getting progressively deeper (Eu/Eu* = 0.54 and 0.20, respectively). The Bum monzogranite PH067 in contrast displays a rather steep, gently curved (convex downward), HREE-depleted pattern ($La_N/Yb_N = 8.8$, $Yb_N = 6.2$) lacking any Eu anomaly.

Minimal constraints on liquidus temperatures of the magmas parental to the non-cumulate granitoids can be obtained using zircon saturation thermometry (Janoušek 2006). The formulation of Watson and Harrison (1983) was preferred to the more recent one of Boehnke et al. (2013), as the latter tends to give too high Zr saturation levels (too low Zr saturation temperatures) in the temperature interval of our interest (Marxer and Ulmer 2019; their fig. 12). For calculation, we selected only acid samples ($SiO_2 > 63$ wt. %, corresponding to M < 2), for which the zircon saturation was likely reached, based on SiO_2–Zr (Hoskin et al. 2000; not shown) and M–Zr (Fig. 9i) variations. Calculated temperatures are mutually well comparable, for the Yaryn Khad (~800 °C), Uliin Arag (~720 °C), Toroin Range (744 and 781 °C), Bum (740 °C) and Aaj Bogd (773 and 788 °C) plutons (Fig. 9i). Exception are minor bodies in the Baaran Subzone that yield heterogeneous, but generally high, temperatures of *c.* 850 °C.

4.3.3. Whole-rock Sr–Nd isotope geochemistry

Eight newly acquired Sr–Nd isotopic compositions are given in ESM 5. Using the newly obtained U–Pb ages, the isotopic data were age-corrected to 350 Ma (Edren Subzone – Toroin Range, Bum Pluton in the Baaran Subzone), 330 Ma (Edren Subzone – Yaryn Khad and Uliin Arag plutons) and 285 Ma (Aaj Bogd Pluton of the Baaran Subzone).

All the granitoid samples, regardless of their regional position or intrusive age, are unevolved in terms of radiogenic isotopic signatures, with low initial Sr isotopic ratios and highly positive epsilon Nd values (Fig. 12a). The isotopic data are mutually well comparable: Toroin Range: $^{87}Sr/^{86}Sr_{350} \sim 0.7038$; $\varepsilon^{350}_{Nd} = +6.2$ and +5.2; Yaryn Khad and Uliin Arag: $^{87}Sr/^{86}Sr_{330} = 0.7036$–0.7038; $\varepsilon^{330}_{Nd} = +6.6$ to +6.2; Aaj Bogd: $^{87}Sr/^{86}Sr_{285} = 0.7036$ and 0.7042; $\varepsilon^{285}_{Nd} = +6.3$ and +6.1; Bum: $^{87}Sr/^{86}Sr_{350} = 0.7039$; $\varepsilon^{350}_{Nd} = +6.4$. The highly positive epsilon Nd values translate to
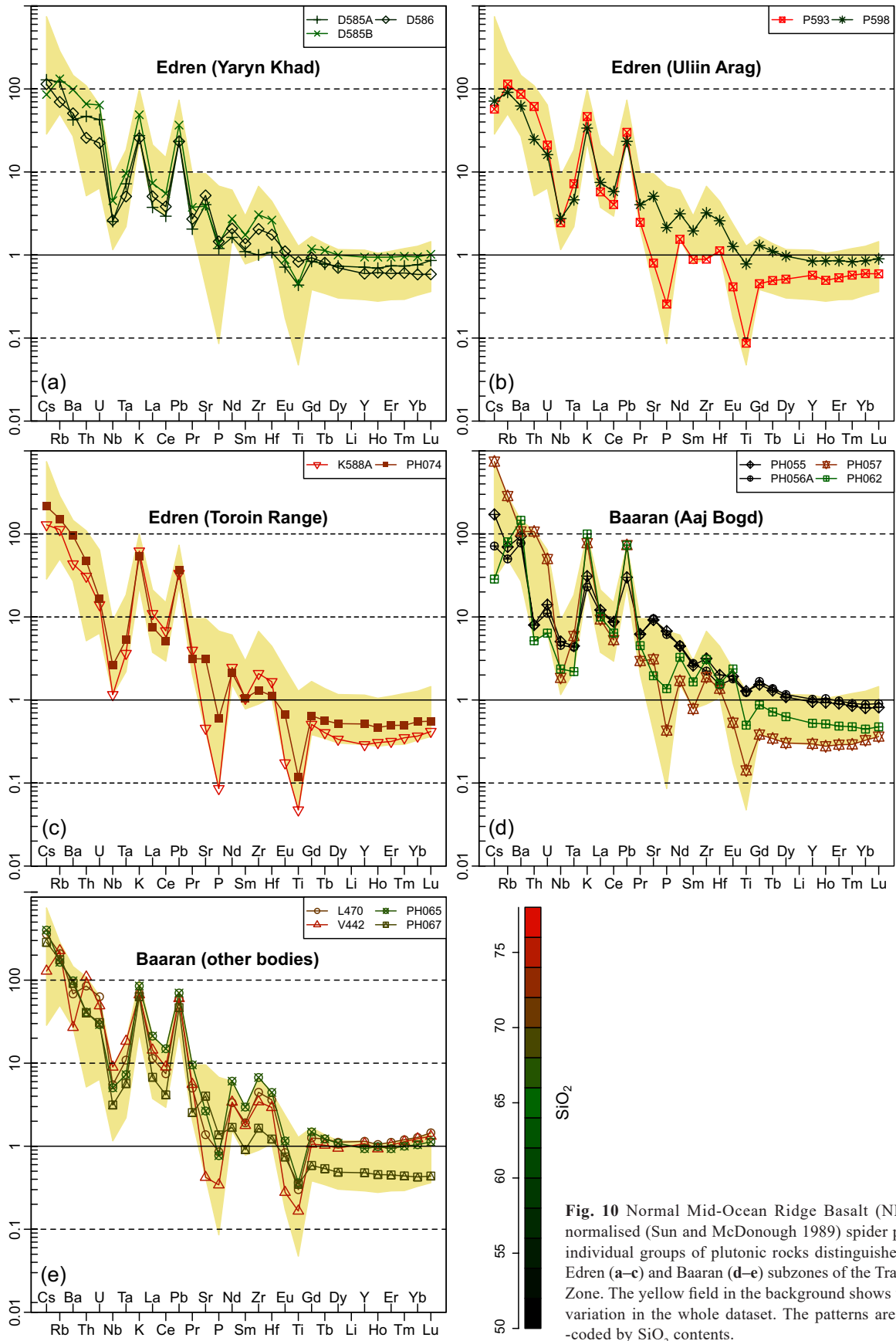
Fig. 10 Normal Mid-Ocean Ridge Basalt (NMORB) normalised (Sun and McDonough 1989) spider plots for individual groups of plutonic rocks distinguished in the Edren (**a–c**) and Baaran (**d–e**) subzones of the Trans-Altai Zone. The yellow field in the background shows the total variation in the whole dataset. The patterns are colour-coded by SiO$_2$ contents.
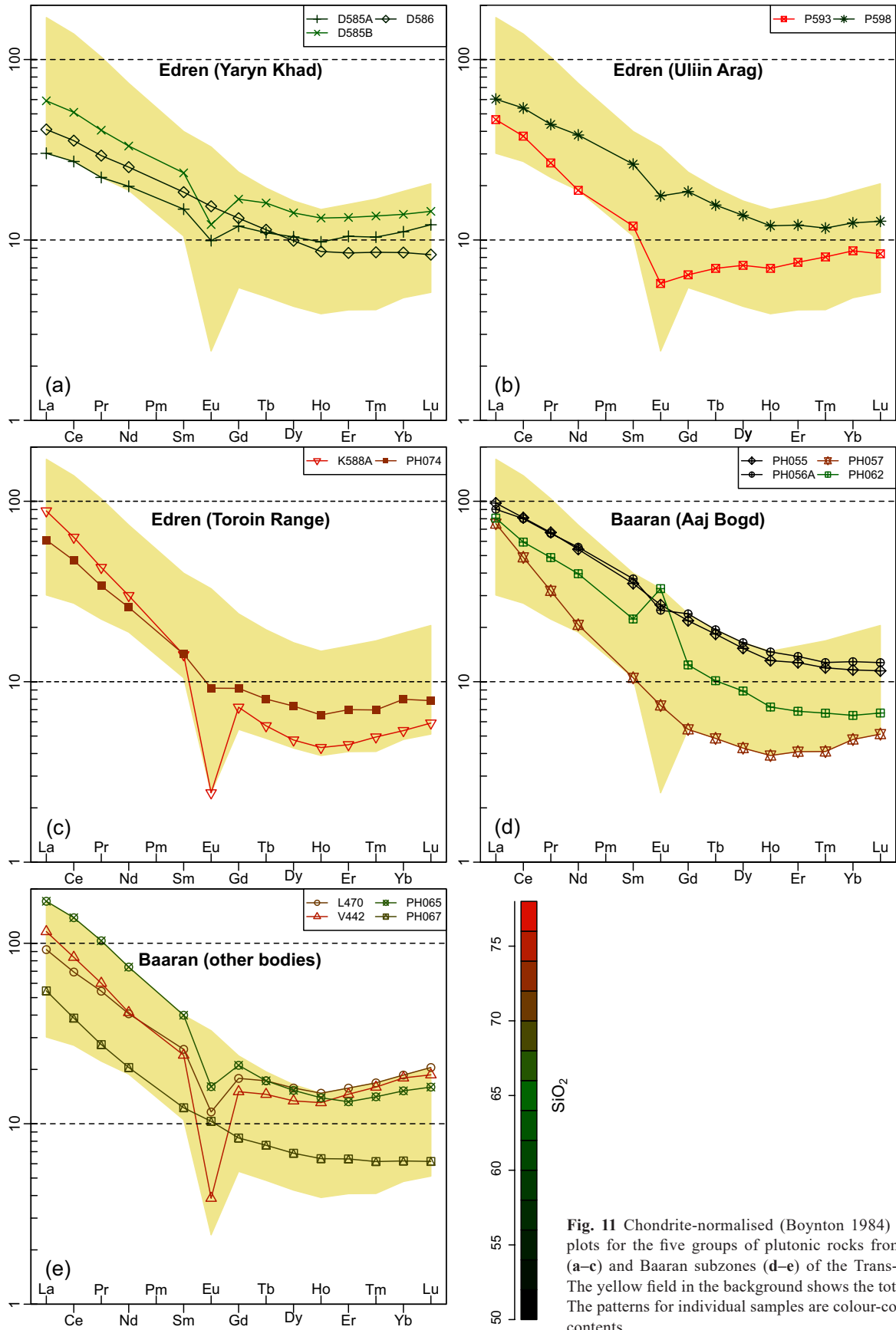
Fig. 11 Chondrite-normalised (Boynton 1984) REE spider plots for the five groups of plutonic rocks from the Edren (**a–c**) and Baaran subzones (**d–e**) of the Trans-Altai Zone. The yellow field in the background shows the total variation. The patterns for individual samples are colour-coded by SiO_2 contents.

Fig. 12a – Whole-rock $^{87}Sr/^{86}Sr_i$ vs. ε_{Nd}^i plot for the newly-obtained dataset, colour-coded by SiO_2 contents. Compositions of the Chondritic Uniform Reservoir (CHUR) (Nd: Jacobsen and Wasserburg 1980; Sr: Faure 1986), Depleted Mantle (DM) (Nd: Liew and Hofmann 1988; Sr: Rehkämper and Hofmann 1997) and Global Subducting Sediment (GLOSS II) (Plank 2014) are also shown for reference. **b** – Two-stage Nd evolution diag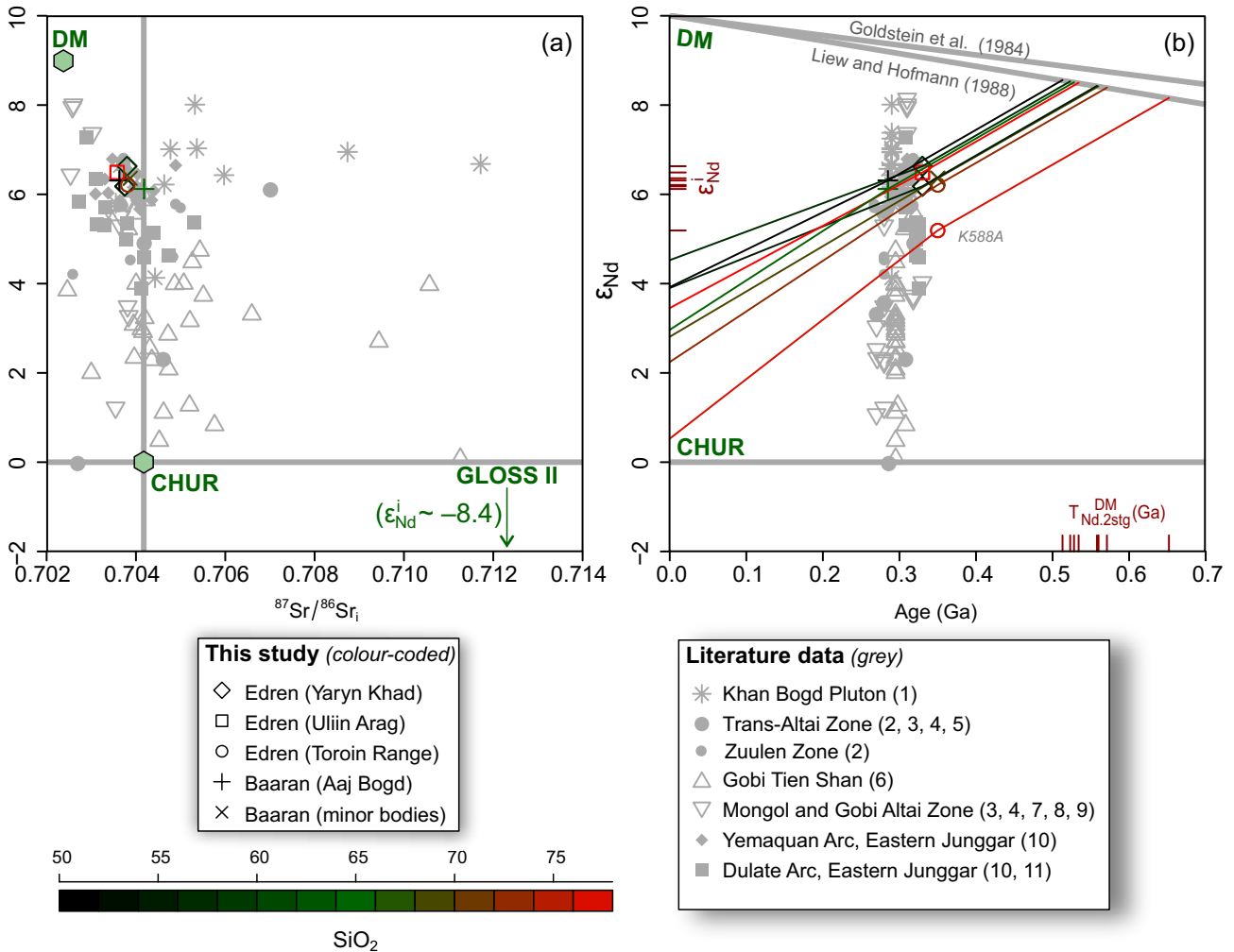ram. DM = Depleted Mantle evolution lines after Goldstein et al. (1984) and Liew and Hofmann (1988). The extra tick marks on the ordinate denote ε_{Nd}^i values, on the abscissa two-stage Depleted Mantle model ages, $T_{Nd.2stg}^{DM}$ (Liew and Hofmann 1988). Literature data plotted in both panels for comparison and denoted by grey symbols: (1) – Amar-Amgalan (2004, 2008); (2) – Yang et al. (2022); (3) – Kozakov et al. (2007); (4) – Savatenkov et al. (2016); (5) – Guy et al. (2015); (6) – Economos et al. (2012); (7) – Buriánek et al. (2016); (8) – Savatenkov et al. (2020); (9) – Cui et al. (2021); (10) – Liu et al. (2013); (11) – Zhang et al. (2018a).

low two-stage Depleted Mantle Nd model ages ($T_{Nd.2stg}^{DM}$ = 0.51–0.57 Ga; 0.65 Ga for sample K588A: Fig. 12b) suggesting short crustal residence for sources of the studied granitoids in both Edren and Baaran subzones, and an overall 'juvenile' character.

4.4. Amphibole thermobarometry, oxygen fugacity, and water contents in the magma

Crystallization temperatures (Tab. 2) for magmatic amphiboles from Yaryn Khad Pluton quartz diorite and monzo-diorite range from 741 to 796 °C and pressures from 0.07 to 0.11 GPa. Slightly higher P–T conditions (864–876 °C

and 0.20–0.22 GPa) were obtained for the amphibole inclusions in plagioclase. Crystallization temperatures for magmatic amphiboles from quartz monzodiorite of the Uliin Arag plutons range 739–765 °C and pressures 0.07–0.08 GPa. Amphiboles in the Aaj Bogd Pluton syenite PH062 were equilibrated at 718–748 °C and 0.05–0.07 GPa. This temperature matches conditions (calculated using the Thermocalc software v. TC321, Powell and Holland 1990) of the thermal metamorphism in wall-rock of garnet hornfels (740±69 °C). Amphibole composition of monzogranite from the Bum Pluton (PH067) reflects crystallization conditions of 718–773 °C and 0.07–0.09 GPa.

The Ridolfi et al. (2010) formulation also provides an estimate of oxygen fugacity during the crystallization of

Tab. 2 Summary of P–T values in selected plutonic rocks

Sample	D585A	D586	P598	PH062	PH067
Body	Yaryn Khad	Yaryn Khad	Uliin Arag	Aaj Bogd	Bum
Rock	Quartz monzonite	Quartz diorite	Qtz monzodiorite	Syenite	Monzogranite
Amphibole thermobarometry (Ridolfi et al. 2010)					
T (°C)	741 to 796*	756 to 784	739 to 765	718 to 748	756 to 773
P (GPa)	0.07 to 0.11*	0.09 to 0.10	0.07 to 0.08	0.05 to 0.07	0.07 to 0.09
DNNO	0.4 to 1.8	0.1 to 0.7	1.0 to 1.3	1.4 to 1.8	1.1 to 1.6
log fO_2	–13.4 to –11.9	–13.3 to –12.7	–13.9 to –13.6	–14.1 to –13.5	–13.5 to –13.0
H_2O melt (wt. %)	4.7 to 6.4	4.4 to 4.9	4.4 to 5.0	3.6 to 4.1	4.2 to 4.7
Plagioclase–hornblende thermometry (Holland and Blundy 1994)					
T (°C) ± 32 °C	650 to 694**	711 to 738	684 to 866	607 to 624	667 to 709

* rim (core = 864 to 876 °C and 0.20 to 0.22 GPa)

** rim (core = 785 to 802 °C at 0.20 GPa)

amphibole. Analogous amphibole compositions and the presence of the same Fe–Ti phases (magnetite, ilmenite ± titanite) yield similar oxygen fugacity for all the studied samples (log fO_2 = –14 to –12). The estimated water content in the melt is 3.6–6.4 wt. % (Tab. 2).

5. Discussion

5.1. Spatial and temporal distribution of Palaeozoic plutonic rocks in SW Mongolia

5.1.1. Age distribution of granitoid plutons in the Lake to Gobi Tien Shan zones

In SW Mongolia, Palaeozoic plutonic rocks are organised into generally NNE–SSW trending zones following major geotectonic domains and are generally younging southwards (Fig. 1, Fig. 13). Thus, the Cambrian–Ordovician subduction-related gabbros, diorites, quartz diorites and granodiorites (Rudnev et al. 2009; Hrdličková et al. 2010; Soejono et al. 2017) are restricted to the northerly **Lake Zone** where they belong to the so-called Ikh-Mongol Arc System (Janoušek et al. 2018 and references therein). Silurian–Devonian to Early Carboniferous plutonic rocks in the Chinese, Mongol and Gobi Altai developed in the continental-arc environment (e.g., Wang et al. 2006; Tong et al. 2012; Cai et al. 2015; Hanžl et al. 2016) but Carboniferous granite–migmatite domes have been described as well (Economos et al. 2008; Lehmann et al. 2017; Wang et al. 2021).

Carboniferous and Early Permian plutons dominate in the **Trans-Altai Zone**. Rare Devonian plutons of an arc character are known from the Gurvansaikhan area in the East (Gerel et al. 2005; Wainwright et al. 2011; Boldbaatar et al. 2019) as well as from the Eastern Junggar just south of the Aaj Bogd (Zhang et al. 2018b for review; Song et al. 2019). Early Palaeozoic ages are confined to the Zuulen accretionary belt in the eastern

segment of this zone (Jian et al. 2014) and in Yemaquan Arc of the Eastern Junggar (Xu et al. 2013; Zhang et al. 2017 for review).

There is a dearth of age data on granitoids from the **Gobi Tien Shan** and **South Gobi**. Late Palaeozoic continental arc granitoids dominate in Gobi Tien Shan (310–290 Ma; Hanžl et al. 2008; Yarmolyuk et al. 2008; Kröner et al. 2010; Economos et al. 2012) while those of Late Carboniferous to Early Permian active continental margin and Middle Permian post-collisional extensional setting are known from the South Gobi (Guy et al. 2014a; Zhang et al. 2021).

Three magmatic phases (389–350, 317–289, and 244–211 Ma) were distinguished in SW Mongolia, albeit on a relatively limited dataset (Cai et al. 2015). On the contrary, the original work of Zhang et al. (2017) distinguished nine discrete Palaeozoic magmatic events in the Chinese Altai, Eastern Junggar and adjacent regions, whereby three of them (359–330, 330–296, and 296–275 Ma) correspond with our data from the north-western Trans-Altai Zone.

5.1.2. Carboniferous plutons of the north-western Trans-Altai Zone

Newly determined ages of samples PH074 (347 ± 4 Ma) and PH067 (352 ± 1 Ma) correlate well with a published age of 348 ± 1 Ma (Yarmolyuk et al. 2008) from granodiorite corresponding to the Bum Pluton on the northern slopes of the Aaj Bogd Range. Late Devonian to Early Carboniferous ages ranging from 382 to 354 Ma were obtained for granodiorites and alkaline granites in the Bulgan segment of the easternmost Dulate Arc (Zhou et al. 2009; Shen et al. 2011; Tong et al. 2012; Cai et al. 2015; Song et al. 2019). Plutons spanning 350–340 Ma in age (Zhang et al. 2017 for review) are scattered in Yemaquan Arc – a continuation of the Baytag Subzone to the Eastern Junggar (Fig. 1). To the east, no rocks of similar age are yet known in TAZ, but contemporaneous syntectonic plutons are exposed in the Gobi Altai Zone

(Hrdličková et al. 2008; Izokh et al. 2011; Kröner et al. 2017; Lehmann et al. 2017) and, rarely, in the Mongol Altai (Cai et al. 2015).

The newly obtained age of 331 ± 1 Ma for the biotite granite K615 of the Yaryn Khad Pluton is in agreement with published ages for gabbronorite from the western part of the same body (316 ± 3 Ma: U–Pb zircon SHRIMP, 330 ± 3 Ma: Ar–Ar biotite) (Izokh et al. 2011) and with c. 330 Ma ages found in Edren Range granitoids further SE (Hanžl et al. 2008; Yarmolyuk et al. 2008). Similar ages were also reported more to the west, from the Bodonch area in the westernmost Trans-Altai Zone (granite: 330 ± 4 Ma, Kozakov et al. 2007; diabase dyke: 335 ± 4 Ma, Cai et al. 2014). Few such data were published from the Yemaquan Arc in the Eastern Junggar (Li et al. 2012; Xu et al. 2015), from granite in southern Gobi west of the Khan Bogd Pluton (Ji et al. 2020) and from its tonalite country-rock (Heumann et al. 2012).

The c. 310 Ma volcanic-arc granitoids, some of which were termed "adakite" (Zhang et al. 2018a) are common in the Eastern Junggar (Liu et al. 2013). Similarly, Late Pennsylvanian (315–307 Ma) subduction-related granites (Guy et al. 2014b; Zhou et al. 2021) and c. 300 Ma old anorogenic granites (Shen et al. 2011; Liu et al. 2013; Guy et al. 2014b). were described in the eastern Trans-Altai Zone. Any evidence for contemporaneous magmatism is missing in our dataset.

5.1.3. Early Permian plutons of the north-western Trans-Altai Zone

Aaj Bogd Pluton (dated here at c. 285 Ma), coeval granites from Eej Khayrkhan Mountain (c. 274 Ma, Kozakov et al. 2007), or younger phase of the Bum Pluton (c. 294 Ma, Yarmolyuk et al. 2008) in the north-western Trans-Altai Zone are situated in a girdle of Early Permian plutons with characteristic circular or oval shapes and alkaline affinity. This plutonic belt extends from the Dulate Arc (290–267 Ma; Tong et al. 2014 for review) eastwards, through the Trans-Altai Zone to the alkaline Khan Bogd Pluton in the Gurvansaikhan Subzone (293–283 Ma; Kovalenko et al. 2006; Heumann et al. 2012; Guy et al. 2014b; Zhou et al. 2021).

North of the Trans-Altai Zone, contemporaneous A-type granites (c. 285 Ma), associated with volcanic rocks, were also described from an E–W trending belt in the Lake Zone known as the Gobi Altai Rift (Chernov
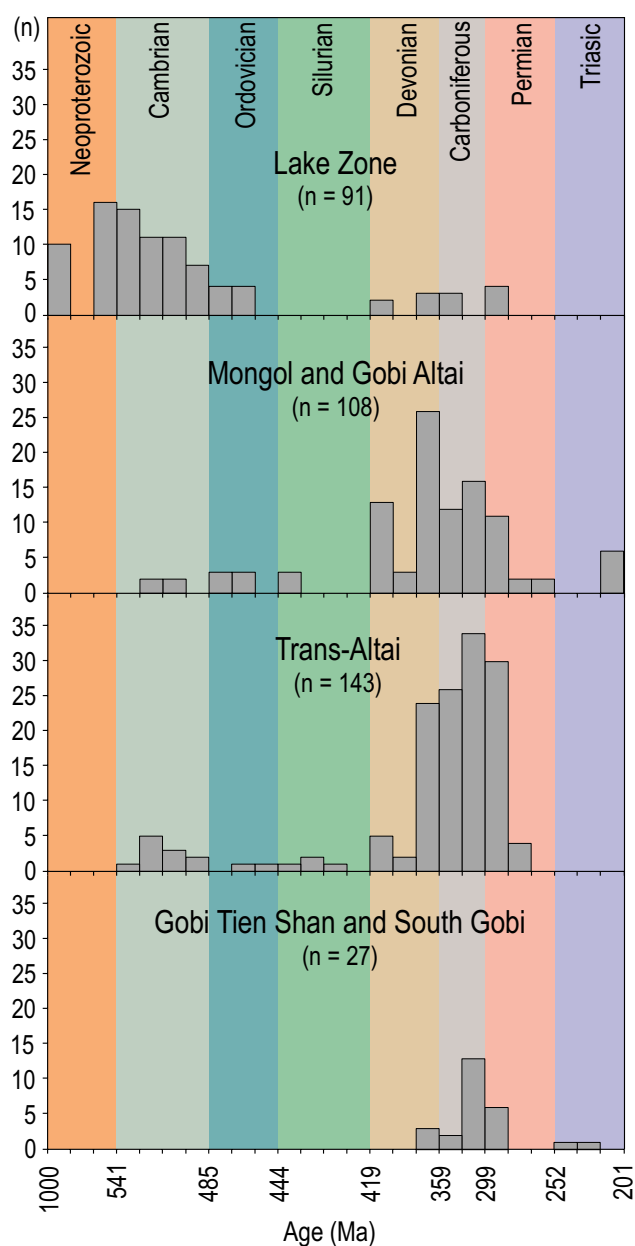

⇦

Fig. 13 Temporal correlation of plutonic rocks in the main geological domains of SW Mongolia and adjacent parts of NW China. Data sources: **Lake Zone** – Gibsher et al. (2001), Kozakov et al. (2002), Helo et al. (2006), Demoux et al. (2009), Hrdličková et al. (2010), Kröner et al. (2010), Jian et al. (2014), Kozlovsky et al. (2015), Soejono et al. (2016), Buriánek et al. (2017), Janoušek et al. (2018), Rudnev et al. (2019, 2021), Skuzovatov (2021); **Mongol and Gobi Altai** – Bibikova et al. (1992), Helo et al. (2006), Kozakov et al. (2007, 2011), Hrdličková et al. (2008); Lamb et al. (2008), Kröner et al. (2010, 2017), Izokh et al. (2011), Jiang et al. (2012), Burenjargal et al. (2014, 2016), Cai et al. (2015), Hanžl et al. (2016), Buriánek et al. (2017), Lehmann et al. (2017), Soejono et al. (2017), Zhang et al. (2017 and references therein), Song et al. (2019), Hong et al. (2021); **Trans-Altai Gobi** (and adjacent Eastern Junggar) – Kovalenko et al. (2006), Kozakov et al. (2007), Yarmolyuk et al. (2008), Wainwright et al. (2011), Heumann et al. (2012), Kozlovsky et al. (2012), Liu et al. (2013), Cai et al. (2014), Guy et al. (2014a), Jian et al. (2014), Zhu et al. (2014, 2016), Zhang et al. (2017 and references therein), Boldbaatar et al. (2019), Song et al. (2019), Yang et al. (2019), Ji et al. (2020), Wang et al. (2021), Zhang et al. (2021), Zhou et al. (2021), Yang et al. (2022; **Gobi Tien Shan and South Gobi** – Kozlovsky et al. (2005, 2012), Hanžl et al. (2008), Yarmolyuk et al. (2008), Kröner et al. (2010), Heumann et al. (2012), Taylor et al. (2013), Zhang et al. (2021).

and Kovalenko 2008; Buriánek et al. 2012; Kozlovsky et al. 2015). Gabbro-norite and monzogabbro-diorite post-collisional intrusions in the southeastern Chinese Altai were dated to 283–275 Ma (Cui et al. 2021).

5.2. Neodymium model ages and zircon inheritance

Age spectra of the studied rocks are rather homogenous, nearly without inheritance (Figs 5–7). If found, the inheritance is not older than Phanerozoic, consistent with the Cryogenian–Cambrian two-stage Depleted Mantle Nd model ages ($T_{Nd.2stg}^{DM}$ = 0.66–0.52 Ga; Fig. 12b). Consulting the literature data in Fig. 12a, we conclude that analogous Sr–Nd compositions are characteristic especially of Yemaquan and Dulate arcs in Eastern Junggar (Liu et al. 2013; Zhang et al. 2017). Furthermore, our newly-obtained data plot at the more primitive end of the Mongol and Gobi Altai data array, but are considerably more primitive than the Gobi Tien Shan data, showing ε_{Nd}^i values often much lower than + 5.

Cambrian–Devonian inheritance. Cambrian and Early Ordovician inheritance in biotite granite PH074 (Toroin Range in Edren Subzone) may reflect the presence of the Lake Zone-type crust in the magma source as Guy et al. (2015) and Nguyen et al. (2018) suggested. Early Devonian zircons encountered in the Bum (*c.* 403 Ma, PH067) and Aaj Bogd (*c.* 394 Ma, PH055) plutons likely represent xenocrysts captured from the Devonian volcanic country rocks, common in the Trans-Altai Zone (Ruzhentsev et al. 1985; Hanžl and Krejčí eds 2008; Hanžl et al. 2020).

Carboniferous inheritance. The inherited age of *c.* 355 Ma from Permian quartz syenite PH065 in Baaran Subzone is close to the age of the Bum Pluton (*c.* 350 Ma: Yarmolyuk et al. 2008 and this paper) as well as andesites of the NW Trans-Altai Zone (*c.* 351 Ma, Nguyen et al. 2018).

5.3. Emplacement mechanism and P–T conditions

5.3.1. Edren Subzone

Even though the sampled granitoid bodies in the Edren Subzone are mostly masked by Cenozoic cover and faults, an oval shape with steep contacts and well-developed thermal aureole are characteristic of the Yaryn Khad Pluton. This, together with dip-slip lineation in the foliated metabasalts at the endocontact, could indicate diapiric ascent of the pluton with concomitant downward transfer of its host rocks (Miller and Paterson 1999; Paterson et al. 2014). The P–T conditions of crystallization obtained from individual samples (Tab. 2) were 0.07 to

0.11 GPa and 740 to 795 °C using the method of Ridolfi et al. (2010). This agrees well with mean zircon saturation temperatures of ~800 °C calculated following the model of Watson and Harrison (1983). Plutons of the Toroin Range are ellipsoidal in shape and contain abundant xenoliths of adjacent volcanic rocks. The angular xenoliths are commonly well-arranged or even accumulated in steep monogenic enclave swarms (Didier and Barbarin 1991). No thermal aureole was detected.

5.3.2. Aaj Bogd Pluton

The distribution of ages indicates a multi-phase magmatic evolution of the Aaj Bogd Pluton. Mafic rocks in the core of the pluton are *c.* 285 ± 1 Ma old (weighted average of ages for quartz monzodiorite: 294 ± 3 Ma and monzogabbro: 284 ± 1 Ma). The main granite–syenite mass of the Aaj Bogd Pluton is slightly younger (282 ± 1 Ma). The oval shape of the body with septa of host metasediments reoriented from their original E–W trend to a concentric arrangement, together with 'onion skin' zoned structure could indicate ballooning (Paterson et al. 1996; Molyneux and Hutton 2000; Dietl and Koyi 2002) as the emplacement mechanism.

Compared to the results of amphibole–plagioclase thermometry of Holland and Blundy (1994), the amphibole-based approach of Ridolfi et al. (2010) yields significantly higher temperatures in all measured samples (Tab. 2). The low temperatures obtained by the method of Holland and Blundy (1994) probably reflect subsolidus re-equilibration between plagioclase and amphibole during cooling (e.g., Cornejo and Mahood 1997; Tetsopgang et al. 2011). On the other hand, the P–T conditions of crystallization obtained from the Aaj Bogd syenite (*c.* 0.05–0.07 GPa and 720 to 750 °C) according to Ridolfi et al. (2010) are consistent with the mineral assemblage in the contact aureole (cordierite–garnet–sillimanite). Further, the temperature (~740 °C) calculated by Thermocalc using the KFMASH system (Powell and Holland 1990) in the contact hornfels corresponds well with the syenite data. Mean zircon saturation temperatures, interpreted as the best estimate of the liquidus temperatures, are expectedly elevated (773 and 788 °C).

5.4. Whole-rock geochemical constraints on geotectonic setting

Despite limitations and criticism, especially concerning the late- to post-collisional granitic suites, whole-rock geochemical compositions of magmatic rocks are frequently used to decipher the geodynamic setting (e.g., Pearce et al. 1984; Pearce 1996; Janoušek et al. 2016; Bonin et al. 2020; Pearce et al. 2021 and references therein). Also we consider some of the commonly used
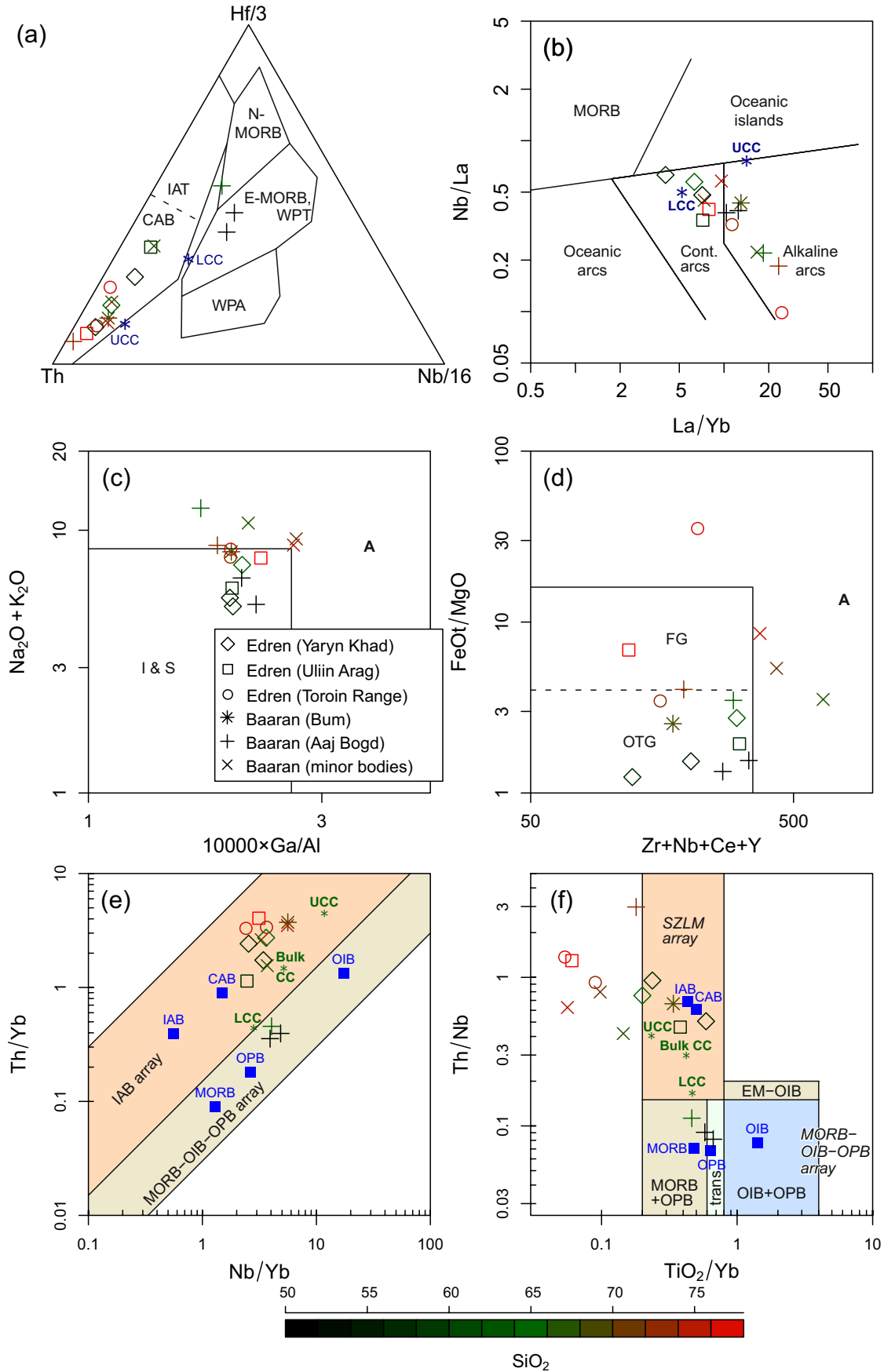
geotectonic diagrams as useful projections that merit a discussion here.

In the Th–Hf/3–Ta ternary plot of Wood (1980) (Fig. 14a), the three most mafic (monzonitic–syenitic) Aaj Bogd lithologies display a clear within-plate affinity (EMORB/within-plate tholeiites, WPT) not influenced by subduction and/or mature crustal contamination. The rest of the dataset is Th-rich and Nb-poor, falling into the continental-arc basalts (CAB) field. These latter samples thus seem to represent either magma derived from a mantle wedge that was metasomatised by hydrous fluids and/or partial melts of subducted sediments (Pearce et al. 2005), or by crustal anatexis of former arc-related material. Indeed, various crustal averages also project into the same field of this graph (e.g., Taylor and McLennan 1995).

In the binary plot of La/Yb vs. Nb/La of Hollocher et al. (2012), the samples from the Edren Subzone exhibit an affinity to standard continental arcs, while those from the Baaran Subzone have a more alkaline character (Fig. 14b). In fact, the minor Permian bodies in the Baaran Subzone (i.e., except the Aaj Bod Pluton proper and ~350 Ma Bum monzogranite PH067) have high (>800 °C) zircon saturation temperatures (Fig. 9i) and are rather low in Fe (Fig. 8d) and rich in HFSE (Fig. 10e). Therefore, they have some characteristics of anorogenic (A-type) granitoids. This can be demonstrated in various discrimination diagrams designed by Whalen et al. (1987), such as $10{,}000 \times Ga/Al$ vs. $Na_2O + K_2O$ and $Zr + Nb + Ce + Y$ vs. FeOt/MgO (Fig. 14c–d). Still, our samples also display some important differences from typical A-type granitoids, most importantly intermediate Ga, as well as low Nb and Ta contents. The latter feature is demonstrated by negative anomalies in the NMORB-normalised patterns (Fig. 10e). Having such a transitional character, the suite is best viewed as post-collisional alkaline, as defined by Sylvester (1989).

⇦

Fig. 14 Geotectonic diagrams based on whole-rock geochemical compositions. **a** – Triangular plot Th–Hf/3–Nb/16 of Wood (1980). IAT – Island-Arc Tholeiites, CAB – Calc-Alkaline Basalts, N-MORB – Normal Mid-Ocean Ridge Basalts, E-MORB – Enriched Mid-Ocean Ridge Basalts, WPT – Within-Plate Tholeiites, WPA – Within-Plate Alkali Basalts. **b** – Binary plot of La/Yb vs. Nb/La of Hollocher et al. (2012) to distinguish various types of arc-related mafic igneous rocks from MORB and ocean-island basalts. **c, d** – Binary plots $10{,}000 \times Ga/Al$ vs. $Na_2O + K_2O$ and $Zr + Nb + Ce + Y$ vs. FeOt/MgO for recognition of A types (Whalen et al. 1987), average of the A-type granites is labelled 'A'. Fields of ordinary S- and I-type granitic rocks ('I & S') or of ordinary and fractionated granites ('OTG' and 'FG'), are also shown. **e–f** – Binary diagrams plotting Nb/Yb vs. Th/Yb and TiO_2/Yb vs. Th/Nb (Pearce et al. 2021). The 'MORB–OIB–OPB array' is formed by average NMORB, OIB (Ocean Island Basalt) and OPB (Oceanic Plateau Basalt) compositions taken from Sun and McDonough (1989) and Pearce et al. (2021). In all diagrams, 'Bulk CC', 'UCC' and 'LCC' refer to the bulk, upper and lower continental crustal averages (Taylor and McLennan 1995). IAB – Island-Arc Basalts, CAB – Continental-Arc Basalts, SZLM – Subduction-Modified Lithospheric Mantle.

In the Nb/Yb vs. Th/Nb diagram of Pearce et al. (2021) (Fig. 14e), three monzonitic–syenitic rocks from the Aaj Bogd Pluton fall onto the 'mantle array' formed by average NMORB, OIB (Ocean Island Basalt) and OPB (Oceanic Plateau Basalt) compositions. Therefore, they have no recognizable continental crustal component, and instead display an OPB affinity, i.e., seem to be strongly influenced by a fertile, asthenospheric mantle. The rest of the data set is strongly contaminated by continental crust or is wholly crustal derived, as it projects onto the IAB array, close to the bulk continental crust average (Taylor and McLennan 1995).

This is further confirmed by the binary diagram TiO_2/Yb vs. Th/Nb (Pearce et al. 2021) (Fig. 14f), where the three most mafic Aaj Bogd samples fall close to the ideal OPB composition. The rest of the dataset falls into the SZLM domain (subduction-modified lithospheric mantle, together with various crustal averages) or, for the most siliceous samples, is shifted to the left of this field, presumably due to crystal fractionation.

5.5. Possible petrogenesis and sources of the crustal melts

The importance of crystal fractionation and accumulation in the Aaj Bogd Pluton is documented by REE patterns (Fig. 11d). For instance, the convex down, Eu-enriched pattern in syenite PH062 is characteristic of granitoids affected by K-feldspar accumulation. On the other hand, the REE pattern of the granite PH057, poor in MREE + HREE, and lacking an Eu anomaly, may reflect a high degree of fractionation of an Amp-dominated assemblage either with, or without accessories such as apatite and zircon. The lack of an Eu anomaly in this case may reflect relatively oxidizing conditions in a water-rich magma (Drake 1975).

While three of most mafic (monzonitic–syenitic) samples from the Aaj Bogd Pluton probably come from the Earth's mantle, but the studied rock types appear, fully or at least largely, crustally derived. Intermediate to acid samples ($SiO_2 > 52$ wt. %) were plotted on the (CaO/(MgO + FeOt) vs. Al_2O_3/(MgO + FeOt) binary plot (Fig. 15a) of Gerdes et al. (2000), designed to distinguish various crustal sources of granitic melts. The acid ones fall mainly into the field of experimental partial melts produced from metagreywackes; these would be, however, very difficult to distinguish from products of orthogneiss melting solely on geochemical grounds (Sylvester 1998). On the other hand, intermediate samples from the Edren Subzone and the Bum monzogranite require melting of intermediate to basic metaigneous sources.

According to the Al_2O_3/(FeOt + MgO) – 3 × CaO – 5 × K_2O/Na_2O (wt. %) ternary plot (Laurent et al. 2014), the intermediate samples seem to reflect a high-K me-
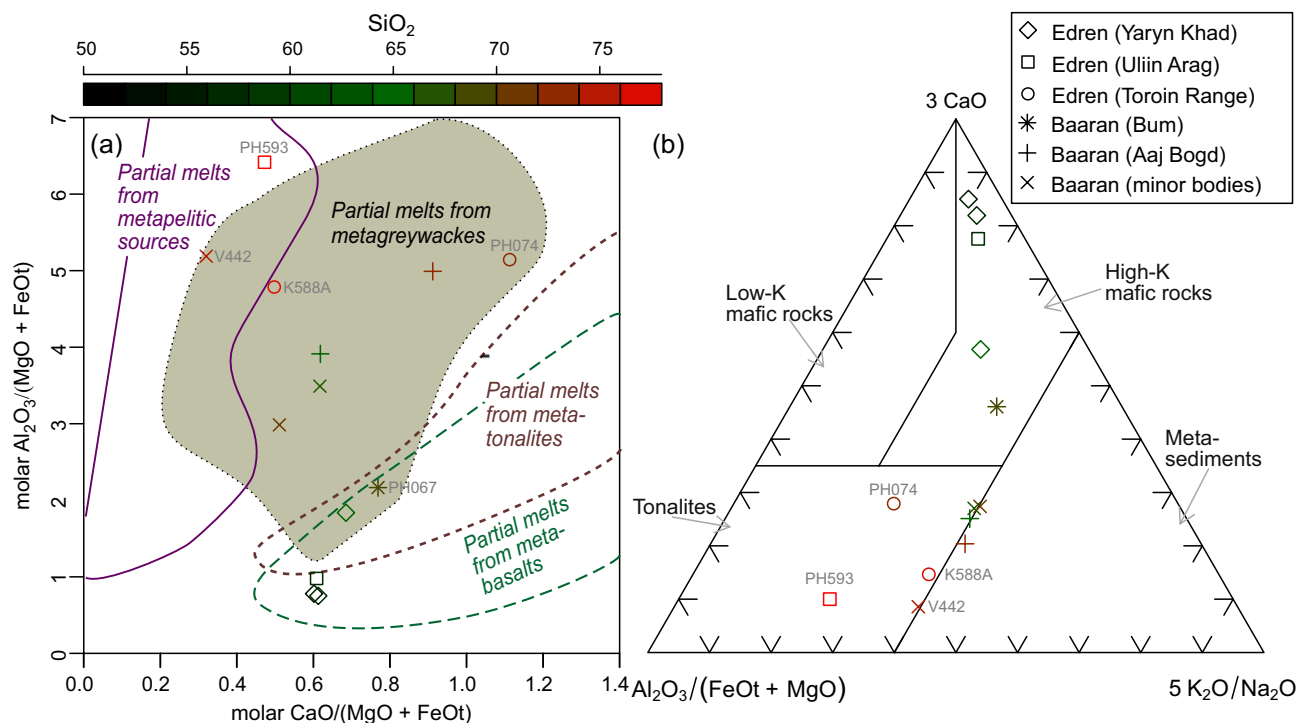
Fig. 15 Diagrams distinguishing granitic melts derived from various crustal sources (based on experimental data). Note that only acid–intermediate samples ($SiO_2 > 52$ wt. %) are shown. **a** – Binary plot ($CaO/(MgO + FeOt)$ vs. $Al_2O_3/(MgO + FeOt)$ in mol. % after Gerdes et al. (2000). **b** – Ternary plot $Al_2O_3/(FeOt + MgO) – 3×CaO – 5×K_2O/Na_2O$ (wt. %) of Laurent et al. (2014).

tabasic source, while the more siliceous ones could have originated by remelting of the metatonalitic rather than mature metasedimentary (pelitic) crust (Fig. 15b). The diagram is in principle not capable of distinguishing tonalite- and greywacke-derived melts, which may result in mismatch in classification of the sample PH593 between Fig. 15a and b.

5.6. Towards a consistent petrogenetic model for Carboniferous–Permian plutonism in the Trans-Altai Zone

In the studied region, two diachronous and compositionally contrasting granitic associations are present: (1) Mississippian, arc-related, calc-alkaline, and (2) Early Permian, alkali-rich.

The Mississippian magmatic activity in the north-western Trans-Altai Zone can be split into Tournaisian (*c.* 350 Ma) and Viséan/Serpukhovian (*c.* 330 Ma) pulses, both clearly subduction-related. This is documented by the arc-like enrichment of LILE (mobile in hydrous fluids released from the subducting slab and/or in oceanic sediment-derived melt) over geochemically conservative HFSE (contributed solely by the mantle wedge) (Saunders et al. 1991; Pearce and Peate 1995; Tatsumi and Eggins 1995; Pearce et al. 2005). This LILE over HFSE enrichment results in deep negative Nb–Ta anomalies in NMORB-normalised spiderplots (Fig. 10) and represents

the rationale behind most of the geotectonic diagrams (Fig. 14) that indeed point to the subduction-related origin of the studied Mississippian samples.

Mississippian arc-related magmatic activity in the Trans-Altai Zone is also evidenced by volcanic rocks from Baaran and Baytag subzones further south. These 351.0 ± 5.9 to 325.6 ± 1.4 Ma basalts to rhyolites have whole-rock geochemical and Nd–Hf isotopic compositions compatible with an origin in a youthful and geochemically primitive (freshly accreted) active continental margin (Nguyen et al. 2018).

Among the post-tectonic Early Permian plutons (294–274 Ma) in the north-western Trans-Altai Zone, the Aaj Bogd Pluton (*c.* 285 Ma) is the most eye-catching due to its round shape and concentric arrangement of host-rock septa (Fig. 2). Together with the minor granitic bodies in the Baaran Subzone, it intruded shallow crust composed of a Late Devonian–Early Carboniferous accretionary complex.

Nearly all studied samples from minor Permian granitic bodies of the Aaj Bogd mountain range show a weak A-type affinity (Whalen et al. 1987) and, since they have comparably high Y/Nb ratios (1.44–2.51), they resemble the A_2 group *sensu* Eby (1990). Granitoids of the A_2 group are interpreted as having been derived by high-T, water-deficient partial melting of tonalites–granodiorites (Creaser et al. 1991; Patiño Douce 1997), devolatilised tonalitic gneisses (Skjerlie and Johnston 1992) or even

metaigneous granulitic residua, stripped of (ordinary) granitic melt during some previous, unrelated geotectonic event (Collins et al. 1982; Clemens et al. 1986). Likewise, partial melting of previously unmelted metatonalites, or restites from which I-type granitic melt had been extracted earlier, were proposed explanations of the origin of post-collisional alkaline granites by Sylvester (1989). In all cases mentioned above, the protolith is assumed to have been through at least one cycle of continent–continent collisional or igneous-arc magmatism (Eby 1990).

Given the whole-rock geochemical signature of the studied Permian granitoids, in particular the strong LILE and Pb enrichment and presence of sizeable negative Nb–Ta anomalies in NMORB-normalised spider plots, the most likely genetic model indeed seems partial melting of pre-existing, arc-related metaigneous rocks. The likely setting was a back-arc or, more likely, a developing rift (Yarmolyuk et al. 2008) that dissected a pre-existing arc domain. Based on the primitive (highly radiogenic Nd and unradiogenic Sr) isotopic signatures, and young (Cryogenian to Cambrian) Nd model ages, it likely was freshly accreted Phanerozoic oceanic arc. It could have been Cambrian–Ordovician and/or Mississippian in age and, indeed, zircon xenocrysts of both age groups have been detected in the inheritance spectra of the studied granitoids. In the former case it could belong to the underplated metaigneous rocks of the Ikh-Mongol Arc System (Guy et al. 2015; Janoušek et al. 2018) with, or without, metagreywackes of the related Altai accretionary wedge (Jiang et al. 2017; Soejono et al. 2021). However, taking into account the intrusion of the studied plutons into Devonian–Early Carboniferous arc-related country rocks, and the low $T_{Nd.2stg}^{DM}$, lower than those characterising the Ikh-Mongol Arc System, the latter hypothesis seems more likely.

While the arc-like geochemistry of the Permian granites from the minor bodies in the Baaran Subzone is clearly inherited from the arc-related source (see Bonin et al. 2020 and references therein for further explanation and global examples of this phenomenon), the monzonitic–syenitic rocks of the Aaj Bogd Pluton correctly point to an intra-plate geotectonic setting. As shown by Fig. 14e–f, the mafic magmas most likely shared the same asthenospheric, or at least asthenosphere-influenced, source, largely unmodified by previous subduction-related metasomatism.

The asthenospheric rise could be related to rifting or ascent of the Tarim mantle plume (e.g., Zhang et al. 2010; Yarmolyuk et al. 2013). Indeed, the volcanic activity of the Tarim large igneous province occurred in three episodes within the overall time span of 300–270 Ma (Liu and Leng 2020 for review), thus overlapping with the age of A-type plutons in the Trans-Altai Zone (*c.* 285 Ma).

Although the radius of the Permian Tarim plume in the Precambrian basement below the Tarim Basin (Xu et al. 2020) was estimated to be *c.* 200 km (Liu and Leng 2020), it does not seem likely that the plume significantly influenced Permian magmatic activity in the thousands kilometres long accretionary belt along the southern Altai.

The rifting scenario would correspond with a linear arrangement of the Early Permian A-type plutons over a distance of more than 1600 km from the Dulate Arc, through the Trans-Altai Zone to the Khan Bogd Pluton. On the other hand, this linear arrangement can be explained through the association of the plutons with major Permian strike-slip zones widespread in the CAOB (Buslov 2011 for review).

In contrast, the geochemistry of the Permian Gobi Tien Shan rift-related mafic rocks was thought to indicate a significant role for metasomatised mantle wedge, contaminated during the preceding (Carboniferous) arc stage by hydrous fluids/melts from the subducted oceanic crust (Kozlovsky et al. 2006).

5.7. The general geotectonic framework

The Trans-Altai Zone (Fig. 16) is a collage of Palaeozoic arcs, back- and fore-arc basins with rare ophiolites accreted to the northerly Gobi Altai Zone in Late Carboniferous times (Xiao et al. 2009) and can be correlated with the westerly adjacent Dulate Arc of Devonian–Carboniferous age (Long et al. 2012). The Trans-Altai Zone is a part of the accretionary orogen developed between the Zavkhan–Baidrag block (Fig. 1) in the north and the Gobi Tien Shan or South Gobi blocks in the south (e.g., Kröner et al. 2010) above a subduction zone retreating southwards in the present-day coordinates (Guy et al. 2015). However, modern reconstructions indicate that the whole Mongolian tract of the CAOB faced east before a major Late Carboniferous clock-wise rotation (Edel et al. 2014; Xiao et al. 2018). In particular, the Late Palaeozoic geotectonic model of Xiao et al. (2015, 2018) for CAOB fits well with the pre-Mesozoic geology of the western Trans-Altai Gobi (e.g., Ruzhentsev and Pospelov 1992; Hanžl and Krejčí eds 2008; Kröner et al. 2010) and could serve as a basis for the geotectonic interpretation of the studied granitoids.

The presented data from the small NW part of the Trans-Altai Zone record three different magmatic events: (1) *Tournaisian* (high-K calc-alkaline) along the boundary between Edren and Baaran subzones, (2) *Viséan/Serpukhovian* (also high-K calc-alkaline) in the Edren Subzone and (3) *Cisuralian* (post-orogenic) in the Aaj Bogd Range of the Baaran Subzone. These magmatic events reflected Late Palaeozoic subduction- to post-collisional extension-related magmatic evolution of the
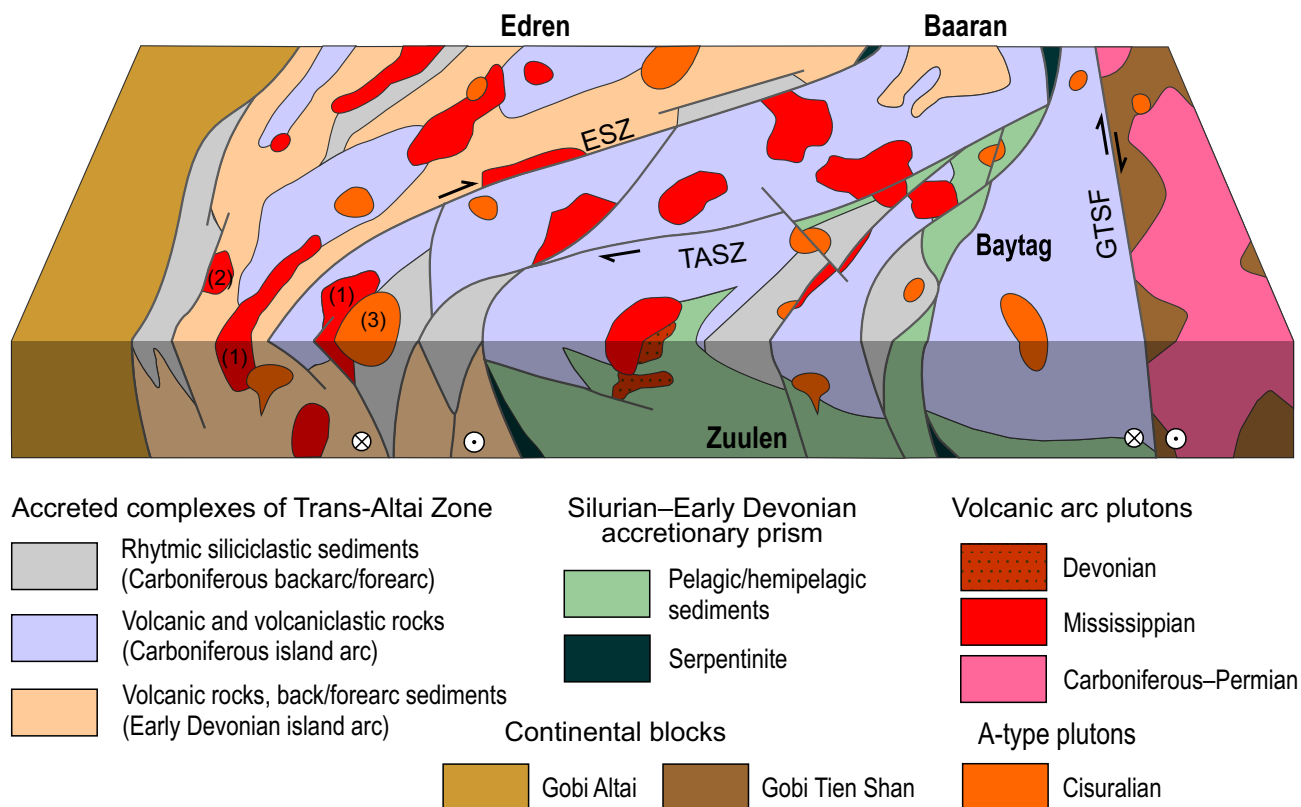
Pavel Hanžl, Vojtěch Janoušek, Kristýna Hrdličková, David Buriánek, Ochir Gerel, Battushig Altanbaatar, John M. Hora, Petr Čoupek

Fig. 16 Position of granitic bodies in idealised 3D section across the Trans-Altai Gobi between northerly Gobi Altai and southerly Gobi Tien Shan domains. ESZ – Edren Shear Zone; TASZ – Trans-Altai Shear Zone; GTSF – Gobi Tien Shan Fault. Numbers in brackets represent studied plutons: (1) – Tournaisian, (2) – Viséan–Serpukhovian and (3) Cisuralian.

Trans-Altai Zone sandwiched between Gobi Altai Zone in the north and Gobi Tien Shan Zone in the south (Fig. 17).

Tournaisian granitoids are interpreted as related to an active continental margin, in agreement with the previous conclusions of Yarmolyuk et al. (2008). These granitoids were synchronous with volcanism in Baaran and Baytag zones developed above the north-dipping (in the present-day coordinates) subduction zone (Nguyen et al. 2018). This Early Carboniferous volcanic arc grew on the previous Silurian–Devonian oceanic and island-arc sequences accreted to the Gobi Altai continental margin (Fig. 17a). Early Carboniferous pulse of the Bum Pluton could represent lower parts of the magmatic system that intruded the roots of the Tournaisian magmatic arc, while the contemporaneous Toroin Range Pluton seems shallower, closely related with coeval volcanic rocks.
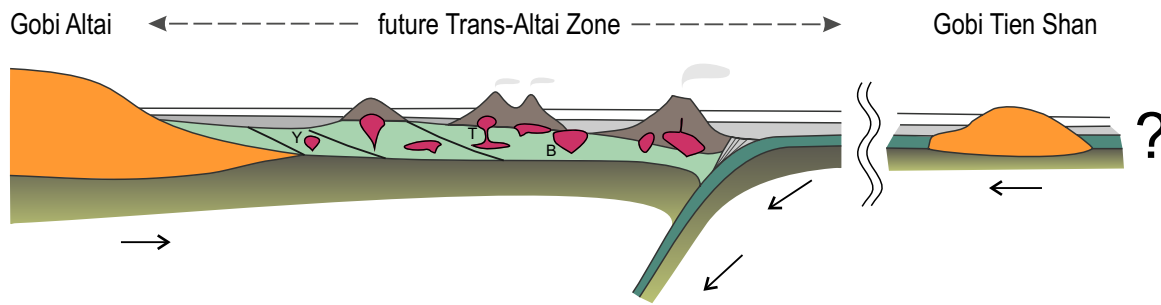
Viséan/Serpukhovian arc-related granitoids found in the Edren Zone have arc-like geochemical signatures (Fig. 14). On the other hand, both intraplate and subduction-related features were described in the Yaryn Khad Pluton by Izokh et al. (2011). Collisional stage in the Eastern Junggar fits interval 310–307 Ma (Zhang et al. 2018a). Consequently, the Viséan/Serpukhovian magmatism in Edren Subzone was pre-collisional in relation to

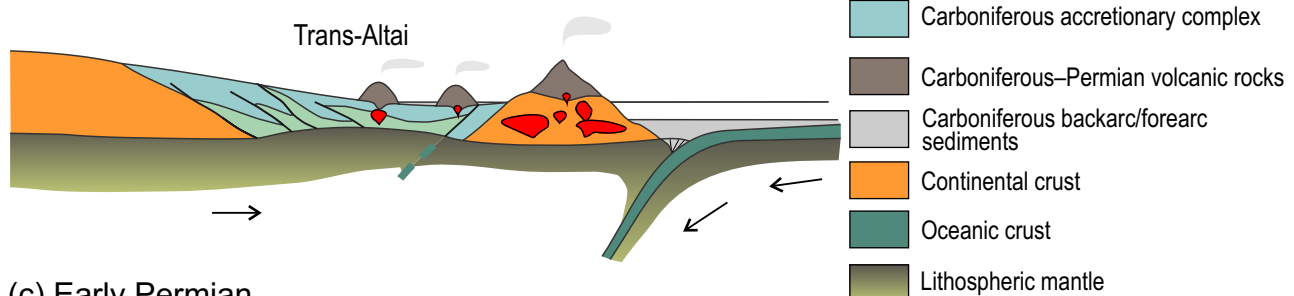these events but probably situated far from the retreating subduction zone.

Pennsylvanian ages remain undocumented from granitoid plutons of the NW and W Trans-Altai Zone. Late Carboniferous to Early Permian plutonic rocks reported from eastern parts of the Trans-Altai Zone were interpreted as reflecting a slab breakoff-related extension (Ji et al. 2020; Zhou et al. 2021) and also Guy et al. (2014a) interpreted 308–307 Ma old granitoids as post-tectonic there. Given the geological relationships, however, an occurrence of such magmatism cannot be excluded in the studied region even though the TAZ was under compression, squeezed between the consolidated Gobi Altai block in the north and Gobi Tien Shan block in the south (Fig. 17b) where massive magmatism of active continental margin culminated in the earliest Permian (Economos et al. 2012).

Cisuralian magmatic activity in TAZ was post-accretionary (Fig. 17c). According to the model of Tong et al. (2014), asthenospheric upwelling after collision and amalgamation of the Altai and Junggar blocks could have produced mantle-derived magmas that presumably evolved to the granitoids by AFC-style processes. As the Junggar and Altai terranes were amalgamated, the subducting slab breakoff could have led to partial melting of the juvenile mafic crust resulting in voluminous *c.* 320–290 Ma post-orogenic granitic plutons

(a) Early Carboniferous

Gobi Altai ←– – – – – – – future Trans-Altai Zone – – – – – – – → Gobi Tien Shan

(b) Late Carboniferous

Trans-Altai

(c) Early Permian

Gobi Altai   Trans-Altai   Gobi Tien Shan

SLAB
ROLLBACK

Silurian–Devonian accretionary complex

Carboniferous accretionary complex

Carboniferous–Permian volcanic rocks

Carboniferous backarc/forearc sediments

Continental crust

Oceanic crust

Lithospheric mantle

Plutonic rocks

Permian A-type

Late Carboniferous–Early Permian arc
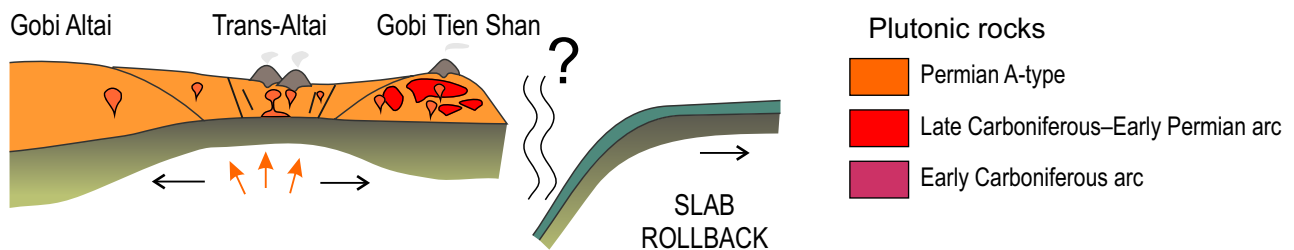
Early Carboniferous arc

Fig. 17 Schematic section between Gobi Altai and Gobi Tien Shan depicting the proposed geodynamic causes and sources of magmatism in Trans--Altai Gobi from Early Carboniferous to Early Permian times.

both in the southern realm of the Chinese Altai and in the northern parts of the Junggar Terrane (Zhang et al. 2012). The bimodal intrusive complexes and A-type granites in the southern part of the Altai orogenic belt may have formed by multiple magmatic pulses associated with a mantle plume in an anorogenic extensional setting (Tong et al. 2006; Wang et al. 2006; Zhang et al. 2010).

The Permian Aaj Bogd Pluton is situated north of the prominent Trans-Altai Shear Zone separating the Baaran and Baytag subzones of the Trans-Altai domain (Fig. 16). Analogous round Permian plutons of similar composition are exposed further SE along this shear zone (Hanžl et al. 2008; Hanžl and Krejčí eds 2008). Similarly, the Cisuralian A-type plutons were described more to the W, in spatial relationship with the Erqis (Irtysh) Fault Zone (e.g., Tong et al. 2006). Movement along the Erqis Fault Zone at 290–280 Ma was primarily sinistral and was followed by a complex succession of dextral and sinistral shearing episodes dated at 245 Ma (Laurent-Charvet et al. 2003). The spatial and temporal association of the magmatic belt of oval-shaped Permian granitic plutons with

regional-scale shear zones may indicate the emplacement of the Permian magmas into rifting-related pull-apart structures (Hutton 1988). This is consistent with the presence of E–W trending magnetic lineaments that characterise Permian rift zones in the Trans-Altai Zone (Guy et al. 2014a). These lineaments pass into zones of high deformation further west, where they are associated with exhumation of UHT rocks and emplacement of alkaline magmatic rocks and gabbros (Broussolle et al. 2019; Guy et al. 2020). Altogether, the Permian magmatic activity in Mongolia, NW China and Kazakhstan was related to post-collisional plate-scale transtensional shear zones in previously accreted CAOB crust (Seltmann et al. 2011).

5.8. A note on cyclicity of magmatism in the southern CAOB

The observed transition from Mississippian subduction-related to Early Permian post-accretionary plutonic activity in the Trans-Altai Zone follows an evolution characteristic of other accretionary orogens.

A tectonic model explaining cyclicity (S → I → A cycles, aka "trilogies") and spatial distribution of the magmatism was recently articulated by Collins et al. (2020) using the well-studied Australian granitic suites of Lachlan Orogen, SE Australia, as an example. Each of these cycles is thought to reflect an evolution from the arc (S-type) to proximal back-arc (I-type) to distal back-arc (A-type) magmatism.

In contrast to SE Australia, Carboniferous arc-related magmatism in Trans-Altai domain evolved on youthful, geochemically primitive crust, formed by freshly accreted oceanic material including metasediments of the accretionary wedge, metabasites, and island-arc related igneous rocks. In the absence of ancient (Proterozoic or older) continental basement, the Palaeozoic arc-derived sediments were psammitic and rather immature. Thus, granitoids produced by their partial melting could not have features of typical Australian restite-rich, strongly peraluminous S-type granites derived from mature metapelitic sources. In our situation, the granitoids generated from metasedimentary (technically S-type) and metaigneous (I-type) sources of the Trans-Altai Zone are inevitably rather hard to distinguish from each other (Bonin et al. 2020).

Asthenospheric upwelling related to a large-scale sinistral transfer of the whole CAOB along the Siberian margin (Şengör and Natal'in 1996) was the likely reason for Early Permian transtension and magmatic flare-up. Most probably, the rising asthenosphere both provided heat for high-T crustal melting, and directly contributed mafic (monzonitic) melts. Products of their crystallization are exemplified by mafic igneous rocks occurring in the centre of the Aaj Bogd Pluton and in many other plutons in the Eastern Junggar (e.g., Chen and Jahn 2004; Liu et al. 2013; Cui et al. 2021). These mafic parental melts further evolved by AFC-style processes with, or without, crystal accumulation, to syenitoids. The transtension connected with the activity of large-scale strike-slip shear zones not only promoted asthenospheric mantle upwelling associated with the crustal anatexis but also facilitated magma ascent and emplacement (Sylvester 1989).

6. Conclusions

Three diachronous Late Palaeozoic plutonic suites have been distinguished and characterised in the Trans-Altai Zone (Central Asian Orogenic Belt, SW Mongolia) employing petrology, U–Pb LA ICP-MS zircon dating, as well as whole-rock geochemical and Sr–Nd isotopic methods. The results and the inferred geodynamic evolution reflect the complex setting of the studied area at the boundary between Edren and Baaran subzones at the north-western tip of the Trans-Altai Zone.

1) **Tournaisian** high-K calc-alkaline, subduction-related granites are represented by (i) Bum Pluton built by amphibole–biotite monzogranite with rapakivi texture (Baaran Subzone: 352 ± 1 Ma), and (ii) elongated bodies of biotite granite in Toroin Range (southern extremity of the Edren Subzone: 347 ± 4 Ma).

2) Compositionally similar younger **Viséan/Serpukhovian** Yaryn Khad (331 ± 1 Ma) and Uliin Arag plutons intruded Devonian pillow lavas and oceanic sediments close to the northern margin of the Edren Subzone. Still these plutons are lithologically more variable (gabbro–quartz monzodiorite–granodiorite–granite).

3) All these Mississippian granitoids in both Edren and Baaran subzones share a subduction signature, with characteristic enrichment in hydrous-fluid mobile large ion lithophile elements over immobile high-field strength elements. Comparably low $^{87}Sr/^{86}Sr_i$ ratios (0.7036–0.7038), highly positive ε_{Nd}^i values (+6.6 to +6.2; +5.2 in a single sample) and low two-stage Depleted Mantle Nd model ages (0.52–0.57 (0.65) Ga) imply derivation from geochemically primitive basic–intermediate metaigneous ± immature metapsammitic (metagreywacke) sources with a short crustal residence. This is in line with the scarcity of (relatively young) zircon inheritance (Toroin Range: mainly ~ 530 Ma; Bum Pluton: ~ 404 Ma).

4) Early Permian (**Cisuralian**) Aaj Bogd Pluton and its satellite bodies intruded the Baaran Subzone (Devonian–Carboniferous turbidites and Mississippian volcanic-arc sequence of dominantly andesite composition). The round Aaj Bogd Pluton is characterised by 'onion skin' concentric structure, with Ol-, Cpx-, Opx-bearing monzogabbro/quartz monzodiorite bodies (284 ± 1 and 294 ± 3 Ma) in the centre, surrounded by the dominant biotite–amphibole syenite (282 ± 1 Ma) to leucogranite mass.

5) Whole-rock composition of the Aaj Bogd Pluton points to the intra-plate geotectonic setting and the rocks are interpreted as having crystallised from asthenosphere-derived parental melts that evolved by AFC-style processes. Alkali feldspar granites to quartz syenites from the satellite bodies (290 ± 1 Ma) show a feeble A_2-type affinity and likely originated from youthful (?Devonian, as some magmatic zircons contain ~ 355 Ma cores) arc-related intermediate metaigneous rocks (tonalites–granodiorites), from which they have inherited a spurious, arc-like Nb–Ta depletion.

6) In the broader context, the both pulses (Tournaisian and Visean) of Mississippian granitoids are viewed as a product of magmatism at the Gobi Altai Plate active margin that evolved above a southward retreating subduction zone. The Cisuralian, clearly post-orogenic alkaline granites of the Aaj Bogd Pluton and its satellite bodies belong to a girdle of analogous round, post-

-tectonic (A$_2$-type-like) intrusions that could be traced for more than one and a half thousand kilometres from the Dulate Arc in the Eastern Junggar to Khan Bogd Pluton in the Central Gobi. The Early Permian plutons intruded due to asthenosphere upwelling and orogenic collapse of pre-Permian magmatic-arc systems of the Trans-Altai Zone amalgamated between Gobi Altai and Gobi Tien Shan crustal blocks. Transtension was accompanied by the development of large-scale strike-slip shear zones likely controlling the final granite emplacement.

Electronic supplementary material. Selected electron-microprobe analyses of the main and accessory rock-forming minerals, laser-ablation ICP-MS U–Pb data from dated zircons, whole-rock major- and trace-element and Sr–Nd isotopic geochemical analyses are available at the Journal web site (*http://dx.doi.org/10.3190/jgeosci.366*).

References

Amantov VA, Blagonravov VA, Borzakovskiy YA, Durante M V, Zonenshain LP, Luvsandanzan B, Matrosov PS, Suyetenko OD, Filippova IB, Hasin RA (1970) Main features of Paleozoic stratigraphy of Mongolian People's Republic. In: Zaitsev N, Luvsandanzan B, Marinov NA (eds) Stratigraphy and Tectonics of the Mongolian People's Republic. Nauka Press, Moscow, pp 8–63 (in Russian)

Amar-Amgalan S (2004) Petrographical and Geochemical Studies on the Khanbogd Alkaline Complex in South Mongolia. Unpublished MSci. thesis, Shimane University, Matsue, pp 1–99

Amar-Amgalan S (2008) U–Pb Geochronology and Multi-isotopic Systematics of Granitoids from Mongolia, Central Asian Orogenic Belt: Implications for Granitoid Origin and Crustal Growth during the Phanerozoic. Unpublished PhD. thesis, Okayama University, pp 1–146

Antipin V, Gerel O, Perepelov A, Odgerel D, Zolboo T (2016) Late Paleozoic and Early Mesozoic rare-metal granites in Central Mongolia and Baikal region: review of geochemistry, possible magma sources and related mineralization. J Geosci 61: 105–125

Badarch G, Dickson Cunningham W, Windley BF (2002) A new terrane subdivision for Mongolia: implications for the Phanerozoic crustal growth of Central Asia. J Asian Earth Sci 21: 87–104

Bibikova VE, Kirnozova TI, Kozakov IK, Kotov AB, Neymark LA, Gorokhovskiy BM, Shuleshko IK (1992) U–Pb ages for polymetamorphic complexes on the southern flank of the Mongolian and Gobi Altai. Geotectonics 26: 166–172

Boehnke P, Watson EB, Trail D, Harrison TM, Schmitt AK (2013) Zircon saturation re-visited. Chem Geol 351: 324–334

Boldbaatar E, Nanzad B, Sereenen J, Locmelis M, Osanai Y, Batsaikhan N, Dashtseren K, Zorigtbaatar A (2019) Geochronology and geochemistry of the intrusive suite associated with the Khatsavch porphyry Cu–Au (Mo) deposit, South Mongolia. Ore Geol Rev 111: 102978

Bonin B, Janoušek V, Moyen JF (2020) Chemical variation, modal composition and classification of granitoids. In: Janoušek V, Bonin B, Collins WJ, Farina F, Bowden P (eds) Post-Archean Granitic Rocks: Contrasting Petrogenetic Processes and Tectonic Environments. Geological Society of London Special Publications 491, pp 9–51

Boynton WV (1984) Cosmochemistry of the rare earth elements: meteorite studies. In: Henderson P (eds) Rare Earth Element Geochemistry. Elsevier, Amsterdam, pp 63–114

Broussolle A, Sun M, Schulmann K, Guy A, Aguilar C, Štípská P, Jiang YD, Yu Y, Xiao WJ (2019) Are the Chinese Altai "terranes" the result of juxtaposition of different crustal levels during Late Devonian and Permian orogenesis? Gondwana Res 66:183–206

Burenjargal U, Okamoto A, Kuwatani T, Sakata S, Hirata T, Tsuchiya N (2014) Thermal evolution of the Tseel Terrane, SW Mongolia and its relation to granitoid intrusions in the Central Asian Orogenic Belt. J Metamorph Geol 32: 765–790

Burenjargal U, Okamoto A, Tsuchiya N, Uno M, Horie K, Hokada T (2016) Contrasting geochemical signatures of Devonian and Permian granitoids from the Tseel Terrane, SW Mongolia. J Geosci 61: 51–66

Buriánek D, Hanžl P, Budil P, Gerdes A (2012) Evolution of the early Permian volcanic–plutonic complex in the western part of the Permian Gobi-Altay rift (Khar Argalant Mts., SW Mongolia). J Geosci 57: 105–126

Buriánek D, Janoušek V, Hanžl P, Jiang YD, Schulmann K, Lexa O, Altanbaatar B (2016) Petrogenesis of the

Late Carboniferous Sagsai Pluton in the SE Mongolian Altai. J Geosci 61: 67–92

Buriánek D, Schulmann K, Hrdličková K, Hanžl P, Janoušek V, Gerdes A, Lexa O (2017) Geochemical and geochronological constraints on distinct Early–Neoproterozoic and Cambrian accretionary events along southern margin of the Baydrag Continent in western Mongolia. Gondwana Res 47: 200–227

Buriánek D, Soejono I, Schulmann K, Janoušek V, Hanžl P, Čáp P, Bold U, Svojtka M, Collett S, Žáček V (2022) Subduction-controlled temporal and spatial variations in early Palaeozoic sedimentary and volcanic record of the Mongol-Altai Domain. J Asian Earth Sci 230: 105182, DOI 10.1016/j.jseaes.2022.105182

Buslov MM (2011) Tectonics and geodynamics of the Central Asian Foldbelt: the role of Late Paleozoic large-amplitude strike-slip faults. Russ Geol Geophys 52: 52–71

Cai K, Sun M, Xiao WJ, Yuan C, Zhao GC, Long XP, Tumurkhuu D, Zhou K (2014) Petrogenesis of late Paleozoic tholeiitic, Nb-enriched, calc-alkaline and adakitic rocks in southwestern Mongolia: implications for intra-oceanic arc evolution. Lithos 202–203: 413–428

Cai K, Sun M, Jahn BM, Xiao WJ, Yuan C, Long XP, Chen HY, Tumurkhuu D (2015) A synthesis of zircon U–Pb ages and Hf isotopic compositions of granitoids from southwest Mongolia: implications for crustal nature and tectonic evolution of the Altai Superterrane. Lithos 232: 131–142

Chen B, Jahn BM (2004) Genesis of post-collisional granitoids and basement nature of the Junggar Terrane, NW China: Nd–Sr isotope and trace element evidence. J Asian Earth Sci 23: 691–703

Chernov EE, Kovalenko DV (2008) New paleomagnetic data on Carboniferous–Permian geological complexes of Mongolia. Dokl Earth Sci 420: 586–602

Clemens JD, Holloway JR, White AJR (1986) Origin of an A-type granite: experimental constraints. Amer Miner 71: 317–324

Collins WJ, Beams SD, White AJR, Chappell BW (1982) Nature and origin of A-type granites with particular reference to southeastern Australia. Contrib Mineral Petrol 80: 189–200

Collins WJ, Huang HQ, Bowden P, Kemp AIS (2020) Repeated S–I–A-type granite trilogy in the Lachlan Orogen and geochemical contrasts with A-type granites in Nigeria: implications for petrogenesis and tectonic discrimination. In: Janoušek V, Bonin B, Collins WJ, Farina F, Bowden P (eds) Post-Archean Granitic Rocks: Contrasting Petrogenetic Processes and Tectonic Environments. Geological Society of London Special Publications 491, pp 53–76

Cornejo PC, Mahood GA (1997) Seeing past the effects of re-equilibration to reconstruct magmatic gradients in plutons: La Gloria Pluton, central Chilean Andes. Contrib Mineral Petrol 127: 159–175

Cox KG, Bell JD, Pankhurst RJ (1979) The Interpretation of Igneous Rocks. George Allen & Unwin, London, pp 1–450

Creaser RA, Price RC, Wormald RJ (1991) A-type granites revised: assessment of a residual-source model. Geology 19: 163–166

Cui X, Sun M, Zhao G, Zhang Y (2021) Origin of Permian mafic intrusions in southern Chinese Altai, Central Asian Orogenic Belt: a post-collisional extension system triggered by slab break-off. Lithos 390–391: 106112

Cunningham D (2005) Active intracontinental transpressional mountain building in the Mongolian Altai: defining a new class of orogen. Earth Planet Sci Lett 240: 436–444

Debon F, Le Fort P (1983) A chemical–mineralogical classification of common plutonic rocks and associations. Trans Roy Soc Edinb, Earth Sci 73: 135–149

Debon F, Le Fort P (1988) A cationic classification of common plutonic rocks and their magmatic associations: principles, method, applications. Bull Minéral 111: 493–510

Demoux A, Kröner A, Liu D, Badarch G (2009) Precambrian crystalline basement in southern Mongolia as revealed by SHRIMP zircon dating. Int J Earth Sci 98: 1365–1380

Didier J, Barbarin B (1991) The different types of enclaves in granites – nomenclature. In: Didier J, Barbarin B (eds) Enclaves and Granite Petrology. Elsevier, Amsterdam, pp 19–24

Dietl C, Koyi HA (2002) Emplacement of nested diapirs: results of centrifuge modelling. J Virtual Explor 7: 79–86

Drake MJ (1975) The oxidation state of europium as an indicator of oxygen fugacity. Geochim Cosmochim Acta 39: 55–64

Droop GTR (1987) A general equation for estimating Fe^{3+} concentrations in ferromagnesian silicates and oxides from microprobe analyses, using stoichiometric criteria. Mineral Mag 51: 431–435

Eby GN (1990) The A-type granitoids: a review of their occurrence and chemical characteristics and speculations on their petrogenesis. Lithos 26: 115–134

Economos RC, Hanžl P, Hrdličková K, Buriánek D, Said LO, Gerdes A, Paterson SR (2008) Geochemical and structural constraints on the magmatic history of the Chandman Massif of the eastern Mongolian Altay Range, SW Mongolia. J Geosci 53: 335–352

Economos RC, Paterson SR, Said LO, Ducea MN, Anderson JL, Padilla AJ (2012) Gobi–Tianshan connections: field observations and isotopes from an early Permian arc complex in southern Mongolia. Bull Geol Soc Amer 124: 1688–1701

Edel JB, Schulmann K, Hanžl P, Lexa O (2014) Palaeomagnetic and structural constraints on 90°

anticlockwise rotation in SW Mongolia during the Permo–Triassic: implications for Altaid oroclinal bending. Preliminary palaeomagnetic results. J Asian Earth Sci 94:157–171

Edel JB, Schulmann K, Lexa O, Lardeaux JM (2018) Late Palaeozoic palaeomagnetic and tectonic constraints for amalgamation of Pangea supercontinent in the European Variscan belt. Earth Sci Rev 177: 589–612

Faure G (1986) Principles of Isotope Geology, 2nd ed. John Wiley & Sons, New York, pp 1–589

Filippova I V, Suetenko OD, Levintov ME (1990) Geological map of Western Mongolia at a scale 1 : 500,000. AN SSSR, Moscow (in Russian)

Frost BR, Barnes CG, Collins WJ, Arculus RJ, Ellis DJ, Frost CD (2001) A geochemical classification for granitic rocks. J Petrol 42: 2033–2048

Galbraith RF (2005) Statistics for Fission Track Analysis. Chapman and Hall/CRC Press, New York, pp 1–240

Gerel O, Oyungerel S, Minjin Ch (2005) Intrusive magmatism of South Mongolia. In: Seltmann R, Gerel O, Kirwin D (eds) Geodynamics and Metallogeny of Mongolia with a Special Emphasis on Copper and Gold Deposits. CERCAMS, London, pp 131–149

Gerdes A, Wörner G, Henk A (2000) Post-collisional granite generation and HT–LP metamorphism by radiogenic heating: the Variscan South Bohemian Batholith. J Geol Soc, London 157: 577–587

Gibsher AS, Khain E V, Kotov AB, Sal'nikova EB, Kozakov IK, Kovach VP, Yakovleva SZ, Fedoseenko AM (2001) Late Vendian age of the Khan-Taishiri ophiolite complex in western Mongolia. Russ Geol Geophys 42: 1179–1185 (in Russian with English abstract)

Goldstein SL, O'Nions RK, Hamilton PJ (1984) A Sm–Nd isotopic study of atmospheric dusts and particulates from major river systems. Earth Planet Sci Lett 70: 221–236

Guy A, Schulmann K, Munschy M, Miehe JM, Edel JB, Lexa O, Fairhead D (2014a) Geophysical constraints for terrane boundaries in southern Mongolia. J Geophys Res B: Solid Earth 119: 7966–7991

Guy A, Schulmann K, Clauer N, Hasalová P, Seltmann R, Armstrong R, Lexa O, Benedicto A (2014b) Late Paleozoic–Mesozoic tectonic evolution of the Trans-Altai and South Gobi zones in southern Mongolia based on structural and geochronological data. Gondwana Res 25: 309–337

Guy A, Schulmann K, Janoušek V, Štípská P, Armstrong R, Belousova E, Dolgopolova A, Seltmann R, Lexa O, Jiang YD, Hanžl P (2015) Geophysical and geochemical nature of relaminated arc-derived lower crust underneath oceanic domain in southern Mongolia. Tectonics 34: 1030–1053

Guy A, Schulmann K, Soejono I, Xiao WJ (2020) Revision of the Chinese Altai–East Junggar Terrane

accretion model based on geophysical and geological constraints. Tectonics 39, e2019TC006026. DOI 10.1029/2019TC006026

Guy A, Schulmann K, Soejono I, Holzrichter N, Lexa O, Munschy M (2021) Structures and geodynamics of the Mongolian tract of the Central Asian Orogenic Belt constrained by potential field analyses. Gondwana Res 92: 26–53

Hanžl P, Krejčí Z, eds (2008) Geological map of the Trans-Altay Gobi 1 : 500 000. Czech Geological Survey, Prague

Hanžl P, Bat-Ulzii D, Rejchrt M, Košler J, Bolormaa K, Hrdličková K (2008) Geology and geochemistry of the Palaeozoic plutonic bodies of the Trans-Altay Gobi, SW Mongolia: implications for magmatic processes in an accreted volcanic-arc system. J Geosci 53: 201–234

Hanžl P, Schulmann K, Janoušek V, Lexa O, Hrdličková K, Jiang YD, Buriánek D, Altanbaatar B, Ganchuluun T, Erban V (2016) Making continental crust: origin of Devonian orthogneisses from SE Mongolian Altai. J Geosci 61: 25–50

Hanžl P, Krejčí Z, Altanbaatar B, Lexa O, Buriánek D, Janoušek V, Schulmann K, Jiang YD, Hrdličková K (2017) Geology of the Gobi Altai and Tseel terranes in the central part of the Sagsai River watershed, SE Mongolian Altai. J Maps 13: 270–275

Hanžl P, Guy A, Battushig A, Lexa O, Schulmann K, Kunceová E, Hrdličková K, Janoušek V, Buriánek D, Krejčí Z, Jiang YD, Otgonbaatar D (2020) Geology of the Gobi and Mongol Altai junction enhanced by gravity analysis: a key for understanding of the Mongolian Altaides. J Maps 16: 98–107

Hawthorne FC, Oberti R, Harlow GE, Maresch WV, Martin RF, Schumacher JC, Welch MD (2012) Nomenclature of the amphibole supergroup. Amer Miner 97: 2031–2048

Helo C, Hegner E, Kröner A, Badarch G, Tomurtogoo O, Windley BF, Dulski P (2006) Chemical signature of Paleozoic accretionary complexes of Central Asian Orogenic Belt in south Mongolia: constraints on arc environments and crustal growth. Chem Geol 227: 236–257

Heumann MJ, Johnson CL, Webb LE, Taylor JP, Jalbaa U, Minjin C (2012) Paleogeographic reconstruction of a late Paleozoic arc collision zone, southern Mongolia. Geol Soc Am Bull 124: 1514–1534

Holland TJB, Blundy J (1994) Non-ideal interactions in calcite amphiboles and their bearing on amphibole–plagioclase thermometry. Contrib Mineral Petrol 116: 433–447

Hollocher K, Robinson P, Walsh E, Roberts D (2012) Geochemistry of amphibolite-facies volcanics and gabbros of the Støren Nappe in extensions west and southwest of Trondheim, Western Gneiss Region, Norway: a key to correlations and paleotectonic settings. Amer J Sci 312: 357–416

Hong T, Gao J, Xu XW, Wu C, Li H (2021) Late Palaeozoic magmatism in the eastern Tseel Terrane of SW Mongolia evidenced by chronological and geochemical data. Geol J 56: 3415–3447

Horstwood MSA, Košler J, Gehrels G, Jackson SE, McLean NM, Paton C, Pearson NJ, Sircombe K, Sylvester P, Vermeesch P, Bowring JF, Condon DJ, Schoene B (2016) Community-derived standards for LA-ICP-MS U–(Th–)Pb geochronology – uncertainty propagation, age interpretation and data reporting. Geostand Geoanal Res 40: 311–331

Hoskin PWO, Schaltegger U (2003) The composition of zircon and igneous and metamorphic petrogenesis. In: Hanchar JM, Hoskin PWO (eds) Zircon. Mineralogical Society of America and Geochemical Society Reviews in Mineralogy and Geochemistry 53: 27–62

Hoskin PWO, Kinny PD, Wyborn D, Chappell BW (2000) Identifying accessory mineral saturation during differentiation in granitoid magmas: an integral approach. J Petrol 41: 1365–1396

Hrdličková K, Bolormaa K, Buriánek D, Hanžl P, Gerdes A, Janoušek V (2008) Petrology and age of metamorphosed rocks in tectonic slices inside the Palaeozoic sediments of the eastern Mongolian Altay, SW Mongolia. J Geosci 53: 139–165

Hrdličková K, Gerdes A, Gilíková H, Bat-Ulzii D, Hanžl P (2010) Burd Gol granite massif as a product of the late Cambrian post-orogenic magmatism in the SE part of the Lake Zone, Gobi Altay, SW Mongolia. J Geosci 55: 369–386

Hutton DHW (1988) Granite emplacement mechanisms and tectonic controls: inferences from deformation studies. Trans Roy Soc Edinb, Earth Sci 79: 245–255

Irvine TN, Baragar WRA (1971) A guide to the chemical classification of the common volcanic rocks. Canad J Earth Sci 8: 523–54

Izokh AE, Vishnevskii AV, Polyakov GV, Shelepaev RA (2011) Age of picrite and picrodolerite magmatism in western Mongolia. Russ Geol Geophys 52: 7–23

Jackson SE, Pearson NJ, Griffin WL, Belousova EA (2004) The application of laser ablation-inductively coupled plasma-mass spectrometry to in situ U–Pb zircon geochronology. Chem Geol 211: 47–69

Jacobsen SB, Wasserburg GJ (1980) Sm–Nd isotopic evolution of chondrites. Earth Planet Sci Lett 50: 139–155

Jahn BM (2004) The Central Asian Orogenic Belt and growth of the continental crust in the Phanerozoic. In: Malpas J, Fletcher A, Ali JR, Aitchison JC (eds) Aspects of the Tectonic Evolution of China. Geological Society London Special Publications 226, pp 73–100

Jahn BM, Wu F, Chen B (2000) Massive granitoid generation in Central Asia: Nd isotope evidence and implication for continental growth in the Phanerozoic. Episodes 23: 82–92

Janoušek V (2006) Saturnin, R language script for application of accessory-mineral saturation models in igneous geochemistry. Geol Carpath 57: 131–142

Janoušek V, Farrow CM, Erban V (2006) Interpretation of whole-rock geochemical data in igneous geochemistry: introducing Geochemical Data Toolkit (GCDkit). J Petrol 47: 1255–1259

Janoušek V, Moyen JF, Martin H, Erban V, Farrow C (2016) Geochemical Modelling of Igneous Processes – Principles and Recipes in R Language. Bringing the Power of R to a Geochemical Community. Springer, Berlin, pp 1–346

Janoušek V, Jiang YD, Buriánek D, Schulmann K, Hanžl P, Soejono I, Kröner A, Altanbaatar B, Erban V, Lexa O, Ganchuluun T, Košler J (2018) Cambrian–Ordovician magmatism of the Ikh-Mongol Arc System exemplified by the Khantaishir Magmatic Complex (Lake Zone, south–central Mongolia). Gondwana Res 54: 122–149

Ji Z, Zhang Z, Han B, Tserendash N (2020) Multiphase Late Devonian to Carboniferous volcanic events in the west of Oyu Tolgoi, southeastern Mongolia: new geochronological, geochemical, and isotopic constraints on tectonic history. Gondwana Res 88: 169–184

Jian P, Kröner A, Jahn BM, Windley BF, Shi Y, Zhang W, Zhang F, Miao L, Tomurhuu D, Liu D (2014) Zircon dating of Neoproterozoic and Cambrian ophiolites in West Mongolia and implications for the timing of orogenic processes in the central part of the Central Asian Orogenic Belt. Earth Sci Rev 133: 62–93

Jiang YD, Sun M, Kröner A, Tumurkhuu D, Long XP, Zhao GC, Yuan C, Xiao WJ (2012) The high-grade Tseel Terrane in SW Mongolia: an Early Paleozoic arc system or a Precambrian sliver? Lithos 142–143: 95–115

Jiang YD, Schulmann K, Kröner A, Sun M, Lexa O, Janoušek V, Buriánek D, Yuan C, Hanžl P (2017) Neoproterozoic–Early Paleozoic peri-Pacific accretionary evolution of the Mongolian collage system: insights from geochemical and U–Pb zircon data from the Ordovician sedimentary wedge in the Mongolian Altai. Tectonics 36: 2305–2331

Khukhuudei U, Kusky T, Otgonbayar O, Wang L (2020) The Early Palaeozoic mega-thrusting of the Gondwana-derived Altay–Lake Zone in western Mongolia: implications for the development of the Central Asian Orogenic Belt and Paleo-Asian Ocean evolution. Geol J 55: 2129–2149

Kovalenko DV, Chernov EE (2008) Paleomagnetism of Carboniferous–Permian and early Jurassic geological complexes in Mongolia. Izv Phys Solid Earth 44: 427–441

Kovalenko VI, Yarmolyuk VV, Saľnikova EB, Kozlovsky AM, Kotov AB, Kovach VP, Savatenkov VM, Vladykin NV, Ponomarchuk VA (2006) Geology,

geochronology, and geodynamics of the Khan Bogd alkali granite pluton in southern Mongolia. Geotectonics 40: 450–466

Kozakov IK, Glebovitsky VA, Bibikova EV, Azimov PY, Kirnozova TI (2002) Hercynian granulites of Mongolian and Gobian Altai: geodynamic setting and formation conditions. Dokl Earth Sci 386: 781–785

Kozakov IK, Kovach VP, Bibikova EV, Kirnozova TI, Zagornaya NY, Plotkina YV, Podkovyrov VN (2007) Age and sources of granitoids in the junction zone of the Caledonides and Hercynides in southwestern Mongolia: geodynamic implications. Petrology 15: 126–150

Kozakov IK, Saľnikova EB, Yarmolyuk VV, Kozlovsky AM, Kovach VP, Azimov PY, Anisimova IV, Lebedev VI, Enjin G, Erdenejargal C, Plotkina YV, Fedoseenko AM, Yakovleva SZ (2011) Convergent boundaries and related igneous and metamorphic complexes in Caledonides of Central Asia. Geotectonics 46: 16–36

Kozlovsky AM, Yarmolyuk VV, Saľnikova EB, Savatenkov VM, Kovalenko VI (2005) Age of bimodal and alkali granite magmatism of the Gobi-Tien Shan rift zone, Tost Range, southern Mongolia. Petrology 13: 197–203

Kozlovsky AM, Yarmolyuk VV, Savatenkov VM, Kovach VP (2006) Sources of basaltoid magmas in rift settings of an active continental margin: example from the bimodal association of the Noen and Tost ranges of the Late Paleozoic Gobi-Tien Shan rift zone, southern Mongolia. Petrology 14: 337–360

Kozlovsky AM, Yarmolyuk VV, Kovalenko VI, Savatenkov VM, Velivetskaya TA (2007) Trachytes, comendites, and pantellerites of the Late Paleozoic bimodal rift association of the Noen and Tost ranges, southern Mongolia: differentiation and contamination of peralkaline salic melts. Petrology 15: 240–263

Kozlovsky AM, Yarmolyuk VV, Travin AV, Saľnikova EB, Anisimova IV, Plotkina YV, Savatenkov VM, Fedoseenko AM, Yakovlevac SZ (2012) Stages and regularities in the development of Late Paleozoic anorogenic volcanism in the southern Mongolia Hercynides. Dokl Earth Sci 445: 811–817

Kozlovsky AM, Yarmolyuk VV, Saľnikova EB, Travin AV, Kotov AB, Plotkina JV, Kudryashova EA, Savatenkov VM (2015) Late Paleozoic anorogenic magmatism of the Gobi Altai (SW Mongolia): tectonic position, geochronology and correlation with igneous activity of the Central Asian Orogenic Belt. J Asian Earth Sci 113: 524–541

Kröner A, Lehmann J, Schulmann K, Demoux A, Lexa O, Tomurhuu D, Štípská P, Liu D, Wingate MTD (2010) Lithostratigraphic and geochronological constraints on the evolution of the Central Asian Orogenic Belt in SW Mongolia: Early Paleozoic rifting followed by Late Paleozoic accretion. Amer J Sci 310: 523–574

Kröner A, Kovach V, Alexeiev D, Wang KL, Wong J, Degtyarev K, Kozakov I (2017) No excessive crustal growth in the Central Asian Orogenic Belt: further evidence from field relationships and isotopic data. Gondwana Res 50: 135–166

Laeger K, Halama R, Hansteen T, Savov IP, Murcia HF, Cortés GP, Garbe-Schönberg D (2013) Crystallization conditions and petrogenesis of the lava dome from the ~900 years BP eruption of Cerro Machín Volcano, Colombia. J South Am Earth Sci 48: 193–208

Lamb MA, Badarch G (1997) Paleozoic sedimentary basins and volcanic-arc systems of southern Mongolia: new stratigraphic and sedimentologic constraints. Int Geol Rev 39: 542–576

Lamb MA, Badarch G (2001) Paleozoic sedimentary basins and volcanic arc systems of southern Mongolia: new geochemical and petrographic constraints. In: Hendrix SM, Davis AG (eds) Paleozoic and Mesozoic Tectonic Evolution of Central and Eastern Asia: From Continental Assembly to Intracontinental Deformation. Geological Society of America Memoirs 194, pp 117–149

Lamb MA, Badarch G, Navratil T, Poier R (2008) Structural and geochronologic data from the Shin Jinst area, eastern Gobi Altai, Mongolia: implications for Phanerozoic intracontinental deformation in Asia. Tectonophysics 451: 312–330

Laurent O, Martin H, Moyen JF, Doucelance R (2014) The diversity and evolution of late-Archean granitoids: evidence for the onset of 'modern-style' plate tectonics between 3.0 and 2.5 Ga. Lithos 205: 208–235

Laurent-Charvet S, Charvet J, Monié P, Shu L (2003) Late Paleozoic strike-slip shear zones in eastern central Asia (NW China): new structural and geochronological data. Tectonics 22: 1009. DOI 10.1029/2001TC901047

Lehmann J, Schulmann K, Lexa O, Corsini M, Kröner A, Štípská P, Tomurhuu D, Otgonbator D (2010) Structural constraints on the evolution of the Central Asian Orogenic Belt in SW Mongolia. Amer J Sci 310: 575–628

Lehmann J, Schulmann K, Lexa O, Závada P, Štípská P, Hasalová P, Belyanin G, Corsini M (2017) Detachment folding of partially molten crust in accretionary orogens: a new magma-enhanced vertical mass and heat transfer mechanism. Lithosphere 9: 889–909

Li W, Liu YQ, Dong YP, Zhou XH, Liu XM, Li H, Fan TT, Zhou DW, Xu XY, Chen JL (2012) The geochemical characteristics, geochronology and tectonic significance of the Carboniferous volcanic rocks of the Santanghu area in northeastern Xinjiang, China. Sci China Earth Sci 568 56: 1318–1333

Liew TC, Hofmann AW (1988) Precambrian crustal components, plutonic associations, plate environment of the Hercynian Fold Belt of Central Europe: indications from a Nd and Sr isotopic study. Contrib Mineral Petrol 98: 129–138

Liu H, Leng W (2020) Tarim Large Igneous Province caused by a wide and wet mantle plume. J Geophys Res, Solid Earth 125, e2019JB019001, DOI 10.1029/2019JB019001

Liu W, Liu XJ, Liu LJ (2013) Underplating generated A- and I-type granitoids of the East Junggar from the lower and the upper oceanic crust with mixing of mafic magma: insights from integrated zircon U–Pb ages, petrography, geochemistry and Nd–Sr–Hf isotopes. Lithos 179: 293–319

Liu B, Chen JF, Ma X, Liu JL, Gong EP, Shi WG, Han BF (2017) Timing of the final closure of the Irtysh–Zaysan Ocean: new insights from the earliest stitching pluton in the northern West Junggar, NW China. Geol J 53: 2810–2823

Long XP, Yuan C, Sun M, Safonova I, Xiao WJ, Wang Y (2012) Geochemistry and U–Pb detrital zircon dating of Paleozoic graywackes in East Junggar, NW China: insights into subduction–accretion processes in the southern Central Asian Orogenic Belt. Gondwana Res 21: 637–653

Ludwig KR (1998) On the treatment of concordant uranium–lead ages. Geochim Cosmochim Acta 62: 665–676

Ludwig KR, Titterington D (1994) Calculation of ^{230}Th/U isochrons, ages, and errors. Geochim Cosmochim Acta 58: 5031–5042

Lugmair GW, Marti K (1978) Lunar initial ^{143}Nd/^{144}Nd: differential evolution line of the lunar crust and mantle. Earth Planet Sci Lett 39: 349–357

Mao Q, Xiao WJ, Fang T, Windley BF, Sun M, Ao SJ, Zhang J, Huang XK (2014) Geochronology, geochemistry and petrogenesis of Early Permian alkaline magmatism in the Eastern Tianshan: implications for tectonics of the southern Altaids. Lithos 190–191: 37–51

Marinov NA, Zonenshain LP, Blagonravov VA (eds) (1973) Geology of the Mongolian People's Republic, vol. 2. Magmatism, Metamorphism, Tectonics. Nedra, Moscow, pp 1–782 (in Russian)

Marxer F, Ulmer P (2019) Crystallisation and zircon saturation of calc-alkaline tonalite from the Adamello Batholith at upper crustal conditions: an experimental study. Contrib Mineral Petrol 174: 84

Merlet C (1994) An accurate computer correction program for quantitative electron probe microanalysis. Microchim Acta 114–115: 363–376

Míková J, Denková P (2007) Modified chromatographic separation scheme for Sr and Nd isotope analysis in geological silicate samples. J Geosci 52: 221–226

Miller RB, Paterson SR (1999) In defense of magmatic diapirs. J Struct Geol 21: 1161–1173

Molyneux SJ, Hutton DHW (2000) Evidence for significant granite space creation by the ballooning mechanism: the example of the Ardara Pluton, Ireland. Geol Soc Am Bull 112: 1543–1558

Mossakovsky AA, Ruzhentsev S V, Samygin SG, Kheraskova TN (1993) The Central Asian fold-belt: geodynamic evolution and the history of formation. Geotectonics 6: 3–31 (in Russian)

Nguyen H, Hanžl P, Janoušek V, Schulmann K, Ulrich M, Jiang YD, Lexa O, Altanbaatar B, Deiller P (2018) Geochemistry and geochronology of Mississippian volcanic rocks from SW Mongolia: implications for terrane subdivision and magmatic arc activity in the Trans-Altai Zone. J Asian Earth Sci 164: 322–343

Paterson SR, Fowler TK, Miller RB (1996) Pluton emplacement in arcs: a crustal-scale exchange process. Trans Roy Soc Edinb, Earth Sci 87: 115–123

Paterson SR, Memeti V, Anderson JL, Cao W, Lackey JS, Putirka KD, Miller RB, Miller JS, Mundil R (2014) Overview of arc processes and tempos. In: Memeti V, Paterson SR, Putirka KD (eds) Formation of the Sierra Nevada Batholith: Magmatic and Tectonic Processes and Their Tempos. Geological Society of America Field Guide 34, pp 87–116

Patiño Douce AE (1997) Generation of metaluminous A-type granites by low-pressure melting of calc-alkaline granitoids. Geology 25: 743–746

Paton C, Hellstrom J, Paul B, Woodhead J, Hergt J (2011) Iolite: freeware for the visualisation and processing of mass spectrometric data. J Anal At Spectrom 26: 2508–2518

Pearce JA (1996) Sources and settings of granitic rocks. Episodes 19: 120–125

Pearce JA, Peate DW (1995) Tectonic implications of the composition of volcanic arc magmas. Ann Rev Earth Planet Sci 23: 251–285

Pearce JA, Harris NBW, Tindle AG (1984) Trace element discrimination diagrams for the tectonic interpretation of granitic rocks. J Petrol 25: 956–983

Pearce JA, Stern RJ, Bloomer SH, Fryer P (2005) Geochemical mapping of the Mariana arc-basin system: implications for the nature and distribution of subduction components. Geochem Geophys Geosyst 6: Q07006

Pearce JA, Ernst RE, Peate DW, Rogers C (2021) LIP printing: use of immobile element proxies to characterize Large Igneous Provinces in the geologic record. Lithos 392–393: 106068

Peccerillo A, Taylor SR (1976) Geochemistry of Eocene calc-alkaline volcanic rocks from the Kastamonu area, Northern Turkey. Contrib Mineral Petrol 58: 63–81

Pin C, Zalduegui JFS (1997) Sequential separation of light rare-earth elements, thorium and uranium by miniaturized extraction chromatography: application to isotopic analyses of silicate rocks. Anal Chim Acta 339: 79–89

Pin C, Briot D, Bassin C, Poitrasson F (1994) Concomitant separation of strontium and samarium–neodymium for isotopic analysis in silicate samples, based on specific extraction chromatography. Anal Chim Acta 298: 209–217

PLANK T (2014) The chemical composition of subducting sediments. In: HOLLAND HD, TUREKIAN KK (eds) Treatise on Geochemistry (2nd edition). Elsevier-Pergamon, Oxford, pp 607–629

POWELL R, HOLLAND TJB (1990) Calculated mineral equilibria in the pelite system KFMASH (K_2O–FeO–MgO–Al_2O_3–SiO_2–H_2O). Amer Miner 75: 367–380

REHKÄMPER M, HOFMANN AW (1997) Recycled ocean crust and sediment in Indian Ocean MORB. Earth Planet Sci Lett 147: 93–106

RIDOLFI F, RENZULLI A, PUERINI M (2010) Stability and chemical equilibrium of amphibole in calc-alkaline magmas: an overview, new thermobarometric formulations and application to subduction-related volcanoes. Contrib Mineral Petrol 160: 45–66

RIPPINGTON S, CUNNINGHAM D, ENGLAND R, HENDRIKS B (2013) The crustal assembly of southern Mongolia: new structural, lithological and geochronological data from the Nemegt and Altan ranges. Gondwana Res 23: 1535–1553

RUDNEV SN, IZOKH AE, KOVACH VP, SHELEPAEV RA, TERENT'EVA LB (2009) Age, composition, sources, and geodynamic environments of the origin of granitoids in the northern part of the Ozernaya Zone, western Mongolia: growth mechanisms of the Paleozoic continental crust. Petrology 17: 439–475

RUDNEV SN, MAL'KOVETS VG, BELOUSOVA EA, TRET'YAKOVA IG, GIBSHER AA (2019) Composition and age of plagiogranitoids in the south of the Lake Zone (western Mongolia). Russ Geol Geophys 60: 1205–1228

RUDNEV SN, GIBSHER AS, SEMENOVA DV (2021) Vendian island-arc intrusive magmatism of the Lake Zone of Western Mongolia (geological, geochronological, and petrochemical data). Russ Geol Geophys 62: 619–632

RUZHENTSEV SV (1985) Geology of the Gobi Tien Shan and problems of South-Mongolian Ocean. Izv Vys Ucheb Zaved, Geol i Razv 6: 12–19 (in Russian)

RUZHENTSEV SV, MOSSAKOVSKY AA (1995) Geodynamic and tectonic evolution of the Central Asian Paleozoic structures as the result of the interaction between the Pacific and Indo-Atlantic segments of the Earth. Geotektonika 4: 29–47 (in Russian)

RUZHENTSEV SV, POSPELOV II (1992) The South-Mongolian Variscan fold system. Geotektonika 5: 45–62 (in Russian)

RUZHENTSEV SV, BADARCH G, VOZNESENSKAYA TA (1985) Tectonics of Trans-Altay Zone of Mongolia. Geotektonika 4: 28–40 (in Russian)

SAFONOVA I, SELTMANN R, KRÖNER A, GLADKOCHUB D, SCHULMANN K, XIAO WJ, KIM JY, KOMIYA T, SUN M (2011) A new concept of continental construction in the Central Asian Orogenic Belt (compared to actualistic examples from the Western Pacific). Episodes 34: 186–196

SELTMANN R, KONOPELKO D, BISKE G, DIVAEV F, SERGEEV S (2011) Hercynian post-collisional magmatism in the context of Paleozoic magmatic evolution of the Tien Shan orogenic belt. J Asian Earth Sci 42: 821–838

SAUNDERS AD, NORRY MJ, TARNEY J (1991) Fluid influence on the trace element compositions of subduction zone magmas. In: TARNEY J, PICKERING KT, KNIPE RJ, DEWEY JF (eds) The Behaviour and Influence of Fluids in Subduction Zones. The Royal Society, London, pp 151–166

SAVATENKOV VM, KOZLOVSKY AM, YARMOLYUK VV, SMIRNOVA ZB (2016) Pb isotope composition of granitoids from the Hercynides of the Central Asian Orogenic Belt: evidence for growth of the juvenile crust. Dokl Earth Sci 470: 985–989

SAVATENKOV VM, KOZLOVSKY AM, YARMOLYUK VV, RUDNEV SN, OYUNCHIMEG T (2020) Pb and Nd isotopic data on granitoids from the Lake Zone, Mongolian and Gobi Altai with implications for the crustal growth of the Central Asian Orogenic Belt. Petrology 28: 403–417

SHAND SJ (1943) Eruptive Rocks. Their Genesis, Composition, Classification, and Their Relation to Ore-Deposits with a Chapter on Meteorite, 2nd edition. John Wiley & Sons, New York, pp 1–444

SHEN XM, ZHANG HX, WANG Q, WYMAN DA, YANG YH (2011) Late Devonian–Early Permian A-type granites in the southern Altay Range, northwest China: petrogenesis and implications for tectonic setting of "A_2-type" granites. J Asian Earth Sci 42: 986–1007

SKJERLIE KP, JOHNSTON AD (1992) Vapor-absent melting at 10 kbar of a biotite- and amphibole-bearing tonalitic gneiss: implications for the generation of A-type granites. Geology 20: 263–266

SKUZOVATOV S (2021) Nature and (in-)coherent metamorphic evolution of subducted continental crust in the Neoproterozoic accretionary collage of SW Mongolia. Geosci Front 12: 101097

SLÁMA J, KOŠLER J, CONDON DJ, CROWLEY JL, GERDES A, HANCHAR JM, HORSTWOOD MSA, MORRIS GA, NASDALA L, NORBERG N, SCHALTEGGER U, SCHOENE B, TUBRETT MN, WHITEHOUSE MJ (2008) Plešovice zircon – a new natural reference material for U–Pb and Hf isotopic microanalysis. Chem Geol 249: 1–35

SOEJONO I, BURIÁNEK D, SVOJTKA M, ŽÁČEK V, ČÁP P, JANOUŠEK V (2016) Mid-Ordovician and Late Devonian magmatism in the Togtokhinshil Complex: new insight into the formation and accretionary evolution of the Lake Zone (western Mongolia). J Geosci 61: 5–23

SOEJONO I, BURIÁNEK D, JANOUŠEK V, SVOJTKA M, ČÁP P, ERBAN V, GANPUREV N (2017) A reworked Lake Zone margin: chronological and geochemical constraints from the Ordovician arc-related basement of the Hovd Zone (western Mongolia). Lithos 294–295: 112–132

SOEJONO I, PEŘESTÝ V, SCHULMANN K, ČOPJAKOVÁ R, SVOJTKA M, ŠTÍPSKÁ P, BURIÁNEK D, JANOUŠEK V, LEXA O (2021) Structural, metamorphic and geochronological constraints on Palaeozoic multi-stage geodynamic evolu-

tion of the Altai accretionary wedge system (Hovd Zone, western Mongolia). Lithos 396–397: 106204

Song P, Wang T, Tong Y, Zhang JJ, Huang H, Qin Q (2019) Contrasting deep crustal compositions between the Altai and East Junggar orogens, SW Central Asian Orogenic Belt: evidence from zircon Hf isotopic mapping. Lithos 328–329: 297–311

Steiger RH, Jäger E (1977) Subcommission on Geochronology; convention on the use of decay constants in geo- and cosmochronology. Earth Planet Sci Lett 36: 359–362

Suess E (1901) Das Antlitz der Erde, vol. III. F. Tempsky, Prague–Vienna, pp 1–508

Sun SS, McDonough WF (1989) Chemical and isotopic systematics of oceanic basalts: implications for mantle composition and processes. In: Saunders AD, Norry M (eds) Magmatism in the Ocean Basins. Geological Society of London Special Publications 42, pp 313–345

Sylvester PJ (1989) Post-collisional alkaline granites. J Geol 97: 261–280

Sylvester PJ (1998) Post-collisional strongly peraluminous granites. Lithos 45: 29–44

Şengör AMC, Natal'in BA (1996) Turkic-type orogeny and its role in the making of the continental crust. Ann Rev Earth Planet Sci 24: 263–337

Şengör AMC, Natal'in BA, Burtman VS (1993) Evolution of the Altaid tectonic collage and Paleozoic crustal growth in Eurasia. Nature 364: 299–307

Šourek J, Černý M, Rejchrt M (eds) (2003) Geological and geochemical mapping of Trans-Altay Gobi at a scale 1 : 200,000. Unpublished Report MRPAM, Ulaanbaatar, pp 1–64

Tanaka T, Togashi S, Kamioka H, Amakawa H, Kagami H, Hamamoto T, Yuhara M, Orihashi Y, Yoneda S, Shimizu H, Kunimaru T, Takahashi K, Yanagi T, Nakano T, Fujimaki H, Shinjo R, Asahara Y, Tanimizu M, Dragusanu C (2000) JNdi-1: a neodymium isotopic reference in consistency with LaJolla neodymium. Chem Geol 168: 279–281

Tatsumi Y, Eggins S (1995) Subduction Zone Magmatism. Frontiers in Earth Sciences, Blackwell, Cambridge, Mass., pp 1–211

Taylor JP, Webb LE, Johnson CL, Heumann MJ (2013) The lost South Gobi microcontinent: protolith studies of metamorphic tectonites and implications for the evolution of continental crust in southeastern Mongolia. Geosci 3: 543–584

Taylor SR, McLennan SM (1995) The geochemical evolution of the continental crust. Rev Geophys 33: 241–265

Tetsopgang S, Enami M, Njonfang E (2011) Emplacement P–T conditions of Pan-African biotite–amphibole granitoids in the Nkambe area, Cameroon. J Mineral Petrol Sci 106: 306–319

Tong Y, Wang T, Kovach VP, Hong DW, Han BF (2006) Age and origin of the Takeshiken postorogenic alkali-rich intrusive rocks in southern Altai, near the Mongolian border in China and its implications for continental growth. Acta Petrol Sin 22: 1267–1278

Tong Y, Wang T, Siebel W, Hong DW, Sun M (2012) Recognition of early Carboniferous alkaline granite in the southern Altai Orogen: post-orogenic processes constrained by U–Pb zircon ages, Nd isotopes, and geochemical data. Int J Earth Sci 101: 937–950

Tong Y, Wang T, Jahn BM, Sun M, Hong DW, Gao JF (2014) Post-accretionary Permian granitoids in the Chinese Altai Orogen: geochronology, petrogenesis and tectonic implications. Am J Sci 314: 80–109

Van Der Voo R, Van Hinsbergen DJJ, Domeier M, Spakman W, Torsvik TH (2015) Latest Jurassic–earliest Cretaceous closure of the Mongol-Okhotsk Ocean: a paleomagnetic and seismological–tomographic analysis. In: Anderson TH, Didenko AN, Johnson CL, Khanchuk AI, MacDonald Jr JH (eds) Late Jurassic Margin of Laurasia – A Record of Faulting Accommodating Plate Rotation. Geological Society of America Special Papers 513, pp 589–606

Vermeesch P (2018) IsoplotR: A free and open toolbox for geochronology. Geosci Front 9: 1479–1493

Wainwright AJ, Tosdal RM, Wooden JL, Mazdab FK, Friedman RM (2011) U–Pb (zircon) and geochemical constraints on the age, origin, and evolution of Paleozoic arc magmas in the Oyu Tolgoi porphyry Cu–Au district, southern Mongolia. Gondwana Res 19: 764–787

Wang T, Hong DW, Jahn BM, Tong Y, Wang YB, Han BF, Wang XX (2006) Timing, petrogenesis, and setting of Paleozoic synorogenic intrusions from the Altai Mountains, northwest China: implications for the tectonic evolution of an accretionary orogen. J Geol 114: 735–751

Wang T, Tong Y, Zhang L, Li S, Huang H, Zhang J, Guo L, Yang Q, Hong D, Donskaya T, Gladkochub D, Tserendash N (2017) Phanerozoic granitoids in the central and eastern parts of Central Asia and their tectonic significance. J Asian Earth Sci 145: 368–392

Wang S, Jiang YD, Weinberg R, Schulmann K, Zhang J, Li PF, Xiao M, Xia XP (2021) Flow of Devonian anatectic crust in the accretionary Altai Orogenic Belt, central Asia: insights into horizontal and vertical magma transfer. Geol Soc Am Bull 133: 2501–2523

Wasserburg GJ, Jacobsen SB, DePaolo DJ, McCulloch MT, Wen T (1981) Precise determination of Sm/Nd ratios, Sm and Nd isotopic abundances in standard solutions. Geochim Cosmochim Acta 45: 2311–2324

Watson EB, Harrison TM (1983) Zircon saturation revisited: temperature and composition effects in a variety of crustal magma types. Earth Planet Sci Lett 64: 295–304

Whalen JB, Currie KL, Chappell BW (1987) A-type granites: geochemical characteristics, discrimination and petrogenesis. Contrib Mineral Petrol 95: 407–419

WHITNEY DL, EVANS BW (2010) Abbreviations for names of rock-forming minerals. Amer Miner 95: 185–187

WIEDENBECK M, ALLÉ P, CORFU F, GRIFFIN WL, MEIER M, OBERLI F, VON QUADT A, RODDICK JC, SPIEGEL W (1995) Three natural zircon standards for U–Th–Pb, Lu–Hf, trace element and REE analyses. Geostand Newsl 19: 1–23

WINDLEY BF, ALEXEIEV D, XIAO W, KRÖNER A, BADARCH G (2007) Tectonic models for accretion of the Central Asian Orogenic Belt. J Geol Soc, London 164: 31–47

WOOD DA (1980) The application of a Th–Hf–Ta diagram to problems of tectonomagmatic classification and to establishing the nature of crustal contamination of basaltic lavas of the British Tertiary volcanic province. Earth Planet Sci Lett 50: 11–30

XIAO WJ, WINDLEY BF, BADARCH G, SUN S, LI J, QIN K, WANG Z (2004) Palaeozoic accretionary and convergent tectonics of the southern Altaids: implications for the growth of central Asia. J Geol Soc, London 161: 339–342

XIAO WJ, WINDLEY BF, HUANG BC, HAN CM, YUAN C, CHEN HL, SUN M, SUN S, LI JL (2009) End-Permian to mid-Triassic termination of the accretionary processes of the southern Altaids: implications for the geodynamic evolution, Phanerozoic continental growth, and metallogeny of Central Asia. Int J Earth Sci 98: 1189–1217

XIAO WJ, WINDLEY BF, SUN S, LI J, HUANG B, HAN C, YUAN C, SUN M, CHEN H (2015) A tale of amalgamation of three Permo–Triassic collage systems in central Asia: oroclines, sutures, and terminal accretion. Ann Rev Earth Planet Sci 43: 477–507

XIAO WJ, WINDLEY BF, HAN C, LIU W, WAN B, ZHANG J, AO S, ZHANG Z, SONG D (2018) Late Paleozoic to early Triassic multiple roll-back and oroclinal bending of the Mongolia collage in Central Asia. Earth Sci Rev 186: 94–128

XU XW, JIANG N, LI XH, QU X, YANG YH, MAO Q, WU Q, ZHANG Y, DONG LH (2013) Tectonic evolution of the East Junggar terrane: evidence from the Taheir tectonic window, Xinjiang, China. Gondwana Res 24: 578–600

XU XW, JIANG N, LI XH, WU C, QU X, ZHOU G, DONG LH (2015) Spatial–temporal framework for the closure of the Junggar Ocean in central Asia: new SIMS zircon U–Pb ages of the ophiolitic mélange and collisional igneous rocks in the Zhifang area, East Junggar. J Asian Earth Sci 111: 470–491

XU X, ZUZA AV, YIN A, LIN XB, CHEN HL, YANG SF (2020) Permian plume-strengthened Tarim lithosphere controls the Cenozoic deformation pattern of the Himalayan–Tibetan Orogen. Geology 49: 96–100

YANG SH, MIAO L, ZHANG F, ZHU MS, ZHOU Y, BAATAR M, ANAAD C (2019) Detrital zircon age spectra of the Gurvan Sayhan accretionary complex in South Mongolia: constraints on the Late Paleozoic evolution of the southern Central Asian Orogenic Belt. J Asian Earth Sci 175: 213–229

YANG SH, MIAO LC, LIU CH, ZHANG F, SMIT MA, ZHU MS, BAATAR M (2022) Late Carboniferous–middle Permian granitoids in south Mongolia: implications for post-subduction processes in southern Central Asian Orogenic Belt. Int Geol Rev 64: 722–741

YARMOLYUK VV, KOVALENKO VI, SAL'NIKOVA EB, KOVACH VP, KOZLOVSKY AM, KOTOV AB, LEBEDEV VI (2008) Geochronology of igneous rocks and formation of the Late Paleozoic south Mongolian active margin of the Siberian Continent. Stratigr Geol Correl 16: 162–181

YARMOLYUK VV, KUZMIN MI, KOZLOVSKY AM (2013) Late Paleozoic–Early Mesozoic within-plate magmatism in North Asia: traps, rifts, giant batholiths, and the geodynamics of their origin. Petrology 21: 101–126

YARMOLYUK VV, KUZMIN MI, ERNST RE (2014) Intraplate geodynamics and magmatism in the evolution of the Central Asian Orogenic Belt. J Asian Earth Sci 93: 158–179

ZHANG SH, ZHAO Y, SONG B, YANG ZY, HU JM, WU H (2007) Carboniferous granitic plutons from the northern margin of the North China block: implications for a late Paleozoic active continental margin. J Geol Soc, London 164: 451–463

ZHANG CL, LI ZX, LI XH, XU YG, ZHOU G, YE HM (2010) A Permian large igneous province in Tarim and Central Asian Orogenic Belt, NW China: results of a ca. 275 Ma mantle plume? Geol Soc Am Bull 122: 2020–2040

ZHANG CL, SANTOSH M, ZOU HB, XU YG, ZHOU G, DONG YG, DING RF, WANG HY (2012) Revisiting the "Irtish tectonic belt": implications for the Paleozoic tectonic evolution of the Altai Orogen. J Asian Earth Sci 52: 117–133

ZHANG J, WANG T, TONG Y, ZHANG Z, SONG P, ZHANG L, HUANG H, GUO L, HOU Z (2017) Tracking deep ancient crustal components by xenocrystic/inherited zircons of Palaeozoic felsic igneous rocks from the Altai–East Junggar terrane and adjacent regions, western Central Asian Orogenic Belt and its tectonic significance. Int Geol Rev 59: 2021–2040

ZHANG C, LUO Q, ZHANG X, LIU L, LIU D, WANG P, YANG K, WANG J, ZHAO Y (2018a) Geochronological, geochemical, and Sr–Nd–Hf isotopic studies of the Aketas adakitic granites in Eastern Junggar: petrogenesis and tectonic implications. Geol J 53: 80–101

ZHANG H, WANG D, WANG R, LIU J, LI R (2018b) Metasomatic alteration of volcanic–sedimentary terrane in the Early Devonian: implication for the formation of the Mengxi porphyry copper deposit, eastern Junggar, Central Asian Orogenic Belt. Geol J 53: 278–292

ZHANG X, TONG Y, WANG T, ZHAO H, GUO L, TSERENDASH N, PUNTSAG D (2021) Petrogenesis and tectonic significance of Carboniferous granites on the north side of the Solonker Suture, Central South Mongolia. Acta Geol Sin 95: 481–499

Zhou G, Wu G, Dong L, Zhang Z, Dong Y, Tong Y, He L, Ying L (2009) Formation time and geochemical feature of Wutubulak Pluton in the northeastern margin of Junggar in Xinjiang and its geological significance. Acta Petrol Sin 17: 1390–1402 (in Chinese with English abstract)

Zhou H, Zhao G, Han Y, Zhang D, Zhao Q, Orsoo EO, Pei X (2021) Magmatic evidence for Late Carboniferous–Early Permian slab breakoff and extension of the southern Mongolia collage system in Central Asia. Gondwana Res 89: 105–118

Zhu M, Baatar M, Miao L, Anaad C, Zhang F, Yang S, Li Y (2014) Zircon ages and geochemical compositions of the Manlay ophiolite and coeval island arc: implications for the tectonic evolution of South Mongolia. J Asian Earth Sci 96: 108–122

Zhu M, Miao L, Baatar M, Zhang F, Anaad C, Yang S, Li X (2016) Late Paleozoic magmatic record of Middle Gobi area, south Mongolia and its implications for tectonic evolution: evidences from zircon U–Pb dating and geochemistry. J Asian Earth Sci 115: 507–519

Zonenshain LP, Suyetenko OD, Jamyandamba L, Eengin G (1975) Structure of the axial part of the South Mongolian eugeosyncline in the Dzolen Range. Geotectonics 9: 214–220

Zorin YA (1999) Geodynamics of the western part of the Mongolia–Okhotsk collisional belt, Trans-Baikal region (Russia) and Mongolia. Tectonophysics 306: 33–56